ABSTRACT

Title of Document: STRAIN ENERGY DENSITY AND
                      THERMODYNAMIC ENTROPY AS
                      PROGNOSTIC MEASURES OF CRACK
                      INITIATION IN ALUMINUM

                      Victor Luis Ontiveros, Ph.D., 2013

Directed By: Professor Mohammad Modarres,
                      Department of Mechanical Engineering

A critical challenge to the continued use of engineering structures as they are asked to

perform longer than their design life is the prediction of an initiating crack and the prevention

of damage, estimation of remaining useful life, schedule maintenance and to reduce costly

downtimes and inspections. The research presented in this dissertation explores the

cumulative plastic strain energy density and thermodynamic entropy generation up to crack

initiation. Plastic strain energy density and thermodynamic entropy generation are evaluated

to investigate whether they would be capable of providing a physical basis for fatigue life and

structural risk and reliability assessments. Navy aircraft, specifically, the Orion P-3C, which

represent an engineered structure currently being asked to perform past is design life, which

are difficult and time consuming to inspect from carrier based operations and are currently

evaluated using an empirically based damage index the, fatigue life expended, is used as an

example in this investigation.

A set of experimental results for aluminum alloy 7075-T651, used in airframe structures, are

presented to determine the correlation between plastic strain energy dissipation and the

thermodynamic entropy generation versus fatigue crack initiation over a wide range of fatigue loadings. Cumulative plastic strain energy and thermodynamic entropy generation measured from hysteresis energy and temperature rise proved to be valid physical indices for estimation of the probability of crack initiation. Crack initiation is considered as a major evidence of fatigue damage and structural integrity risk. A Bayesian estimation and validation approach is used to determine systematic errors in the developed models as well as other model uncertainties. Comparisons of the energy-based and entropy-based models are presented and benefits of using one over the other are discussed.

STRAIN ENERGY DENSITY AND THERMODYNAMIC ENTROPY AS
PROGNOSTIC MEASURES OF CRACK INITIATION IN ALUMINUM

By

Victor Luis Ontiveros

Dissertation submitted to the Faculty of the Graduate School of the
University of Maryland, College Park, in partial fulfillment
of the requirements for the degree of
Doctor of Philosophy
2013

Advisory Committee:
Professor Mohammad Modarres, Chair
Professor Ali Mosleh
Professor Hugh Bruck
Dr. David Barrett
Professor Sung Lee (Dean's Representative)

Acknowledgements

I must thank everyone who contributed to the completion of this work, there are truly too many single everyone out.

I would like to thank my advisor, Dr. Mohammad Modarres, for his guidance, patience and support throughout my graduate studies at Maryland. I would also like to thank the members of my dissertation committee for their support during my research. I must thank Dr. David Barrett and Mr. David Rusk from NAVIAR for constant support and willingness to set time aside to answer my many questions.

My thanks to Dr. Mohammad Reza Azarkhail for spending countless hours reviewing concepts of reliability engineering with me, and then, going over them once more. Huzzah! I would like to thank Dr. Mehdi Amiri for his considerable patience in teaching me the ways of entropy.

I must thank my colleagues in the Center for Risk and Reliability for their constant support and the countless hours of help coding MATLAB and discussing the challenges of research. Specifically, my thanks to Mohammad Nuhi Faradini, Gary Paradee and and Dr. Shunpeng Zhu for our many tea times. Boss. Here's what I owe you:
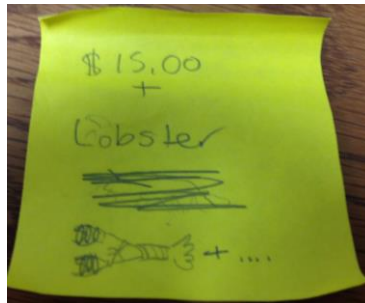
Thanks, my Frisbee friends. For moments of peace each week. So many fun games.

I must thank my friends for reminding me how long I've been in school. HR roll out.

And, thank you Mom, Dad, Brother, and Buffalo Kitty for constant love and support.

Table of Contents

.

List of Tables

List of Figures

Chapter 1: Introduction

1.1 Motivation and background

Many engineered systems are now expected to function longer than their initial design life. One example would be nuclear power plants, which are currently being used longer than their original 40-year license (NRC, 2013). Another example is aircraft. The United States Navy (USN) follows a Structural Appraisal of Fatigue Effects (SAFE) life approach. In this regime, aircraft are assumed to be 'crack free' when new and they are retired when they reach the point at which a crack initiates, usually assumed to be a length of 0.01 inches, before the onset of fatigue crack growth (Hoffman, 2005, Iyyer, 2007). For aircraft that are carrier-based the SAFE life approach offers a feasible life management program (Hoffman, 2005) when the operating environment and the viability of conducting inspections aboard ships presents a challenge. During flight, data is taken on the aircraft by multi-channel data recorders (See Figure 1.1). This data is used to compute the load and stress on the aircraft. Next, the stress-strain response is modeled and these results are compared with the results from full scale fatigue tests to estimate the current damage. This fatigue damage calculation methodology is shown in Figure 1. With these results, a relative fatigue life expended (FLE) can be determined. Recent service findings show that a majority of the fleet aircraft are beyond the SAFE-life bench marks (Iyyer, et. al., 2006).
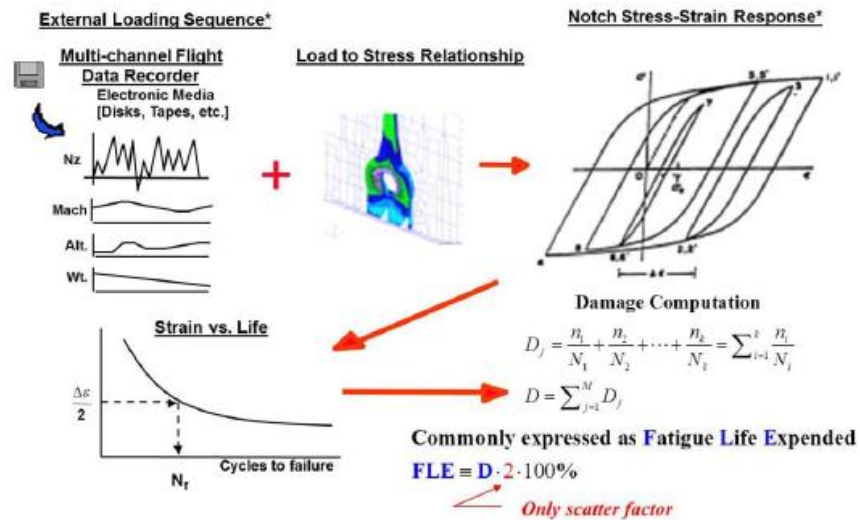
Figure 1.1: Fatigue damage calculation methodology (Hoffman, 2005)

In earlier work performed at the University of Maryland, the plastic strain energy density at the point of 100% FLE for some forty (40) P-3 aircraft was calculated using data recorded during the life of the aircraft (Hoffman, 2010). The results showed that the plastic strain energy density at the end of each aircraft's design life fell within a tight band (Figure 1.2).
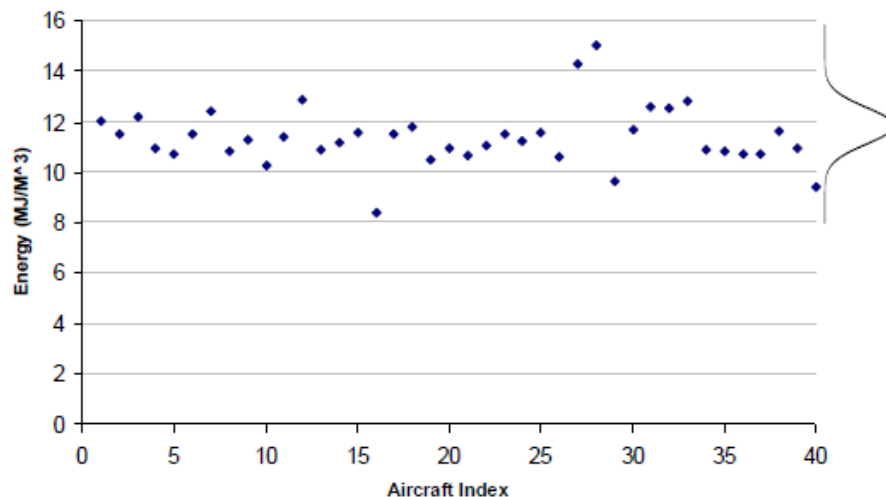
Figure 1.2: Plastic Strain energy density for 40 P-3 Aircraft (Hoffman, 2010)

This led to the proposal of the current study on strain energy density. During this study, results were published showing a limit of thermodynamic entropy generation at the point of fracture for Al 6061 (Naderi et al., 2010.) This study was expanded to include thermodynamic entropy, to see if the same limit could be found for crack initiation. As a means to move away from the standard established method of using tests to demonstrate the life of an aircraft, this current work examines the possibility of using strain energy density and thermodynamic entropy as measures of component degradation (Doelling et. al, 2000; Basaran and Tang, 2002)

The motivation behind this research is to determine if a limit on strain energy density can be used as a reliable limit for the remaining life of an aircraft. Additionally, other entities, such as the total strain energy density, which combines the elastic and plastic strain energy density and the thermodynamic entropy which makes use of the plastic strain energy density will be explored. Data will be generated through accelerated fatigue tests of Al 7075-T651, an alloy used in airframe construction. The result will be the development of a prognostic, physics-based model capable of estimating the life expended of the alloy.

1.2 Research Objective

The main objectives of this dissertation are listed as:

- Review developments in the use of strain energy density and thermodynamic entropy as means of fatigue life assessment.
- To experimentally search for limits on plastic strain energy density, total strain energy density, and thermodynamic entropy at the point of crack initiation.
- To develop models for the determination of cycles to crack initiation using plastic strain energy density dissipation and thermodynamic entropy generation.

- To assess the uncertainty of the models developed using a Bayesian inference approach

- To determine the true cycles to crack initiation given a model prediction from the models developed using a Bayesian updating approach.

- To determine the probability of crack initiation at a given number of cycles using models developed for plastic strain energy density and thermodynamic entropy.

1.3 Methodology

Given the challenge posed on inspecting fleets of aircraft, new methods must be explored. Recent areas of research at the University of Maryland have explored means of developing physics-based, probabilistic methods for risk assessment and management of ageing aircraft. The objective of this research is to present one such means by proposing the development of models for determining a point of crack initiation using strain energy density and thermodynamic entropy.

This theory will be tested by comparing the plastic strain energy density, total strain energy density and thermodynamic entropy generation values at the point of crack initiation for a number of accelerated fatigue tests performed on Al 7075-T651, a material commonly used in airframe construction. These experiments will involve a range of loading conditions to test the validity of this theory. During these experiments stress and strain data will be collected and used to generate the hysteresis loops for the determination of the plastic, elastic, and total strain energy density densities. Temperature data will also be collected and combined with the plastic strain energy density for the determination of the thermodynamic entropy generation. The models for plastic strain energy density dissipation and thermodynamic entropy generation will be made using these experimentally generated values.

The first model developed will use the plastic strain energy density dissipation to probabilistically predict the cycles to crack initiation. The difference in experimental results

to those found in the P-3 aircraft will be discussed. The model developed will be capable of predicting the cycles to crack initiation for a range of loading conditions. The model will be validated using independent experimental results at similar and alternate loading conditions. Uncertainty and bias in the model will be estimated using a Bayesian analysis inference. The results provide a physics-based approach for predicting crack initiation of Al 7075-T651 subject to fatigue loading.

A similar analysis will be repeated to develop a model to probabilistically determine the cycles to crack initiation using thermodynamic entropy generation. The difference in results to those found in the literature (Naderi et al., 2010) will be discussed. The model developed will be capable to predicting the distribution of cycles-to-crack initiation for a range of loading conditions.

The results developed through this method have significant potential to be used as a non-destructive means of providing an evidence driven prognostic and structural health modeling for life assessment.

1.4 Contributions of this work

The primary contributions of this dissertation will include development of a non-destructive assessment of crack initiation using physical measures as opposed to the empirically driven Palmgren-Miner rule. The probability of crack initiation will be estimated using the physical measures, plastic strain energy density dissipation and thermodynamic entropy generation. Additionally, confirmation of the historically observed increase in plastic strain energy density with fatigue life is made and it's relation with the thermodynamic entropy generation is discussed.

1.5 Outline of the Dissertation

The remainder of this dissertation is organized into four chapters.

Chapter 2 presents a literature review of the history and background strain energy density and thermodynamic entropy. In Chapter 3, the experimental approach for gathering the cumulative strain energy density dissipation and thermodynamic entropy generation is reviewed. Chapter 4 reviews the probabilistic model development and approach for using both strain energy density and thermodynamic entropy to predict crack initiation. The uncertainty analysis and model validation are discussed in this chapter as well. Finally, the conclusions of this dissertation as well as its contributions are listed in Chapters 5. Suggestions for future research are also provided in Chapter 5.

Chapter 2: Understanding Fatigue through Strain energy density and Thermodynamic Entropy

2.1 Overview

This chapter will consist of a review of the history and theory of strain energy density and thermodynamic entropy. Additionally, a discussion of the application of these and other tools to the understanding of fatigue life will be made.

The historical review in this chapter set the foundation for the rest of this dissertation to be built upon. The results obtained here will be used to develop the life models using strain energy density and thermodynamic entropy. Once developed, the models will be used to estimate probability of reaching the point of crack initiation using strain energy density and thermodynamic entropy.

2.2.1 Brief History of Strain energy density

A considerable amount of research has been put into understanding strain energy density's role in fatigue. As early as 1911 Bairstow described the role of hysteresis energy in the fatigue process through observations of the hysteresis loops stating that if the stress is sufficiently great, the specimen becomes inelastic resulting in work being performed and expended in moving portions of the crystals relative to one another (Bairstow, 1911). These movements are likely associated with microscopic slip-lines that develop into cracks and ultimately rupture (Bairstow, 1911). In 1923 Jasper studied the relation between energy and fatigue failure as a means of estimating fatigue damage. In 1947 Hanstock attempted to relate fatigue life to the total measured total hysteresis energy required for fatigue (Hanstock, 1947). Hanstock (1947) proposed a linear relation (Eq. 2.1) for the prediction of energy as a function

of the number of cycles to failure, N_f, using two empirically developed material constants, C and D:

$$\sum_0^{N_f} \Delta E = C + DN_f \qquad (2.1)$$

However, Hanstock (1947) noted that the failure was easier predicted using the amount of strain hardening since a considerable portion of the energy may appear as thermal energy, which is not captured in the hysteresis loop.

The concept of a critical dissipated energy required to cause fatigue fracture was first hypothesized by Enomoto in 1955 (Enomoto, 1955). In 1961 Feltner and Morrow explored the plastic strain energy density as a possible index that could be used to express the accumulated fatigue damage (Felter and Morrow, 1961). This postulated constant plastic strain energy density required for fracture was called the 'fatigue toughness' (Chang, 1968).

However, it was quickly determined experimentally that the hysteresis energy required for fatigue fracture was not a constant, but increased with the fatigue life (Martin and Brinn, 1959; Martin, 1961; Topper and Biggs, 1966; Halford, 1966). Halford compiled a large compilation of the cumulative plastic strain energy density at the point of failure showing the relation of increasing energy as the cycles to failure increased (See Figure 2.1)

In the 1960's the relating strain energy density to fatigue fracture focused on the plastic strain energy density as it was determined that the anelastic strain energy density should not be considered as contributing to fatigue damage since it is not associated with plastic strain (Feltner, 1959; Feltner and Morrow, 1961; Morrow, 1965). In 1961 Martin, presented a theory that, only energy associated with strain hardening causes damage, this damage per cycle is constant and the critical energy for failure is equal to that obtained in a static tension test (Martin, 1961). In 1966 Stowell showed that the cyclic strain energy density accumulated at failure was equal to the energy accumulated during a monotonic test (Stowell, 1966).

Plastic strain energy per cycle as a function of strain reversals.
Comparison of the Cyclic Stress and Plastic Strain Energy for Waspalloy (4).
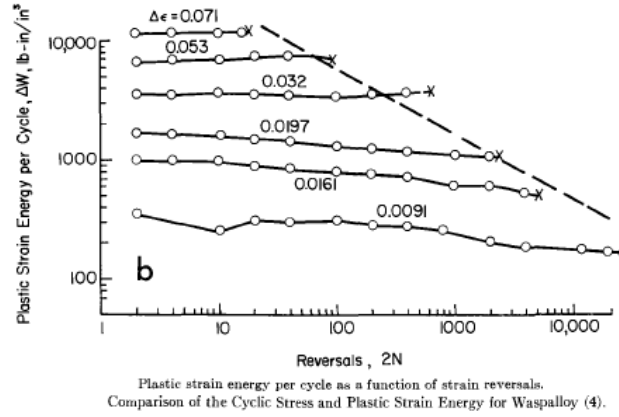
Figure 2.1: Plastic strain energy density per cycle as a function of strain reversals [Morrow, 1965]

In 1965 Morrow used the observation that that the plastic strain energy density per cycle was relativity constant throughout the fatigue life (see Figure 2.1) for constant loading conditions and developed relations for estimating the fatigue damage using the cumulative plastic strain energy density per cycle using cyclic stress-strain properties under a fully reversed fatigue loads (Morrow 1965, Halford 1966, Park and Nelson, 2000):

$$\Delta W_p = 4\sigma_f' \varepsilon_f' \left(\frac{c-b}{c+b}\right)\left(2N_f\right)^{b+c} \tag{2.2}$$

and

$$\Delta W_p = \frac{4\varepsilon_f'\left(\frac{1-n'}{1+n'}\right)\sigma_a^{(1+n')/n'}}{\sigma_f'^{1/n'}} \tag{2.3}$$

where fatigue strength coefficient: σ_f', fatigue strength coefficient: b, fatigue ductility coefficient: ε_f', fatigue ductility exponent: c, cyclic strain hardening exponent: n', final number of cycles: N_f, stress amplitude: σ_a Shown in Figure 2.2 is the plastic strain energy density per cycle as a function of strain reversals (Morrow, 1965). As shown, the energy remains fairly constant throughout the life of the metal.

Equations 2.2 and 2.3 make use of cyclic fatigue material properties. Often, these properties can be taken from literature. However, care should be taken as different values for

9

the same material can be found in the literature and their use can lead to results that differ on

an order of magnitude. This difference in results will be discussed in relation to results

determined in this study later in Chapter 4. Additionally, distinction is important as the use of

equations, for the determination of the plastic strain energy density introduces additional

uncertainties into the analysis as any model is at best an approximation of reality, no matter

how complex it may be (Droguett, 1999). As a result a model will always introduce

additional uncertainty into the analysis based on the assumptions used in the creation of the

model. Examples of some values are shown below in Table 2.1. For a comparison of the

differences that can result from the use of different literature values will be explored using the

results obtained from experiments used in this study.
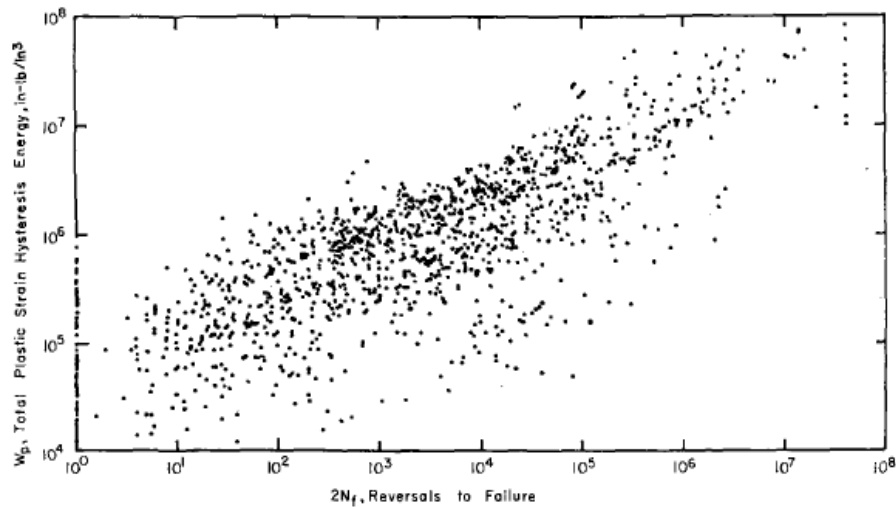
Figure 2.2: Total plastic strain energy density required for fatigue fracture
(Halford, 1964, Morrow, 1965).

Table 2.1: Cyclic and fatigue properties of Al 7075-T651 (Ince and Glinka, 2011; Zhao and
Jiang, 2008; Brammer, 2013)

Fatigue strength coefficient, σ_f'	1576 MPa	952 MPa
Fatigue strength exponent, b	-0.1609	-0.089
Fatigue ductility coefficient ε_f'	0.1575	0.182
Fatigue ductility exponent, c	-0.6842	-0.43
Cyclic strain hardening exponent, n'	0.0597	0.0662

The traditional concept of a hysteresis loop often described in engineering is shown below in Figure 2.3 (Boroński and Mroziński, 2007). The plastic strain energy density is represented by the area bounded inside the hysteresis loop. The elastic strain energy density is represented by the area outside the hysteresis loop, as showing in Figure 2.3.

In Figure 2.3, the plastic strain energy density makes up a considerable portion of the total energy. This is not representative of the response seen in aircraft. The loads on the aircraft lead to a response that yields very small amount of plastic deformation. To be more representative of the loads seen by an aircraft, for experiments used in this research, the plastic deformation was kept low – resulting in low plastic strain energy density. In Figure 2.4, a more appropriate representative hysteresis loop is shown. Here, the area plastic strain energy density, bounded inside the loop is very small compared to the elastic strain energy density, represented by the area under the loop.

With such a low amount of plastic strain energy density expected, the total strain energy density could be used as a better means to determine the life of an aircraft.
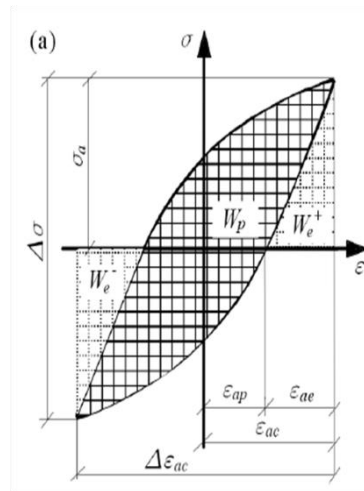
Figure 2.3: Hysteresis loop (Mroziński and Boroński, 2007)

Early study on strain energy density focused on the plastic strain energy density. However, for instances in which the plastic strain energy density component, $\Delta\varepsilon_p$, of the strain energy density, $\Delta\varepsilon$, is small, and approaches zero, $\Delta\varepsilon_p \rightarrow 0$, the plastic strain energy

density per cycle also approaches zero, $\Delta W_p \to 0$, other researchers proposed returning to the use of both the plastic and elastic strain energy density. A number of researchers proposed using the total strain energy density, which includes the elastic strain energy density, as a means of predicting fatigue damage (Golos and Ellyin, 1988; Kujawski, 1989; Golos, 1995; Park and Nelson, 2000).

Grasping that, particularly for instances of high cycles fatigue (HCF) the total strain energy density could provide a means of predicting fatigue life, Golos and Ellyin (1988) proposed a method making use of both the plastic strain energy density and the strain energy density associated with the tensile load. An empirical relation for the total energy per cycle, W_t, as a function of the cycles to failure was proposed as:

$$\Delta W_t = \kappa N_f^{\alpha} + C \tag{2.4}$$

where κ, α and C are constants determined by least-squares fit to experimental data. Results from Eq. (2.4) appeared to fit well for ASTM A-516 Gr. 70 carbon steel.

Park and Nelson (Park and Nelson, 2000) also proposed a means of estimating the fatigue life using the total strain energy density, a combination of the plastic, W_p, and elastic strain energy density, W_e:

$$W_t = W_p + W_e = AN_f^{\alpha} + BN_f^{\beta} \tag{2.5}$$

where A, B, α, and β are constants determined empirically from uniaxial fatigue test data. Similar to Morrow's relations for the plastic strain energy density per cycle, the elastic strain energy density can be determined using uniaxial fatigue properties (Park and Nelson, 2000):

$$W_e = \frac{2^{2b+1}(1+v)\sigma_f'^2}{3E} N_f^{2b} \tag{2.6}$$

where b is the fatigue strength coefficient, E is the elastic modulus and v is Poisson's ratio.

Using previous evidence that the energy required to cause failure from fatigue was equal to the energy obtained in a tension test (Martin, 1961; Stowell, 1966), Scott-Emuakpor et. al. have proposed a means of predicting the cycles to failure using the total strain energy

density accumulated during a monotonic tension test divided by the strain energy density

accumulated in one hysteresis loop (Scott-Emuakpor, et. al, 2007; 2008.) The relation showed

reasonable life estimations when compared with experimental result and is seen below:

$$N_f = \frac{\sigma_n\left(\varepsilon_n - \frac{\sigma_n}{2E}\right) + \varepsilon_0\sigma_0\left[cosh\left(\frac{\sigma_n}{\sigma_0}\right) - 1\right] + \frac{\beta_A}{2}\left(\varepsilon_f^2 - \varepsilon_n^2\right) + \beta_0\left(\varepsilon_f - \varepsilon_n\right)}{2\sigma_c\left\{\frac{\sigma}{\sigma_c}sinh\left(\frac{2\sigma}{\sigma_c}\right) - \left[cosh\left(\frac{2\sigma}{\sigma_c}\right) - 1\right]\right\}}$$

(2.7)

Recalling that the observed constant plastic strain energy density dissipated

that was first noticed at the point of 100% FLE of the P-3 aircraft is the motivation of

this project (Figure 1.2), an understanding of the FLE must be reached.

2.2.2 Fatigue Life Expenditure

The fatigue life expenditure (FLE) is determined using a limited amount of

information taken during aircraft flight. A schematic, pictorially describing the FLE

calculation is shown below in Figure 2.5.

As shown in Figure 2.5, data including loads observed during the flight, mission

hours, weights and altitudes taken from the flight data recorder. All this data is then used to

estimate the FLE for an individual aircraft. FLE is an index that compares the amount of

damage accumulated by an aircraft to the damage experienced in a representative fatigue test.

This representative test involved a full-scale fatigue test (FSFT) of a P-3C Orion aircraft

(Lamas, 2003). The load spectrum was developed using fleet operation data over a period of

six years (Iyyer et. al., 2007). An 85th percentile spectrum was applied to ensure a severe

spectrum was applied. In the FSFT the time to reach a crack the size of 0.254 mm was

determined. This time demonstrated life was attributed to 200% FLE (Hurtado, 2006). A

scatter factor of 2 is used to account for fatigue property variability (Iyyer, 2007).
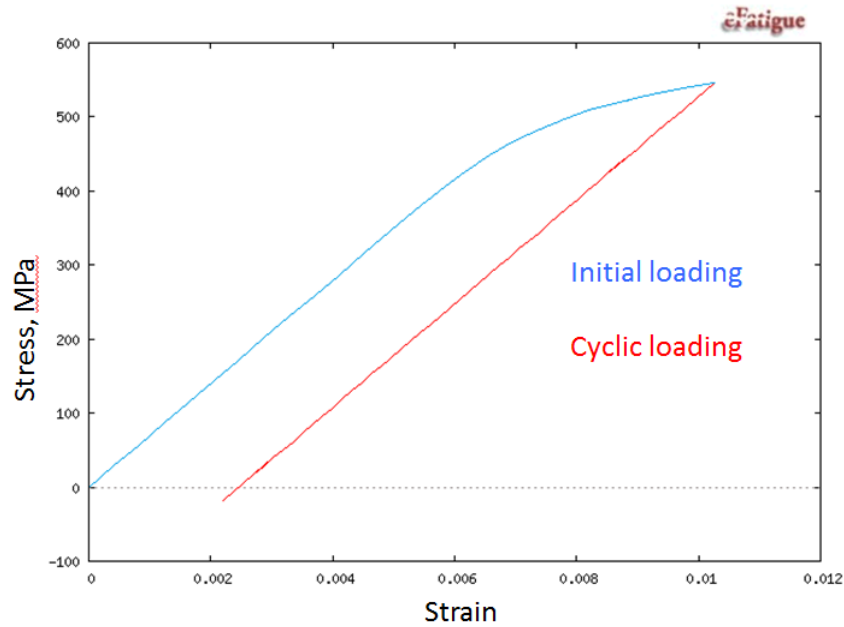
Figure 2.4: Hysteresis loop, low plastic deformation [Socie et. al., 2011]

In the work by Scott-Emuakpor et al, (Scott-Emuakpor et. al, 2011) the authors make note that their model (Equation 2.7) makes use of strain energy density only, and neglect energy dissipated through heat, vibration, surface defects and acoustics. This leads to a need to explore additional sources of dissipated energy that may not be captured in the hysteresis loop that could still contribute to fatigue damage.
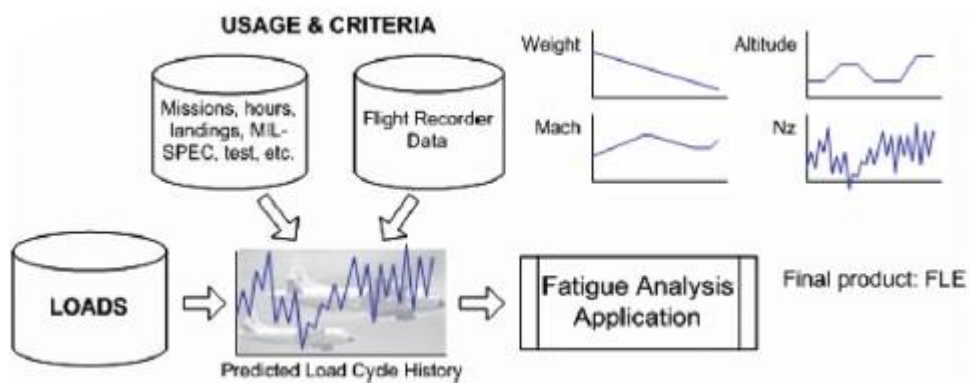
Figure 2.5. Schematic of tracking using multi-channel recorder data (Iyyer et. al., 2007).

2.2.3 Heat Energy

Early in the study of strain energy density, energy dissipated through heat was acknowledged as an important area (Hanstock, 1947; Morrow, 1965). In the same work that proposed the models for estimating the plastic strain energy density per cycle, Morrow noted that a major portion of the plastic strain energy density, ΔW_p, is dissipated into heat with the remaining mechanical energy causing dislocation movements and volumetric changes (Morrow, 1965). Similarly, during their study on using the total strain energy density as a means of predicting fatigue life, Golos and Ellyin (1988) noted that during fatigue a portion of the energy is converted to heat with the remaining rendered irrecoverable in the form of plastic strain energy density (Golos and Ellyin, 1988)

As a result, the temperature evolution (Yang, 2003; La Rosa and Risitano, 2000; Harig and Weber, 1983) that results from the hysteresis heating during the fatigue process has been another popular area of focus in the search of a determination of fatigue life.

Harig and Weber point out that during plastic deformation, the movement of dislocations increases atomic oscillations in both tension and compression. As a result, only a small portion of the internal energy is increased while a principle portion of the work is changed into heat (Harig and Weber, 1983). Hodowany found that around 90% of the plastic work was converted into heat (Hodowany, 1997). These findings suggest that the energy converted to heat is an important factor for consideration in the study of fatigue and strain energy density.

At the onset of fatigue the surface temperature begins to rise. This is a result of the energy density associated with the hysteresis effect, due to plastic deformation, gives rise to heat generation greater than heat loss from the specimen due to radiation and convection (Naderi et. al., 2011). The temperature rise can be seen in Figure 2.6. An observed oscillation in the temperature around the mean value is a result of the thermoelastic effect (Yang et. al.

2001, Meneghetti, 2007). As depicted in Figure 2.6, the initial temperature rise levels off and becomes uniform as the heat generation and heat loss to the surroundings reach equilibrium. Near the end of the experiment, as a result of a sufficiently large crack, the heat generation resulting from the plastic deformation of the specimen again out gains the heat loss resulting from convection and radiation and a large temperature rise is seen directly before rupture. Note, the spike seen midway through the experiment in the temperature is a result of the heat reflected by an observer approaching the test specimen to visually check for crack initiation.
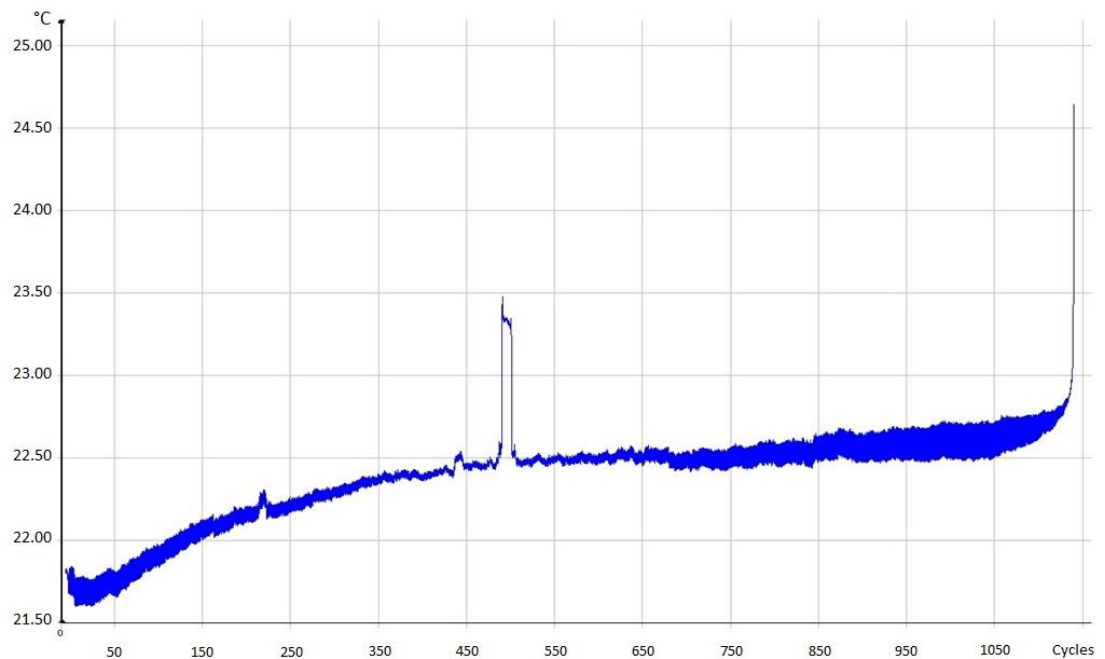
Figure 2.6: Example of a specimen temperature evolution

In 2007 Meneghetti studied this portion of mechanical energy that is converted to heat and dissipated to the surroundings (Meneghetti, 2007). Meneghetti was able to determine the heat energy dissipated per cycle by relating the change in temperature of the specimen when stopping the fatigue loading (Figure 2.7). Combining this information with material properties like density and specific heat, the heat power can be estimated by:

16

$$\rho \cdot c \cdot \frac{\partial T}{\partial t}\bigg|_{t=(t^*)^+} = -\left(H_{cd} + H_{cv} + H_{ir}\right)$$

(2.8)

where ρ is the density, c is the specific heat, and H is the power released as heat by the material per unit volume for conduction, convection and radiation.

Using the frequency, f, of the experiment, the energy released by heat per cycle, Q, can be estimated as:

$$Q = \frac{H}{f}$$

(2.8)

Meneghetti used the estimated heat energy per cycle to develop fatigue curves for smooth and notched specimens at different loading ratios for AISI 304 L steel.
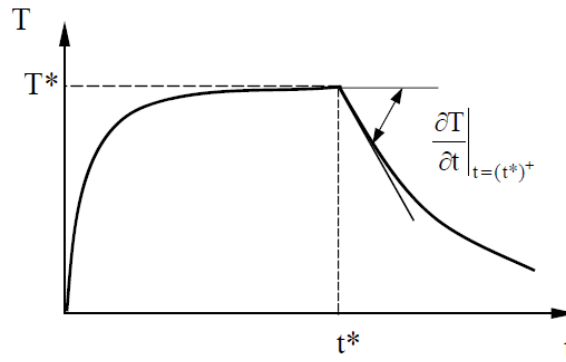
Figure 2.7: Experimental determination of cooling rate (Meneghetti, 2007).

The relation proposed by Meneghetti also shows that frequency is a factor that must be considered when understanding the temperature change that results from fatigue. Lee et al. (1993) have shown the mean surface temperature rise changes with a change in frequency. In Figure 2.8 the difference in temperature in changing the loading frequency from 1 Hz to 5 Hz is shown for AISI 1045 steel (Lee et. al., 1993). The difference in temperature rise is attributed to an abundant energy accumulation which results in a temperature rise quicker and higher than a test under the same loads at a lower frequency (Lee et. al., 1993).
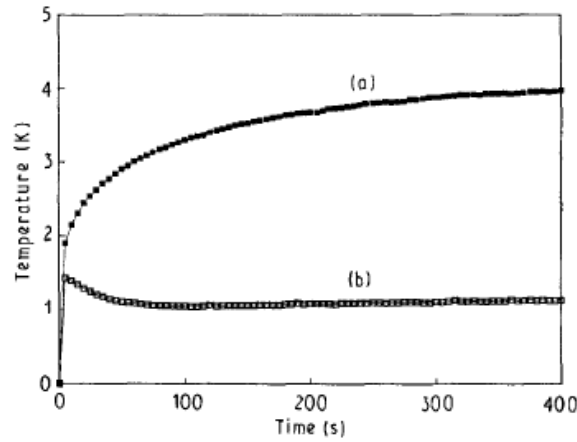
Figure 2.8: Temperature rise for loading rate (a) 400 KNs^{-1} (5 Hz), (b) 80KNs^{-1} (1 Hz) with R = 0 and σ$_a$=20 KN (Lee et. al., 1993).

Similar to frequency, different loading conditions, such as tension and compression can result in different temperature profiles. Figure 2.9 shows the different temperature profiles for loading in tension and compression. This difference is important as it could affect the results for the heat energy estimation and as will be shown in the next section, temperature is a critical factor in the estimation of the thermodynamic entropy generation.
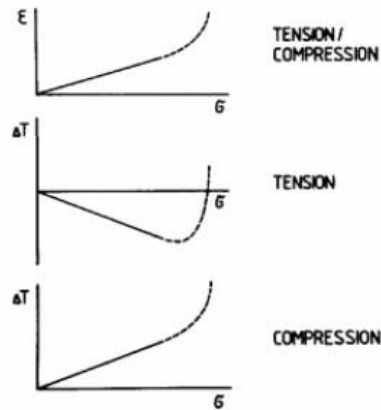
Figure 2.9: Monotonic stress strain curve and changes in temperature (Harig and Weber, 1983)

2.3.1 Thermodynamic Entropy

Recently, a combination of hysteresis energy and temperature rise methods has led to development of a method for fatigue failure assessment based on thermodynamic entropy

18

generation (Naderi et. al., 2010; Naderi and Khonsari, 2012). Entropy offers a natural measure of component degradation as a dissipative process must follow the laws of thermodynamics (Whaley, 1983; Ital'yantsev, 1984; Hansen and Schreyer, 1994; Bhattachaharya and Ellingwood, 1998; Voyiadjis et. al. 1999). Dissipative processes like, plastic dislocations (Weertman and Weertman, 1964) and fatigue (Izumi et. al. 1981; Mura, 1987; Naderi et. al 2010; Amiri et. al., 2011, Naderi and Khonsari, 2012) lend themselves to the thermodynamic energies and the concept of irreversible entropy generation.

In 1983 Whaley proposed that '*the material entropy gain during fatigue directly related to the plastic (irreversible) part of the hysteresis strain energy density is a material constant at fatigue failure*' (Whaley, 1983). Paring beliefs that the plastic portion of the hysteresis loop is irreversible (Kelly and Gillis, 1974, Wallace, 1980, Weissmann, 1981) and using discussions on the hysteresis energy conversion to heat (Halford, 1966) energy causing fatigue damage (Reifsnider and Wiliams, 1974) Whaley surmised that a thermodynamic approach, considering irreversible entropy gain, would provide a means of understanding the irreversible nature of fatigue.

Whaley's method was primarily theoretical in nature. Whaley proposed that the total entropy gain at fracture is determined by:

$$S_f = \int_0^{\varepsilon_f} \frac{\sigma}{T} d\varepsilon_p \tag{2.9}$$

where ε_f is the strain at fracture, σ is the stress, and T is the temperature. He then proposed that the local entropy rate could be estimated by:

$$\frac{\partial S}{\partial t} = \frac{f D_m(x)}{T(x)} \left(\frac{\varepsilon_p}{\varepsilon_s} \right) \tag{2.10}$$

where f is the frequency, D_m is the energy dissipated per cycle of vibration, x is the position, ε_p is the plastic strain and ε_s is the amplitude of the applied strain. The energy dissipated per cycle could be estimated as the area of the hysteresis loop. Unfortunately, no experimental

results confirming the proposed material constant for entropy gain were ever published by Whaley.

In 2011 Naderi et al. showed experimentally that, for LCF, the cumulative entropy gain for Al 6061-T6 and SS 304 was a material constant, independent of geometry, load and frequency (Naderi et al., 2011). The entropy generation described by Naderi et al. (Naderi et al., 2011) under a continuum mechanics regime is described for fatigue as the dissipation (Lematire and Choboche, 1990) divided by the temperature:

$$\dot{s}_i = \frac{\sigma : \dot{\varepsilon}_p}{T} - \frac{A_k V_k}{T} - \frac{1}{T^2} \boldsymbol{q} \cdot \boldsymbol{grad} T \tag{2.11}$$

where σ is the stress, ε_p is the plastic strain rate, T is the temperature, V_k represents any internal variable, such as hardening, A_k is the thermodynamic force associated with an internal variable, and q is the heat flux. Equation 2.11 describes the entropy generation as a function of the energy dissipation associated with plastic dissipation, the internal variables, and the thermal dissipation due to heat conduction.

In the work performed by Naderi et al. (Naderi et al., 2011), a limit of entropy generated was found as samples of Aluminum 6061-T6 (Figure 2.10) were fatigued to fracture. This result is similar to the results of the analysis performed on the P-3 aircraft (Figure 1.2) in that upon reaching the same limit, this time complete fracture, the cumulative entropies were relatively, the same.

What sets the thermodynamic entropy generation apart from using only the plastic strain energy density dissipation, which it relies heavily on, is the sudden increase in the rate of entropy flow as the sample reaches a critical damage (Amiri et. al., 2011) such as the initiation and growth of a crack. This is also seen in an increase in the surface temperature of the metal resulting from the formation of micro-cracks and an increase in the plastic deformation caused by a stress concentration at the crack tips (Jiang et. al., 2001).

Entropy has also been used to study degradation resulting from wear on metals (Ling et. al, 2002; Bryant et. al., 2008).
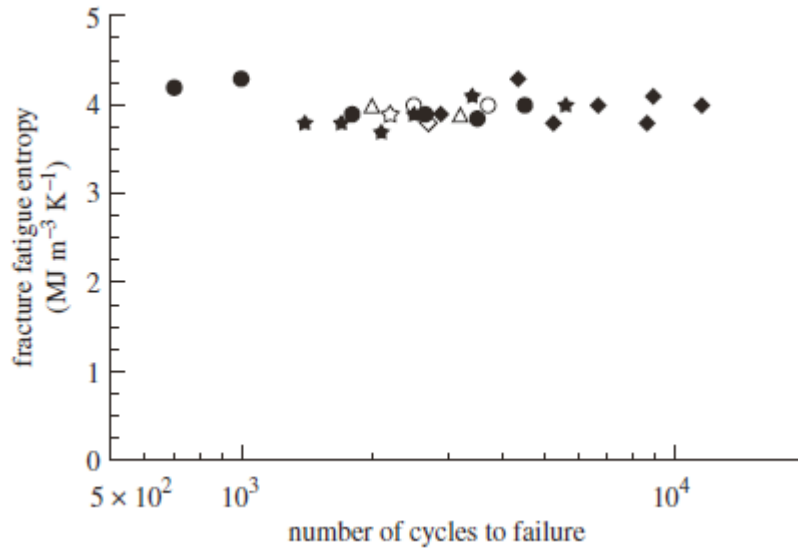
Figure 2.10: Fracture fatigue entropy for bending fatigue of Al 6061-T6 with different specimen thickness, frequencies and displacment amplitudes (Naderi et al., 2011).

As discussed above, the work performed by Naderi, Amiri and Khonsari (Naderi et al., 2011) involved primarily LCF and therefore the results relied primarily on the first term in Equation 2.11. The plastic strain energy density dissipation, represented by W_p, was calculated using Morrow's equation for the plastic strain energy density (Equation 2.2).

For the loading conditions associated with this work, where the plastic energy dissipation is small, additional terms need to be considered (Lemaitre and Chaboche, 1990). These terms are not 'new,' they are simply often assumed to be negligible and not considered when plastic deformation is high. The hysteresis energy can be split into three different parts as shown in Figure 2.11.

In Figure 2.11, the hysteresis energy is shown by the colored sections; the red area represents energy dissipated due to plastic deformation. The blue area represents energy dissipated due to the internal variables, often associated with work hardening. The green section represents the energy dissipated resulting from elastic damage, seen in the change in

the elastic modulus. As a result, the equation for the energy dissipation, from which the entropy generation equation (Equation 2.9) was constructed, should be changed to include the additional elastic damage term (Lemaitre and Chaboche, 1990):

$$\Phi = \sigma:\dot{\varepsilon}_p - A_k\dot{V}_k - Y\dot{D} - \frac{1}{T}q \cdot gradT \qquad (2.12)$$

where Y is the elastic energy release rate and D is the damage. In the literature (Lemaitre and Chaboche, 1990), the energies associated with the internal variables are often considered negligible and ignored. Similarly, the damage associated with the elastic forces is often considered to be overshadowed by the plastic deformation. However, in cases like this research, where the plastic deformation is small, these two energies can become non-negligible. In this research, the hysteresis loops are built using the stress and strains taken from strain gauges and not estimated using relations like those proposed by Morrow. Therefore, the energies associated with the internal variables and elastic damage are already captured in the hysteresis loops built from the experimental data.
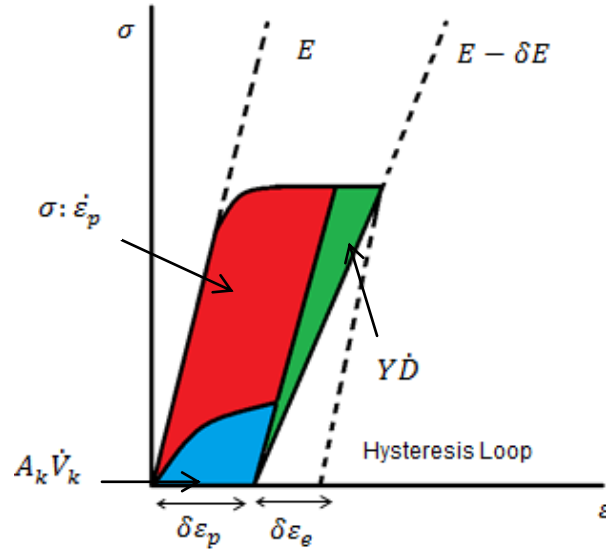
Figure 2.11: Hysteresis Energy Dissipation [Lemaitre and Chaboche, 1990]

In this research, entropy generation will be explored to determine its application as an indicator for crack initiation, as it appears the entropy generation appears at the point of complete fracture has a similar trend to the plastic strain energy density is at the point of

100% FLE in the data for the P-3 aircraft. Experiments performed in this research were developed with a focus on determining the strain energy density dissipated upon crack initiation resulting from fatigue.

Chapter 3: Experimental Procedure

3.1 Overview

In this section, an overview of the experimental procedures undertaken to generate data of plastic strain energy density and thermodynamic entropy generation will be reviewed.

3.2 Loading conditions

Fatigue tests were run under varying load ratios. Load ratios of 0, 0.1 and 0.4 with far field stresses ranging from 183 to 276 MPa were used (Appendix I). Originally global stresses were applied in percentages (55%, 65% and 70%) of the yield stress (Smith et. al., 2010). Stresses were later changed to integer MPa values—183, 214, 245, 276—to simplify the testing set up procedure. All tests used in the analysis were performed in constant amplitude load control; however a few tests were conducted in displacement control for comparison to the results seen in load control and to search for any differences. No significant difference in results was observed. All tests were performed under tension loading. This was done for two primary reasons, one to represent similar aircraft loadings and the second to simplify testing conditions. An area on the wing root of the P-3C aircraft typically sees tension dominated loading (Iyyer, et. al, 2009). For the second reason, the length of the test specimen coupon made it possible to cause bending and buckling in compression loading. Each test was conducted at room temperature with a frequency of 2 Hz. Frequency was not varied as it has been observed that fatigue life is not highly dependent on frequencies up to a frequency of 200 Hz (Morrow, 1965; Liaw et. al., 2002).

3.3 Test Specimens

Initial test specimens were designed with input from NAVAIR to better represent similar tests supporting the development of life management models for the P-3C aircraft (Iyyer et. al., 2009.) Coupons were made out of Al 7075-T651 (Table 3.1) representing material used in aircraft wing lower surfaces (Iyyer et. al., 2009). The dimensions for the original coupons are shown below in Figure 3.1. The original coupons were developed with three holes which allowed for multiple opportunities for cracks to initiate during a single test. As expected during most tests cracks initiated at the holes at different cycles. Originally, surface crack measurements were made and tests were continued until the sample failed due to crack initiation, growth and ultimately rupture resulting from one of the holes (Smith et. al., 2010). A difficulty introduced through the use of the coupon design was in the ability to properly take strain data around each of the holes for estimation of the strain energy density. Each hole provided not only one, but two locations of stress concentration for a crack to initiate. As will be discussed below, attempting to properly measure the strain at twelve locations, thirteen if the far field strain measurement was desired, was not possible with the tools available. The twelve locations come from attempting to measure the strain on the two edges of each hole, and both sides of the coupon since, while it was most likely for the crack to initiate near the center of the notch, it was possible a crack could favor a single side and the difference in strains might affect the strain energy density estimations. As the focus of these experiments was to estimate the strain energy density required for crack initiation the three-hole design was later changed to a single hole.
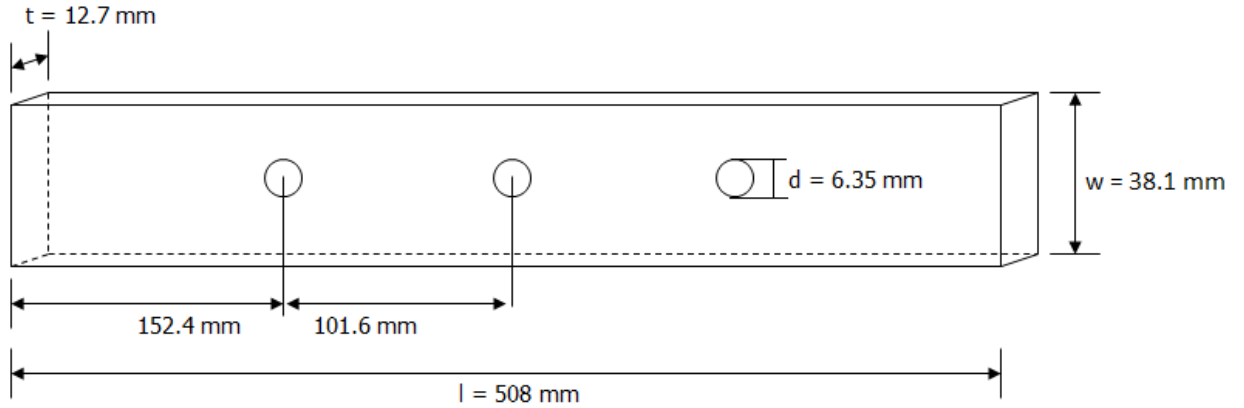
Figure 3.1: Initial Al 7075-T651 Three-Hole Sample Dimensions

The dimensions for the single-hole coupons are shown in Figure 3.2. The change in dimensions from a specimen coupon with three holes to a single-hole allowed the focus to be centered on the initiation of a single crack. While this lowered the number of points to track strain values, it still required four strain measurements to be taken around the single hole in the coupon. While finite element modeling (FEM) was performed for comparison with strain values observed experimentally, this was not used as a means to cover the positions where strain measurements could not be taken experimental for the single and three-hole coupons as the differences between the coupons was also sought for the later estimation of the difference uncertainties to be included in the study. Similar to the three-hole coupon design, the number of points to take strain measured increased by one if the far field strain was required. One more modification was made to the coupon dimensions before the data gathering phase of this study was completed.

Table 3.1: Al 7075-T651 WT % Composition

	Si	*Fe*	*Cu*	*Mn*	*Mg*	*Cr*	*Zn*	*Ti*	*Al*
Actual	0.07	0.24	1.4	0.02	2.7	0.19	5.9	0.3	Remainder
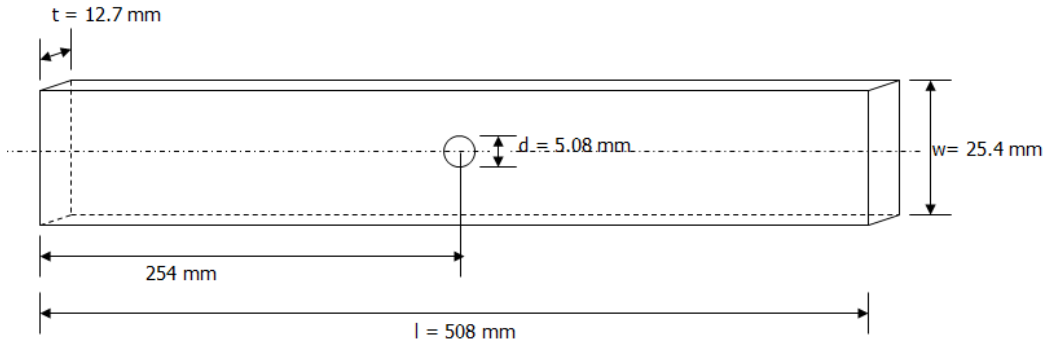
Figure 3.2: Al 7075-T651 Single-Hole Sample Dimensions

The final coupon dimensions used in this study are shown below in Figure 3.3. The hole was removed and replaced with a notch on the edge of the sample with the same radius as those of the hole in the single-hole coupon. This change improved the ability to view the initiation of the crack considerably. Previously, to observe the initiation of a crack, unless it started on the edge of the coupon, great effort had to made to see into the hole of the sample and watch and observe the minuscule movements of a surface rupture on the inner surfaces of the hole. To be discussed later in this section, with respect to the temperature measurements made in this study, the close proximity the observer had to be to the coupon to make these visual inspections paired with the limited temperature increase resulting from fatigue, introduced considerable noise into the temperature measurements. This final change in sample dimensions also lowered the number of points the strain data needed to be taken to at most three, including the far field strain measurement.

Placing the notch on the side of the coupon also allowed for the use of an Infrared camera to be used to observe the change in temperature at the location of crack initiation.
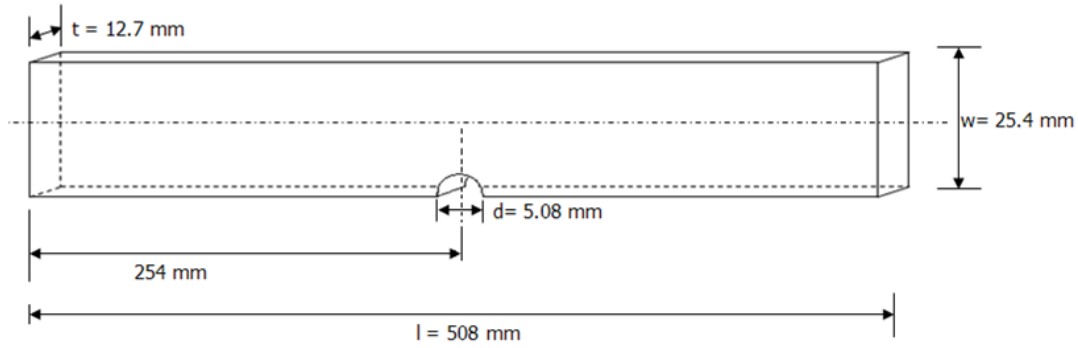
Figure 3.3: Al 7075-T651 Edge Notch Sample Dimensions

Near the end of the data gathering phase of the study, a new sample design was studied for comparison. The dimensions for the dog-bone sample are shown in Figure 3.4. The dog-bone sample was added to the analysis to address a number of questions. One such question was to see if the larger notch area of the original samples provided a larger area for surface flaws to influence the results. Another question was to see if such a great change in sample dimensions would change the estimated cumulative strain energy density and thermodynamic entropy results. These questions will be answered in the results discussed in the following section.

3.4 Data Collection

A number of measurements were taken during the experiemental process of this study. These include stress and strain for the development of the strain energy density and the surface temperature of the coupons for the development of the heat energy and thermodynamic entropy.

3.4.1 Stress

Stress data was developed using the load data recorded by the load cell attached to the upper grip on the MTS load frame and the coupon body. The load cell is capable of measuring loads from -100 kN to 100kN. The load cell is calibrated to $\pm$ 1% (Instron, 2012.)

The stress values being recorded are the stresses measured by the load which are considered to be far field stresses due the distance between the load cell and the notch in the sample. Therefore, these far field values needed to be corrected to include the effect introduced by the notch placed on the coupon.
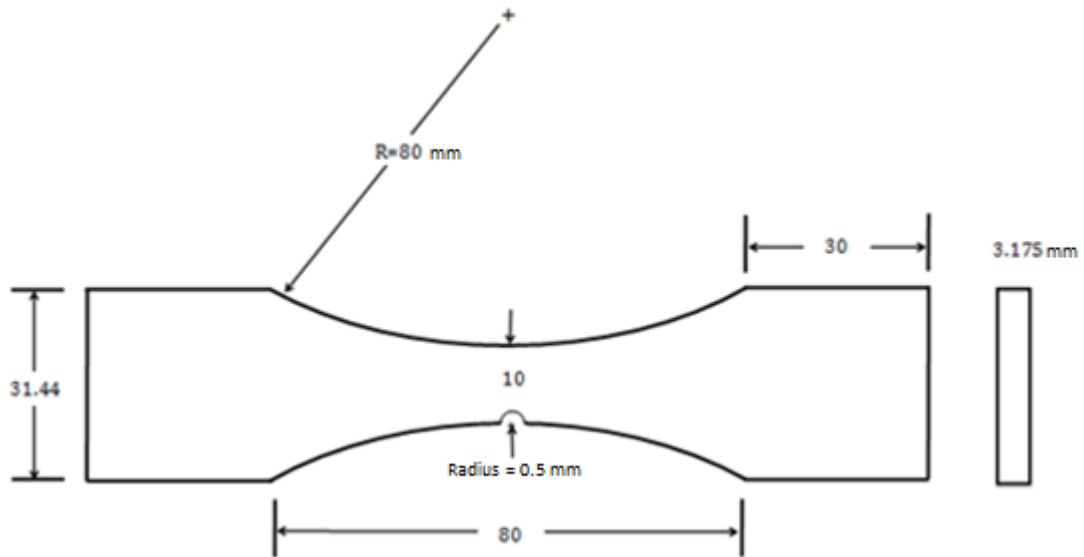
Figure 3.4: Al 7075-T6 Dog-Bone Sample Dimensions

3.4.2 Notch effect

A notch was added to the test coupons to introduce a stress concentrator for several reasons: The original coupons were designed to be similar to those used in the P-3C aircraft life management study (Iyyer et. al., 2009) and have a geometry that could be relatable to the condition seen on those aircraft. Additionally, experimentally it simplified the measurement technique because it limited the location that needed to be observed for crack initiation. In an unnotched specimen, a crack could initiate at any position on the sample, and could possibly be missed. As a result, the stress at the notch needs to be modified by the elastic stress concentration factor, K_t, such that:

$$\sigma_{notch} = \sigma_0 K_t \tag{3.1}$$

where σ_0 is the far field stress.

Initially, empirical relations for the different dimensions of the notches used in this study were used to estimate the value of K_t (Pilkey and Peterson, 1997). For the single-hole coupon K_t could be estimated by:

$$K_t = 2 + 0.284\left(1 - \frac{d}{H}\right) - 0.6\left(1 - \frac{d}{H}\right)^2 + 1.32\left(1 - \frac{d}{H}\right)^3 \qquad (3.2)$$

where d is the diameter of the hole and H is the width of the specimen. The resulting K_t is 2.96.

A similar equation for a coupon with a notch on a single edge:

$$K_t = 3.065 - 8.871\left(\frac{t}{H}\right) + 14.036\left(\frac{t}{H}\right)^2 - 7.219\left(\frac{t}{H}\right)^3 \qquad (3.3)$$

which results in a K_t of 2.31.

Unfortunately, these estimations are for when the stress at the notch stays within the elastic region. The yield stress for the Al 7075-T651 is 503 MPa (Metals Handbook, 1990), when matched against the values for K_t and the stresses used in this study, the stress at the notch was found to surpass the yield stress. Therefore, to determine the appropriate stress concentration factor to account for the change in stress caused by the notch, FEM was used to determine the stress concentration factors to be used under different loading stresses.

The FEM program Abaqus (Abaqus) was used in this study to model the coupons and to determine the stresses at the notch when the coupons were load to varying stresses. Figure 3.5 shows an example of the FEM results. The results allowed for an estimation of the appropriate factor to be used with different stresses. Table 3.2 shows the different stress concentration factors paired with the far fields stresses.
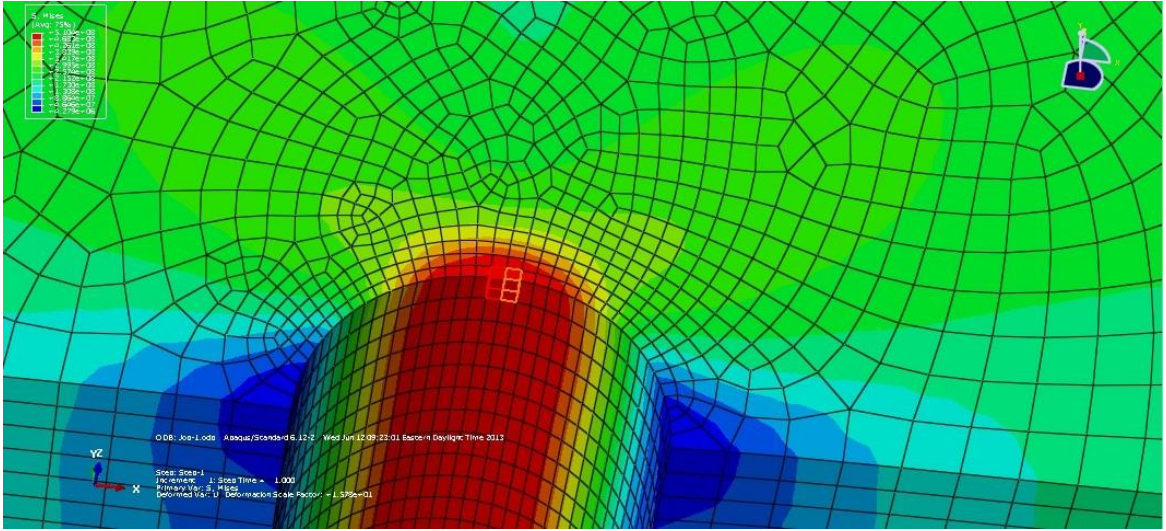
Figure 3.5: FEM analysis of stress at the notch of coupon for 214 MPa.

The results show how the concentration factor begins to decrease as the stress

is increased due to the resulting initiation of plasticity. The stress concentration

values presented in Table 3.2 were multiplied by the stress values obtained using the

load data captured by the MTS load frame. The load data was recorded at a rate of

200 Hz to ensure that the entire hysteresis loop would be appropriately captured. To

develop the hysteresis loop the strain data must also be taken.

Table 3.2: Stress concentration factors

σ (MPa)	K_t (Abaqus)
183	2.73
214	2.37
245	2.10
275	1.88

3.4.3 Strain

Over the course of this study strain data was taken by a number of different

means. During the initial tests, performed on the three-hole coupons, the strain data

was estimated using the displacement of the grips reported by the MTS machine.

However, a more precise measurement of strain at the notch over the far field strain was sought.

3.4.1 Strain Gauges

For a number of experiments, strain gauges were used to measure the strain around the hole and notches of the coupons. The gauges used in this study were WD-DY-062AP-350, 350 ohm strain gauges. Strain data was taken at a rate of 200 samples per second.

The use of strain gauges was limited to at most 4 gauges per experiment. For the single-hole coupons, strain gauges were placed so that three gauges were placed around the hole (See Figure 3.6a) and the fourth gauge was placed a distance above the hole so that the far field strain could be measured. For the edge notch coupons, the gauges were arranged in an array allowing for the strain to be monitored at various distances from the hole (See Figure 3.6b)

A LabView program was developed to record the strain gauge data. Since the LabView program was not directly integrated in the MTS load frame software, the two data sets did not match up completely. Hysteresis loops built from stress data taken from the MTS load frame and LabView strain gauge measurement system resulted in hysteresis loops eventually becoming out of sync with each other after a short amount of time. Therefore, the far field strain measurement was used to estimate the far field stress using Hooke's Law:

$$\sigma = E\varepsilon.$$
(3.4)

This estimation of the stress allowed for the stress and strain data to be kept in sync and the resulting hysteresis loops would not shift out of time. The use of strain gauges presented a number of challenges. Often, during testing a strain gauge would fail. If the failed

gauge was the far field gauge, that particular test would likely become useless as it would become difficult to determine stress values for use in the determination of the hysteresis loops. Sometimes during the installation of the gauges to the coupon surface, the connecting wires would detach rendering the gauge useless. This required the gauge to be sanded off completely to make room for a new gauge to be attached. Additionally, the location of the strain gauges, how close or far they were placed near the edge of the hole or notch could influence the results. As a result, a relation was empirically developed to calculate the strain at the hole using strain data from gauges located away from the notch.
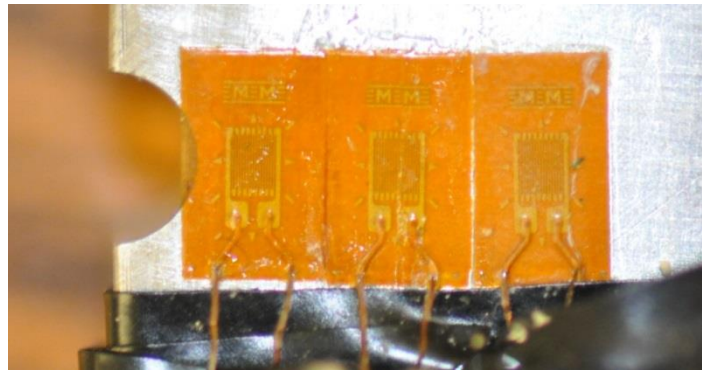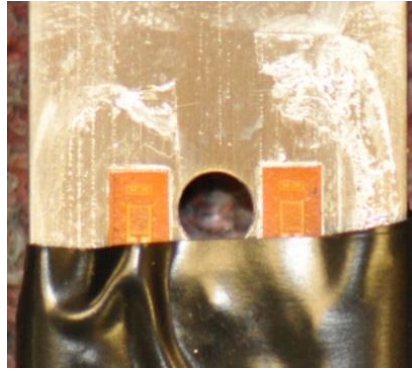
Figure 3.6: Strain gauge placement a) single-hole b) edge notch

Using the relation for the determination of the stress at a notch (Dally and Riley, 1978):

$$\sigma_{xx} = \frac{\sigma_0}{2}\left(2 + \frac{a^2}{x^2} + \frac{3a^4}{x^4}\right), \tag{3.5}$$

Where a is the radius of the hole and x is the distance from the center of the hole, a similar relation for the strain was assumed:

$$\varepsilon_g = \frac{\varepsilon_0}{2}\left(2 + \frac{a^2}{x^2} + \frac{3a^4}{x^4}\right)$$ (3.6)

and, therefore, the strain at the edge of the notch would be:

$$\varepsilon_h = \frac{\varepsilon_0}{2}\left(2 + \frac{a^2}{a^2} + \frac{3a^4}{a^4}\right) \rightarrow \frac{\varepsilon_0}{2}(2 + 1 + 3) \rightarrow 3\varepsilon_0$$ (3.7)

combining equations 3.6 and 3.7 the strain at the hole, given the strain at the gauge is:

$$\varepsilon_h = \frac{\left(\dfrac{2\varepsilon_g}{2 + \frac{a^2}{x^2} + \frac{3a^4}{x^4}}\right)}{2}\left(2 + \frac{a^2}{a^2} + \frac{3a^4}{a^4}\right)$$ (3.8)

Edge notch coupons with the strain gauges arranged in an array (as seen in Figure 3.6b) were used to determine how the strain field progressed on the surface of the sample Using the strain gauge values from the strain gauges and additional values taken from the FEM analysis, the model parameters in equation 3.8 were updated to better match the samples used in this study (Figure 3.7)

The resulting relation used to extrapolate the strain values determined using the gauges to the location of the hole is shown in equation 3.9:

$$\varepsilon_h = \frac{\left(\dfrac{2.278\varepsilon_g}{1.827 + \frac{a^2}{x^2} + \frac{2.955a^4}{x^4}}\right)}{2.278}\left(1.827 + \frac{a^2}{a^2} + \frac{2.955a^4}{a^4}\right)$$ (3.9)

Which, with a being a constant, reduces to:

$$\varepsilon_h = (2.538)\left(\frac{2.278\varepsilon_g}{1.827 + \frac{a^2}{x^2} + \frac{2.955a^4}{x^4}}\right)$$ (3.10)

For coupons utilizing strain gauges, the resulting notch strain values are independent of strain gauge placement on the sample because Eq. 3.10 can be used to extrapolate the notch strain regardless of strain gauge location. Owning to the challenges posed in using strain gauges, an extensometer was ultimately chosen to capture strain data for the development of the hysteresis loops.

3.4.5 Extensometer

The extensometer used was an Epsilon Model 3542 extensometer with 25 mm gauge length. The extensometer was placed around the notch as shown in Figure 3.8. The extensometer was connected to the MTS load frame and the resulting data was taken simultaneously with the stress data reported for the load. Therefore, there were no syncing issues between the stress and strain data. The extensometer also eliminated many of the challenges seen when using strain gauges. The extensometer did not require a lengthy application process and could easily be attached to the samples immediately before the experiment.
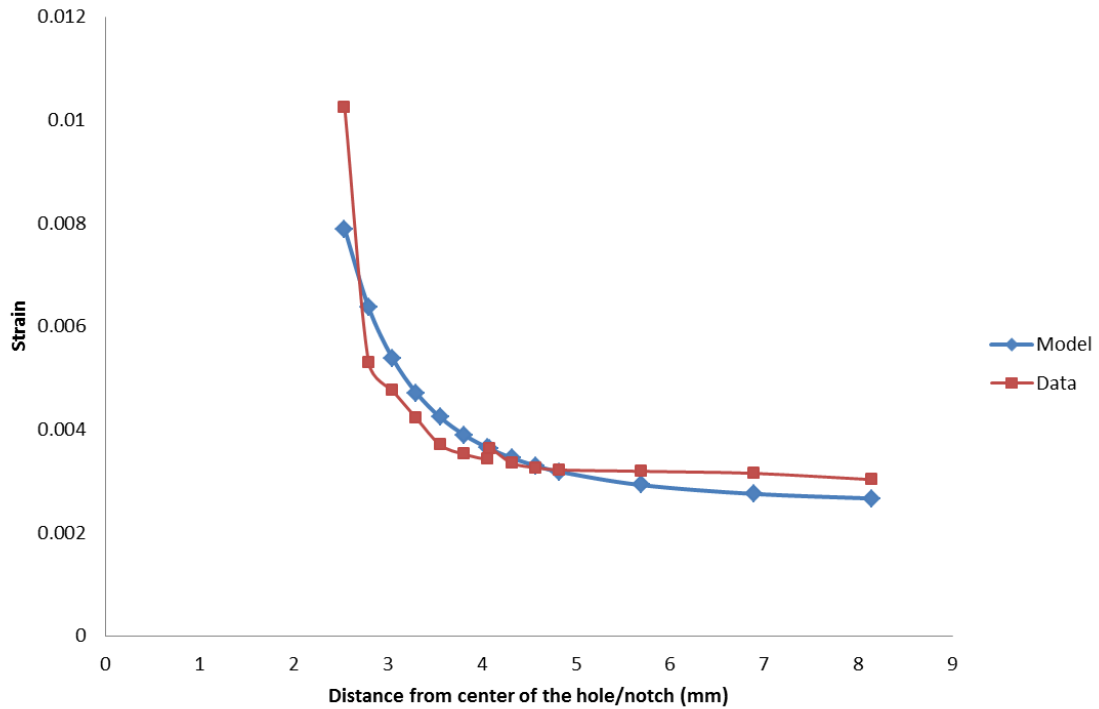
Figure 3.7: Strain gradient model parameter fitting using experimental and FEM data.
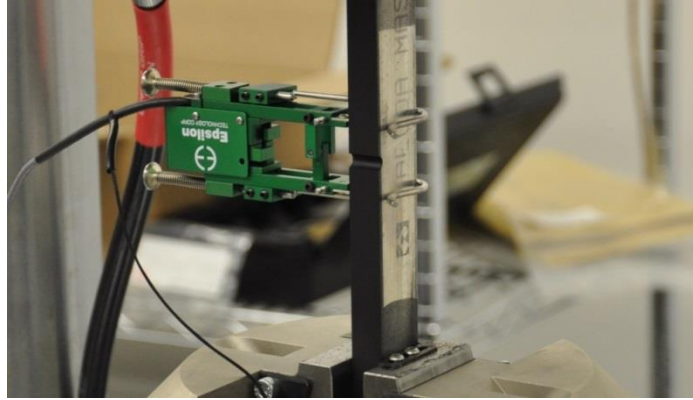
Figure 3.8: Extensometer.

The strain taken by the extensometer is the far field strain, so a modification needed to be made. Initially, a single multiplication factor was applied to modify the strain measured from the extensometer to a value more representative of the strain at the notch. It was here that an observation was made with respect to the difference in strain depending on the peak loading conditions. It was observed (See Figure 3.9) that the ratio of the increase in strain was not the same as that seen in the load due to plasticity. Therefore, the extensometer had to be modified based on the individual loading conditions. Data taken from the previously used strain gauges was helpful in modifying the extensometer results.
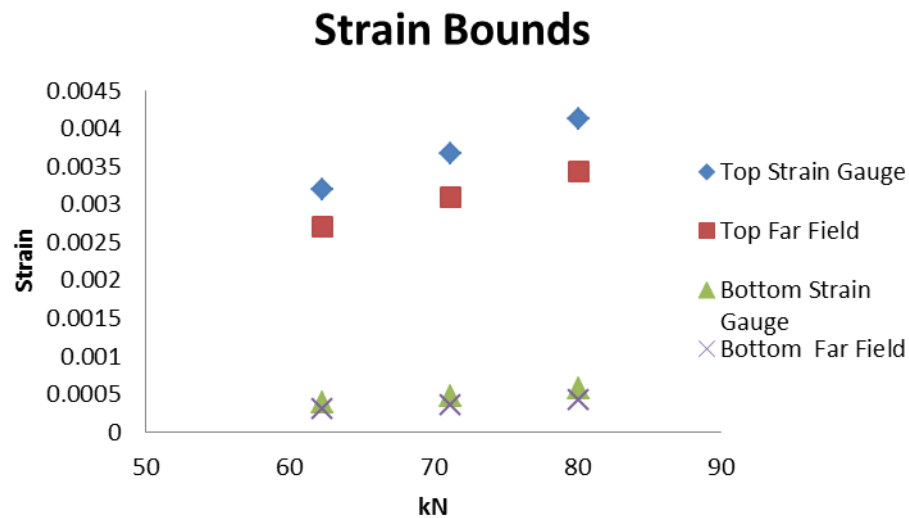
Figure 3.9: Strain values for different loading conditions.

With the stress and strain data taken from these experiments, the area of the hysteresis loops was calculated (See Figure 3.10) and later used for the determination of the plastic and elastic strain energy density.
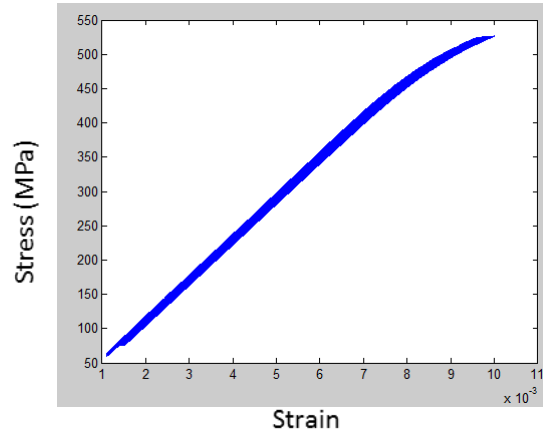
Figure 3.10: Sample hysteresis loop.

The determination of the strain energy density was performed using a very simple numerical method. Stress and strain data was taken at a rate of 100 samples per cycle. The strain energy density, determined by taking the area under the upper and lower bounds of the hysteresis was determined using the midpoint method. In Figure 3.11, the estimation of the total and elastic strain energy density is depicted graphically. The plastic strain energy density is determined by subtracting the elastic strain energy density from the total strain energy density. The total, plastic and elastic strain energy density is now available for analysis. The MATLAB code for the determination of the total, plastic and elastic strain energy density is included in Appendix 1. The code also contains the conversion of the MTS load to stress of the specimen, including the K_t factor. Modifications to correct the extensometer strain measurements are also included in the attached code. With all the measurements for the determination of strain energy density presented, one additional property, sample surface temperature must be measured to determine the thermodynamic entropy.

a) **b)**
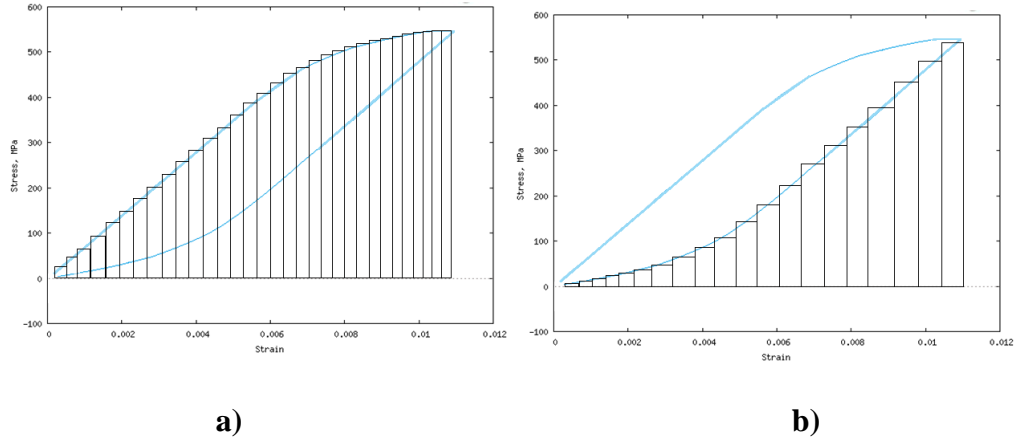
Figure 3.11: Representation of energy calculated from experimentally developed hysteresis loops a) total strain energy density, b) elastic strain energy density. (not to scale)

3.5 Temperature

For the calculation of the thermodynamic entropy, temperature measurements were taken by three different methods: thermocouple, IR sensor and IR camera.

3.5.1 Thermocouples

Initially, high-speed, high-resolution T-type thermocouples were used to record the surface temperature evolution of the specimen around the crack tip during the fatigue loading. A National Instrument USB-9211 data acquisition device was used to gather thermocouple data. T type thermocouples have an accuracy of T <0.05 °C at room temperature (15°C - 35°C).

The placement of the thermocouples on the single-hole coupon is shown below in Figure 3.12. Three thermocouples were used for the measurement of temperature. Two thermocouples were placed on the coupon, one adjacent to the edge of the hole where a strain gauge was not placed and a second on the side of the sample. A third thermocouple was placed adjacent to the coupon for the measurement of the ambient temperature. The placement of the thermocouples allowed for measurements to be made of the change in temperature regardless of which side of the hole the crack initiated on. For the coupons with

38

the edge notch, two thermocouples were used, one placed on the face opposite the face with the strain gauge array and a second was used to measure the room temperature around the coupon. Using thermocouples presented a number of challenges. One side of the thermocouples was covered with an adhesive used to keep the thermocouple attached to the surface of the specimen. Initial use of the thermocouples showed that during fatigue, the thermocouples would delaminate from the surface of the coupon as the adhesive on the thermocouple became significantly less effective with continued use of the thermocouple. Two actions were taken to mitigate the delamination of the thermocouples from the coupon surface. As seen in Figure 3.12, the thermocouples were held in place on the surface of the sample by using the stem of a q-tip. In order to ensure that the thermocouple maintained good contact with the surface, a high thermal conductivity paste was placed between the thermocouple and surface of the coupon. This ensured that any temperature change the surface of the coupon experienced, the thermocouple experienced the same. Another challenge posed in using thermocouples was the inability to monitor the temperature at the point of crack initiation. Most cracks initiated on the inner surface of the notch (or hole) and the thermal couple was unable to detect the temperature change after it conducted through the coupon. The first attempt to account for this was to model the temperature at the point of observed crack initiation using the FEM software.

Attempts to model the temperature at the point of crack initiation were undertaken using the FEM software COMSOL (COMSOL). A model of the coupon (see Figure 3.13c) was constructed using the thermal properties of Al 7075-T651

Table 3.3 –Al 7075-T651 thermal properties (Metals Handbook, 1990)

Property	Value
Specific Heat Capacity (J/g·C)	0.96
Thermal Conductivity(W/m·K)	130
Density (g/cc)	2.81
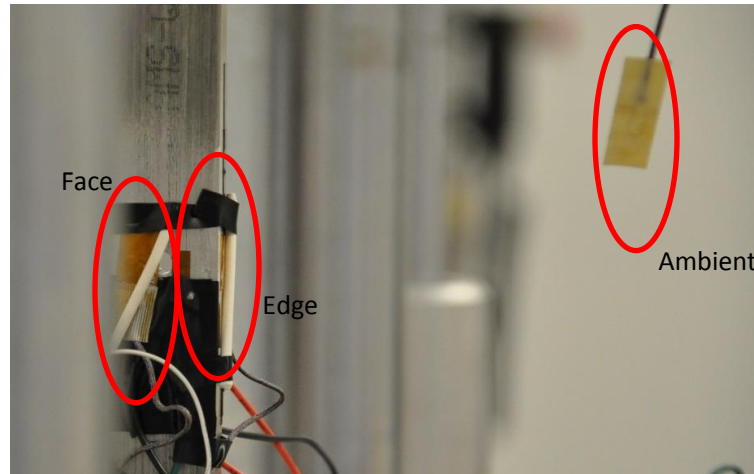
Figure 3.12: Singe hole coupon thermocouple placement.

Within the model, a small heat source was placed at the suspected position of the crack initiation. The point heat source was then modified until the surface temperature matched that of the thermocouple in the experiment. This allowed for an estimation of the temperature at the location of suspected crack initiation.

c)
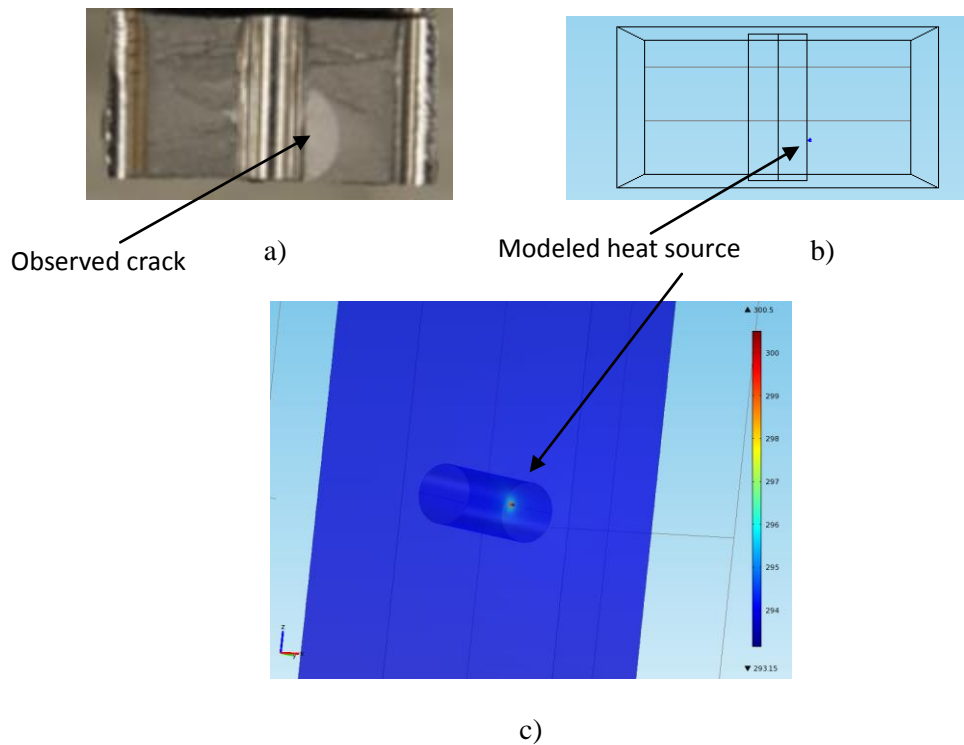
Figure 3.13: a) Fracture surface showing small crack, b) FEM depiction of location of crack initiation, c) FEM model of point heat source depicting the location of crack initiation.

Uncertainties introduced by the use of modeling the temperature at the location of suspected crack initiation are expected to be limited. This is due to Aluminum's high thermal conductivity, so the temperature difference between the thermocouple and suspected crack initiation site is minimal. Additionally, another means of determining the temperature at the location of crack initiation confirmed the observation that the temperature change was relatively small on the surface and at the location of crack initiation.

3.5.2 Infra-red temperature measurements

Two means of measuring the temperature evolution of the specimens during fatigue experiments involved using a non-contact infra-red (IR) sensor and an IR camera. Most of the temperature measurements were taken using a non-contact IR sensor.

3.5.2.1 IR sensor

Most temperature data was taken using a non-contact Omega OS151 Infra-Red (IR) temperature transmitter with a temperature range of -40 to 1000°C and a 240ms response time. The IR sensor was placed so that it would view the coupon from the side (See Figure 3.14), similar to the placement of the thermocouples. The position on the sample that was viewed by the IR sensor was painted black to increase the surface emissivity. Data taken by the IR sensor was recorded by hand. The change in temperature due to the thermoelastic effect, the small change in temperature during each cycle, was not recorded, but the increase in the mean temperature, which is needed for the analysis, was recorded.
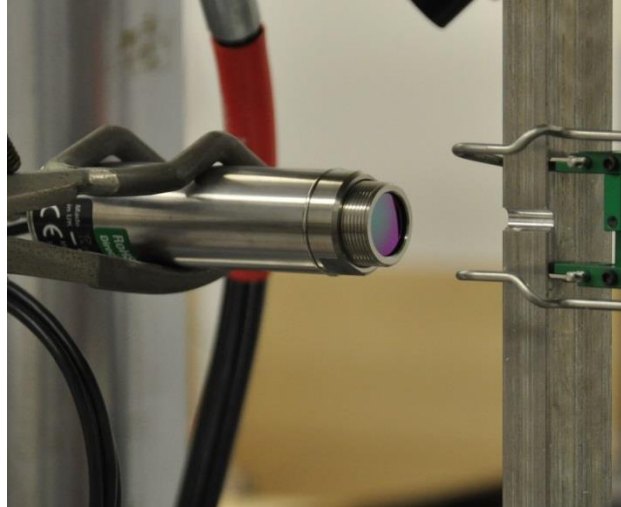
Figure 3.14: IR sensor placement.

3.5.2.2 IR Camera

Previous studies on thermodynamic entropy and fatigue have made use of an IR camera to monitor the temperature evolution of the specimen. Initial results using an IR camera seemed promising.

A single experiment was run at the Naval Research Laboratory (NRL) with the assistance of Dr. Robert Bayles. This experiment was conducted on an edge notch coupon. An important note should be made, in this single experiment there is no reference to the actual temperature. In Figures 3.15-3.18, the 'temperature' profiles were not calibrated. The IR camera at the NRL had not been used in a number of years and unfortunately, the camera ceased to function after this single experiment.

From this single IR camera test, it appeared the use of an IR camera might be able to determine when the crack is starting to initiate. Figure 3.15 shows the sample early in the test, before a crack has started to initiate.
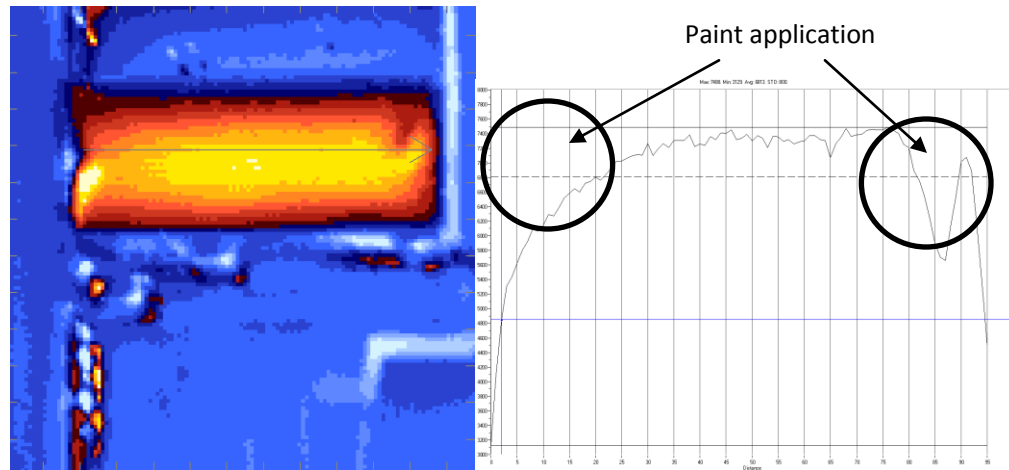
Figure 3.15: (a) Temperature* field in notch on specimen shortly after start of test (b) Temperature* profile along centerline of specimen notch at start of test

In Figure 3.15, we can see that the temperature profile remains constant along the center axis of the specimen. In Figure 3.15b, the 'temperature' profile along the line at the center of the specimen seen in Figure 3.15a is shown. The dip seen in the 3.15b is a result of poor paint application. The samples must be painted to reduce reflections and differences in the emissivity of the surface. What appears to be an area of low temperature on the right side of both Figure 3.15a and b is the result of uneven paint application.

As the test progresses and a crack begins to form, the change in the coupon resulting from the crack can be seen in the temperature profile (Figure 3.16.). In Figure 3.16a, there appears to be a difference in temperature, just right of center, in the notch of the specimen and in the temperature profile (Figure 3.16b), a similar dip was observed. This dip in the profile could be used to determine the point of crack initiation before it can be seen visually. Earlier in the test, this dip is not seen in the profile (Figure 3.17b) before it can be recognized in the temperature profile (Figure 3.17a.)

Suspected point of crack
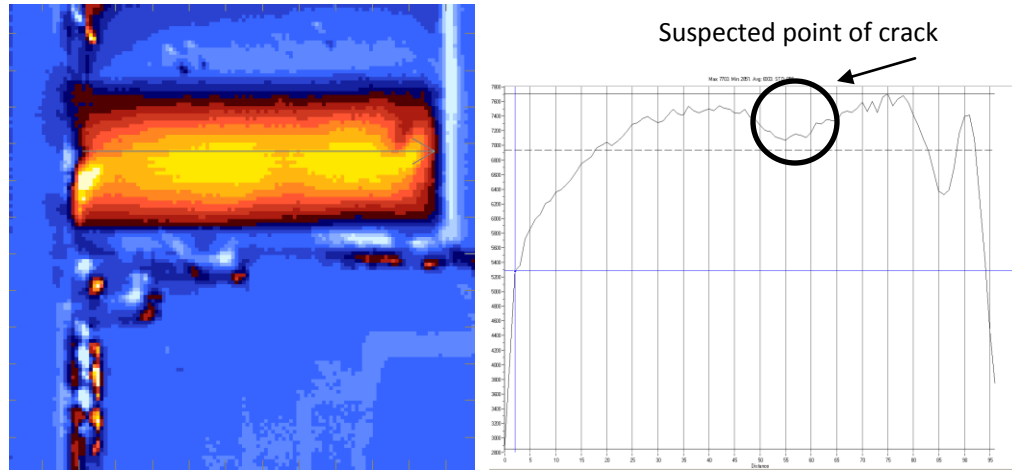
Figure 3.16: (a) Temperature* field in notch on specimen suspected to be after point of crack initiation (b) Temperature* profile along centerline of specimen notch suspected to be after point of crack initiation

The sample was allowed to progress until there was no doubt a crack in the specimen had initiated. In Figure 3.18, the effect of the presence of crack in the sample was observed in the IR camera output.
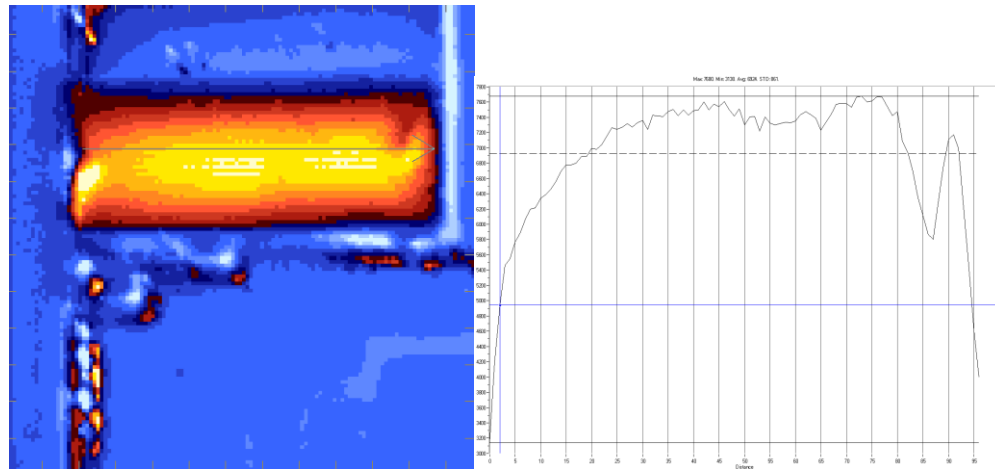
Figure 3.17: (a) Temperature* field in notch on specimen suspected to be around point of crack initiation (b) Temperature* profile along centerline of specimen notch suspected to be around point of crack initiation
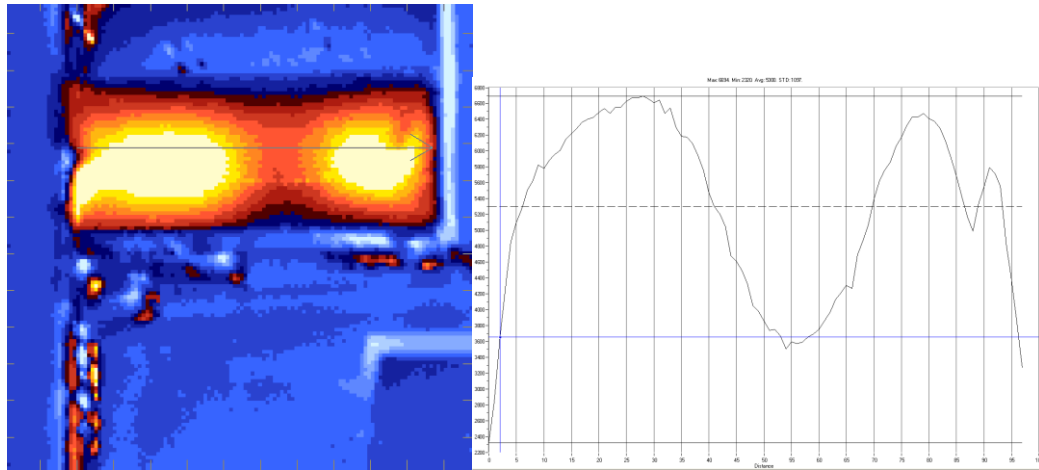
Figure 3.18: (a) Temperature* field in notch on specimen at the end of the test (b) Temperature* profile along centerline of specimen notch at the end of the test

While these initial results look promising, after this single experiment the IR camera failed, limiting the usefulness of these results.

Additional IR camera tests were performed at the University of Maryland (UMD) using an IR camera (Figure 3.19) provided by the Thermal Management of Photonic and Electronic Systems (TherPES). The IR camera used was a FLIR Silver 660 MW with a resolution of 320 x 256 pixels with accuracy of ±1% with a frame rate up to 100 Hz. The initial hope was that this IR camera would, as observed in the NRL experiment, allow for a more accurate determination of the cycle for crack initiation when compared to the visual inspection method. Unfortunately, the result seen at NRL appears to be the only time, crack initiation was clearly seen by the IR camera. In one instance (Figure 3.20) the crack initiation was observed by the IR camera, but it was so small, it was not recognized to be crack initiation until after the completion of the experiment. In Figure 3.20, the profile of the fractured sample is compared with the results observed from the IR camera. During the experiment, the profile seen as a faint blue-white line in the IR camera results (Figure 3.20b) was not observed during the experiment, but only after when viewed later with significant manipulation of the recorded results.

45

Figure 3.19: FLIR IR Camera
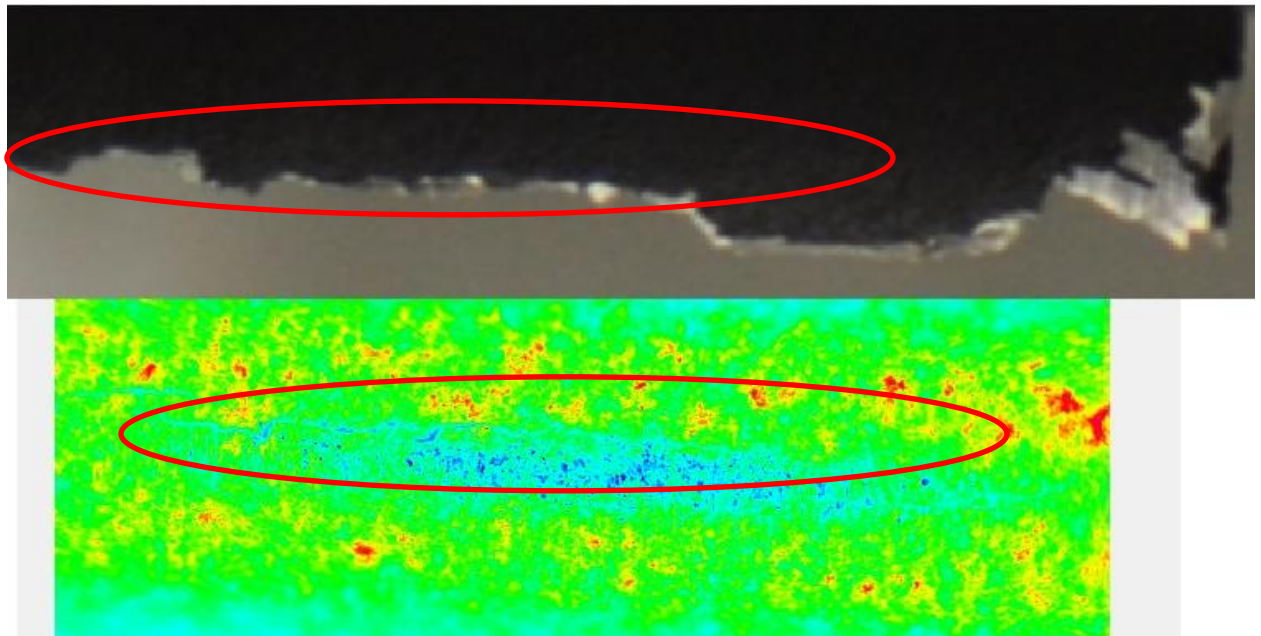
Figure 3.20: a) Fractured specimen profile, b) comparison of IR results to sample.

While the IR camera did not increase the ability to accurately observe the cycle for

crack initiation—which may not be terribly important and is discussed in the next section—

the IR camera was still able to capture the temperature evolution of the specimen (Figure 3.21). In Figure 3.21, the increase in the temperature as the coupon is fatigued is shown. The sample starts at room temperature and then increases, quickly initially, then reaches near steady state as the difference between the heat energy related to the hysteresis effect and the heat loss from convection equalize. The temperature finally increases rapidly as the specimen fails.

In Figure 3.21, short jumps seen in the temperature are a result of a person passing near the specimen and the camera picking up the small amount of heat they add to the surface of the specimen.
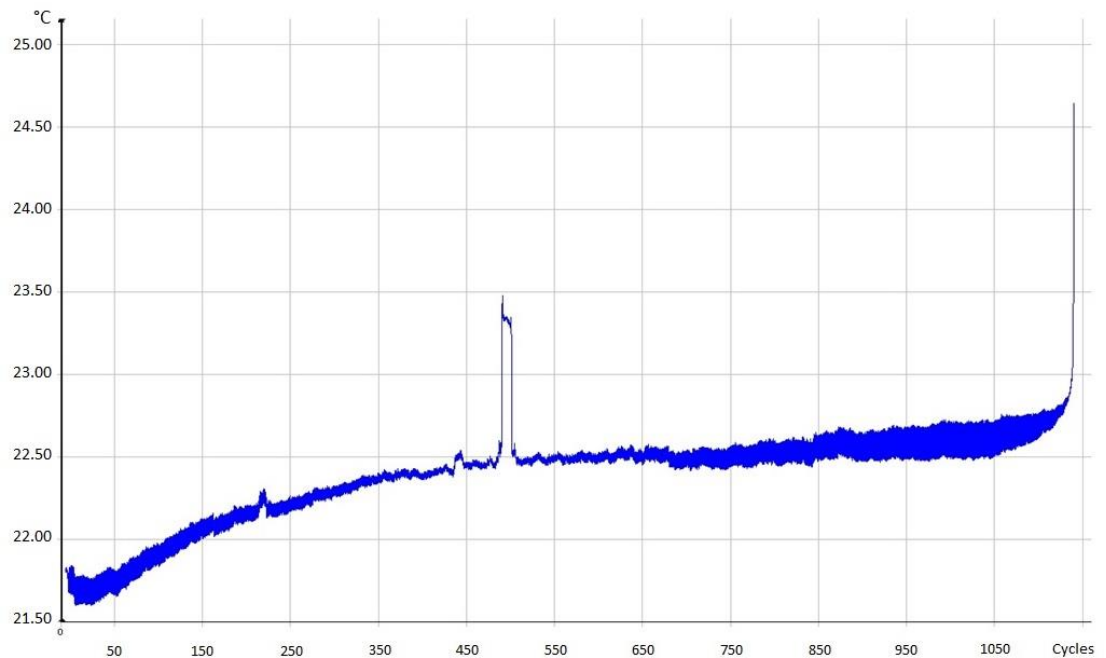
Figure 3.21: Example of a specimen temperature evolution

3.6 Crack initiation

3.6.1 Back cut

With the focus on crack initiation, action was taken to lessen the time required to complete an experiment. With an assumed crack initiation size of 0.25 mm (0.01") once a

crack was visually observed, the experiment was stopped and the coupon was removed from the test frame. Then the edges of the coupon were 'back-cut' to a point judged to be just short of the fatigue crack initiation. This back cutting removed a significant portion of the coupons cross-sectional area, weakening the coupon. The coupon was then placed back in the load frame and pulled apart. This allowed for the fracture surface of the specimen to be observed without having to wait for the specimen to reach full fracture.

3.6.2 Walkers equation

Once the crack was large enough to be seen visually, without the aid of a microscope, the crack length was already larger than the required 0.25 mm length designated as crack initiation. Therefore, an attempt to determine how many extra cycles took place between 'crack initiation' and the end of the experiment was made using a modified version of Walker's Equation (Levey, 1986). The equation used is shown below:

$$\frac{da}{dN} = C((1-R)^m K_{MAX})^n, \tag{3.11}$$

Where C, m and n are material constants, R is the loading ratio, and K is the stress intensity factor. Tested samples were examined through photographs obtained from a Nikon D90 digital camera. Measurements of the crack length were determined based on image analysis software, ImageJ (Rasband, 2008) as shown in Figure 3.22. Subjectively determined ImageJ measurements were made to the nearest pixel of crack size between the edge of the notch and the edge of the crack were made. For each photograph, a ratio of pixels to millimeters was calculated. To understand the scatter of the measurements, each measurement was made 5 times and averaged. This step was performed in an attempt to determine the crack size with more accuracy and to provide information for the determination of the contribution to experimental uncertainty through use of these measurements.
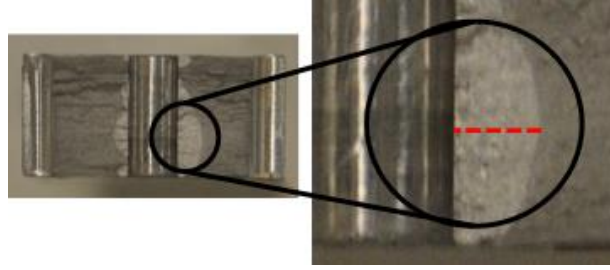
Figure 3.22: Crack length measurement

Modified Walker equation parameters, *C* and *n*, were fit using experimental results taken for this study at loading ratios of 0.0, 0.1, and 0.4. The parameter *m* was taken from literature values for Al 7075 (Levey, 1986, Zhao, 2008). The values used for fitting are shown below in Figure 3.23. The resulting mean values used for *A*, *n*, and *m* are shown in Table 3.4.
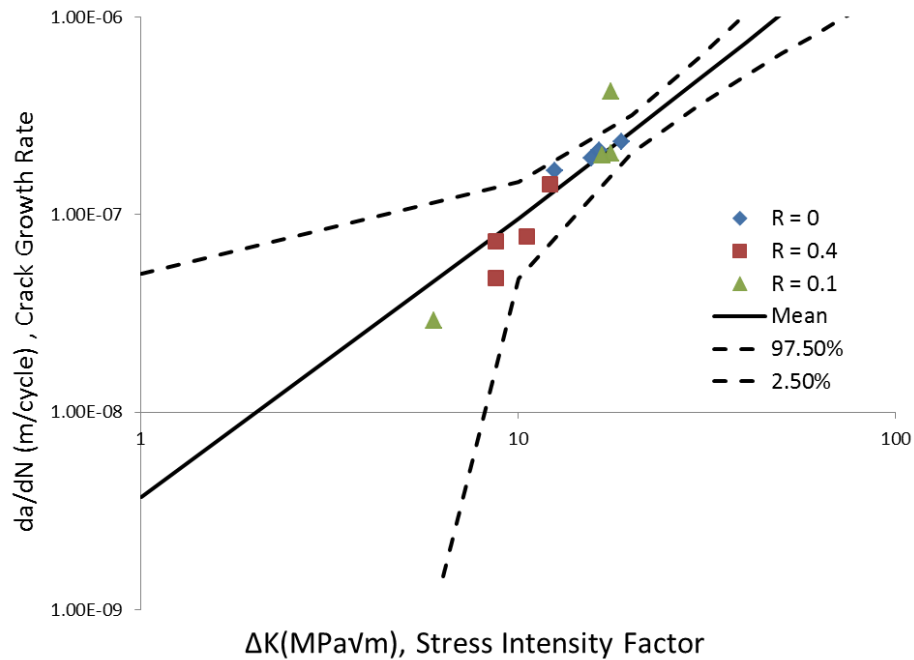
Figure 3.23: Crack growth for different loading ratios

There was no means of measuring crack growth inside the single-hole and edge notch coupons for the range of interest. Crack lengths could only be measured after the sample was removed from the load frame, back cut and then mechanically pulled apart. Therefore, each

data point is an individual experiment, with each test conducted under the same loading condition simply allowed to fatigue for a subjective additional number of cycles. While, not ideal, this has allowed for material batch specific values for A and n, where literature values did not seem to match well with experimentally observed results.

Table 3.4: Walker Equation Parameters

A	7.1E-09
n	1.72
m	0.5 (Levey, 1986, Zhao, 2008)

Thru the use of the modified Walker equation it was observed that the number of cycles estimated between crack initiation and the end of the experiment was only a small percentage of the total cycles undertaken during the experiment. To confirm this, a number of experiments we allowed to run until full fracture. It was observed that number of cycles between full fracture, visual observation of crack initiation and the estimated cycle to initiation was a small percentage of the total cycles undertaken by the coupon, usually on the order of 5-10%.

Additional experiments were run using dog-bone samples. The accuracy of these experiments was increased through use of a microscope. The different dimensions of the dog-bone specimen allowed for the crack size to be measured at the edge of the sample and not down the center, like in the three-hole, single-hole and edge notch coupons. Therefore, thru the aid of the microscope, the number of cycles undertaken to the point of a crack size of 0.25 mm could be observed and the test could continue to full fracture. Similar to the experiments performed with the coupon specimens, the number of cycles between initiation and full fracture was negligible. Therefore, while the capability is available, no distinction will be made between experiments stopped upon the visual observation of a crack and those that were allowed to reach full fracture.
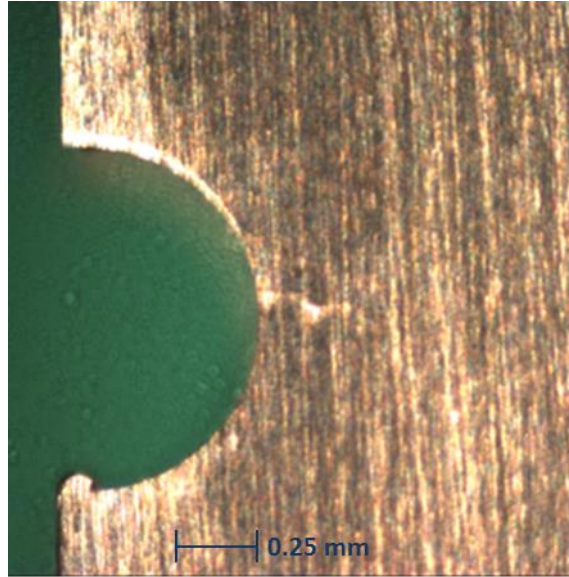
Figure 3.24: Small crack in dog-bone specimen.

The results gathered from the experiments outlined in this chapter were used to develop

models for predicting the cycles to crack initiation. This process is outlined in the following

chapter.

Chapter 4: Results and Discussion

In this chapter, the plastic strain energy density dissipation and thermodynamic entropy generation will be explored as a means of predicting crack initiation. The first property studied will be the plastic strain energy density.

4.1 Plastic Strain energy density

The cumulative plastic strain energy density dissipation for crack initiation of Al 7075-T651 at different load ratios, load amplitudes and tensile mean stresses are presented in Figure 4.1. Results show that plastic strain energy density dissipation increases as the number of cycles to crack initiation increases. At higher load amplitudes (lower number of cycles to crack initiation), accumulation of strain energy density is lower and it increases as the load amplitude decreases. Also, at a given number of cycles the strain energy density dissipation is lower for higher load ratio.
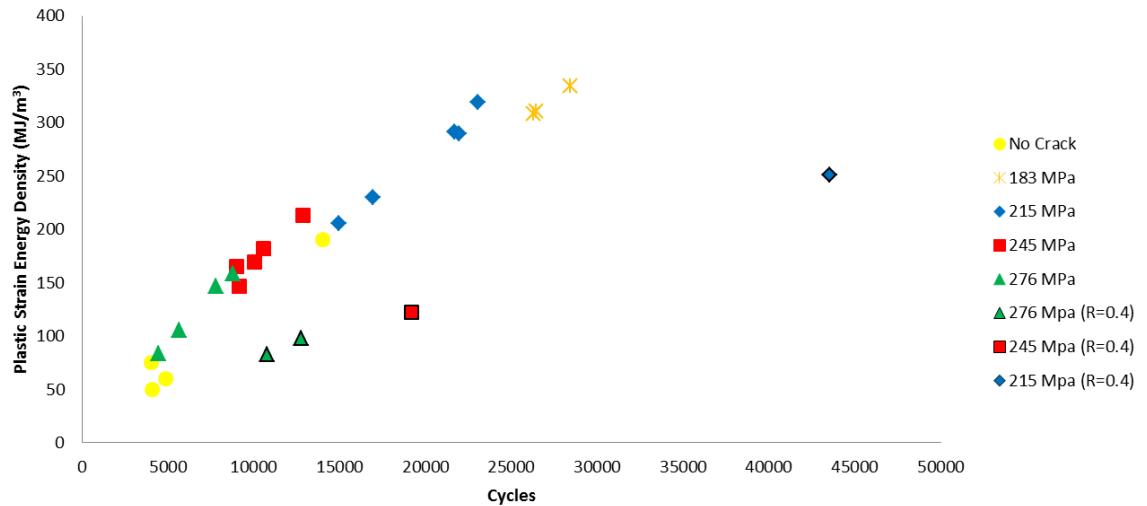
Figure 4.1: Cumulative plastic strain energy density at crack initiation.

In both trends, the strain energy density dissipation depends on the maximum stress and not the minimum stress. This suggests that the maximum stress is the dominant factor for

energy dissipation until crack initiation. Therefore, even with a smaller energy per cycle, the cumulative strain energy density to crack initiation is a constant with respect to a specific maximum load. Based on the observed data, it is hypothesized that accumulation of strain energy density dissipation to crack initiation is independent of load ratio. Examining the fracture surfaces of different specimens shows different number of crack initiation sites for different maximum loads.
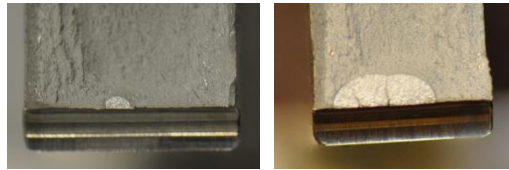
a) 183 MPa peak stress
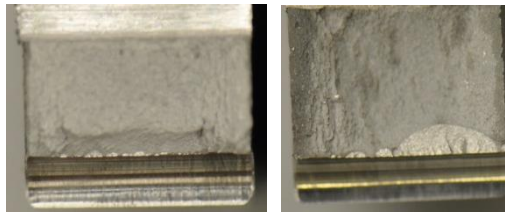
b) 276 MPa peak stress

Figure 4.2: Optical images of fracture surfaces under different fatigue loading conditions.

In Figure 4.2, fracture surfaces for four specimens are shown, two were loaded at 183 MPa and the remaining two were loaded at 276 MPa. Visual observation indicates an apparent difference in the number of crack initiation sites. There are significantly more crack sites initiating at the higher stress. This observation has been explained by Sornette (Sornette, et al., 1992) where LCF rupture typically results from an induced instability in the uniform dislocation distribution as a result of microscopic dislocation interactions within individual grains. In these interactions, dislocations accumulate near surface stress concentrations leading to the formation of persistent slip bands (PSBs) (Abdel-Aziz et. al, 2008). Mesocracks (cracks of grain size) favor nucleating at the PSBs of grain boundaries and thru

interactions with mesocracks in adjacent grains that ultimately emerge at the surface of the specimen in the form of macrocracks.

In the work by Sornette et al. and Magin et al. (Sornette, et al., 1992, Magin, et al., 1989) formation of a macrocrack was described as a function of two important factors: the spacing between PSBs and the fraction of adjacent mesocracks that can effectively connect – the alignment of mesocracks. It was surmised that both of these factors are functions of the plastic strain range, $\Delta\varepsilon_p$.

a)   b)
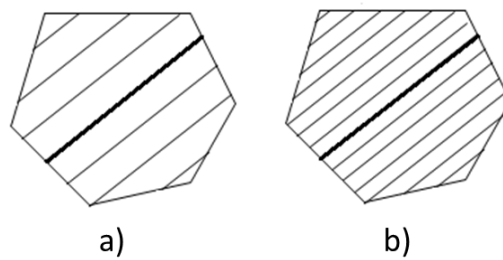
Figure 4.3: Illustration of spacing between PSBs for a) lower plastic strain range and b) larger strain range resulting in higher density of PSBs.

Spacing between PSBs was proposed to be proportional to $1/\Delta\varepsilon_p$ (Winter, 1974). Therefore, at higher plastic strain ranges the density of PSBs is greater (Figure 4.3b). Since mesocracks favor nucleating at PSBs, the rate of nucleation depends on the density of PSBs. However, another factor must be considered for the mesocracks to interact and form a macrocrack.

a)   b)
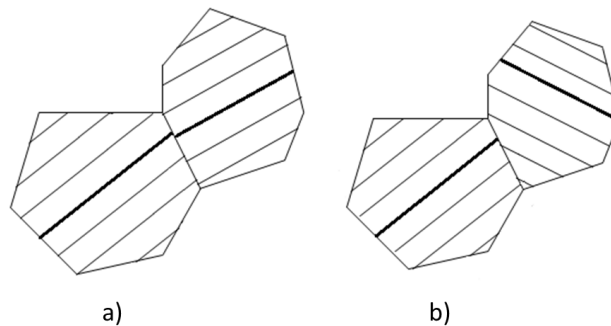
Figure 4.4: a) Illustration of PSB in adjacent grains closely aligned. b) extreme case where grains are not aligned (Sornette et. al., 1992)

The probability, $\mathcal{B}$, that two mesocracks form, at random, in neighboring grains and are aligned within a distance less than some threshold distance needs to be considered. It is unlikely that mesocracks in neighboring grains that are not aligned (Figure 4.4b) cooperate in the formation of a macrocrack (Sornette et al, 1992). This probability was proposed to be equal to the distance, d, from a mesocrack nucleated on a PSB in one grain to that in another grain divided by the spacing between PSBs (Sornette et al, 1992). As a result, $\mathcal{B}$ is proportional to $d\Delta\varepsilon_p$. Therefore, for both criteria, an increase in $\Delta\varepsilon_p$ increases the likelihood of the formation of a crack capable of forming macroscopic cracks. This explains why there are more cracks seen on the fracture surface of the specimens subject to higher loads, with resulting higher plastic strain ranges. It may also explain the increasing trend seen in the strain energy density results discussed below.

Let us first review Morrow's original model for the plastic strain energy density per cycle (Morrow, 1965):

$$\Delta W = 2\sigma_a \Delta\varepsilon_p \left(\frac{1-n'}{1+n'}\right), \tag{4.1}$$

where σ_a is the stress amplitude and n' is the cyclic strain hardening exponent. Using the Coffin-Manson relation, $\Delta\varepsilon_p$ can be written as a function of number of cycles to failure as:

$$\frac{\Delta\varepsilon_p}{2} = \epsilon_f'\left(2N_f\right)^c, \tag{4.2}$$

where ϵ_f' is the fatigue ductility coefficient, c is the fatigue ductility exponent and N_f is the cycles to crack initiation.

Similarly, σ_a can be replaced using fatigue strength properties (Halford, 1961):

$$\sigma_a = \sigma_f'\left(2N_f\right)^b, \tag{4.3}$$

where σ_f' and b are the fatigue strength coefficient and the fatigue strength exponent, respectively.

Substituting Eqs. (4.2) and (4.3) into (4.1) gives:

$$\Delta W = 2\left[\sigma_f'(2N_f)^b\right]\left[2\epsilon_f'(2N_f)^c\right]\left(\tfrac{1-n'}{1+n'}\right), \tag{4.4}$$

which simplifies to:

$$\Delta W = 4\sigma_f'\epsilon_f'(2N_f)^{b+c}\left(\tfrac{1-n'}{1+n'}\right). \tag{4.5}$$

Morrow has shown theoretically that $n' = b/c$ (Morrow, 1965):

$$\Delta W = 4\sigma_f'\epsilon_f'(2N_f)^{b+c}\left(\tfrac{c-b}{c+b}\right). \tag{4.6}$$

Assuming that the strain energy density per cycle given in Eq. (4.6) is constant throughout the fatigue, the final strain energy density can be written as:

$$W_f = \Delta W N_f. \tag{4.7}$$

Substituting Eq. (4.6) into Eq. (4.7) yields:

$$W_f = 4\sigma_f'\epsilon_f'\left(\tfrac{c-b}{c+b}\right)(2N_f)^{1+b+c}. \tag{4.8}$$

It is to be noted that in Eq. (4.8), the final strain energy density, W_f, is independent of cycles to failure, N_f, if the exponent, $1+b+c$ vanishes. That is $b+c =-1$. However, for most materials $b+c$ does not sum to -1. In Table 2.1, fatigue properties for Al 7075-T651 taken from literature are shown. The value of c is more significant in influencing the power term in Eq. (4.8). Now consider, low-cycle fatigue where exponent b is negligible compared to c and that the power term is primarily influenced by c.

Recalling that Morrow used the Coffin-Manson relation to remove $\Delta\varepsilon_p$ from Eq. (4.2), an alternate form of Eq. (4.2) can be expressed as:

$$2N_f = \left(\frac{\Delta\varepsilon_p}{\varepsilon_f'}\right)^{1/c}. \tag{4.9}$$

Thru some manipulation, Eq. (4.9) can be represented in the following form:

$$2N_f \Delta\varepsilon_p^{-(1/c)} = constant. \tag{4.10}$$

In the original formulation presented by Manson (1953) the power term, $-(1/c)$, was given to be about 3 while Coffin found that $-(1/c)$ was approximately equal to 2 (Coffin, 1954). Since the original formulation, the exponent has been found to universally be equal to 2 for most metallic materials (Sornette et al., 1992). Recalling Eq. (4.8), if the exponent in Eq. (4.10) were equal to 1, the cumulative plastic strain energy density would be constant and independent of the cycles to failure. However, it is not, and this is due to the reasons stated by Sornette. Since, the spacing between PSBs is proportional to $1/\Delta\varepsilon_p$ and that the probability, $\mathcal{B}$, is also proportional to $\Delta\varepsilon_p$ requiring a mesocrack density increase by a factor of $1/\Delta\varepsilon_p$ to reach a critical crack size for macroscopic rupture, the cycles to failure is related to the plastic strain range by:

$$N_f \sim \frac{1}{\Delta\varepsilon_p^2}. \tag{4.11}$$

This gives a physical explanation for the common value of 2 that has been found to be nearly universal for the exponent in the Coffin-Manson relation (Sornette et al., 1992). If the exponent was not dependent on these two factors, spacing of PSBs and probability of adjacent interacting mesocracks, the exponent would be 1 and the result would be a constant cumulative energy at failure. Equation (4.11) also shows a decrease in the number of cycles to failure as the plastic strain range increases. The lower fatigue life results in less time for energy to accumulate.

4.2 Effect of FLE and gap-filling

Given the previous explanation, the trend observed in Figure 4.1 matches well with the historical trend (See Figure 2.1) observed by Halford (1964), but it does not match with the results that served as the genesis for this research. Recalling Figure 1.2, the plastic strain energy density for 40 different P3 aircraft at 100% FLE was nearly constant with limited scatter around a single value. The explanation for the difference lies in the determination of 100% FLE as described in Chapter 2. Recalling FLE is a cumulative damage index calibrated by a representative fatigue test, while 100% FLE is scaled to represent a crack size of 0.254 mm, it is based off a single experiment. It would be similar to running a single experiment on a coupon used in this study under a load of 245 MPa and using the plastic strain energy density results as the index of energy required for all crack initiation, regardless of the loading. From the results presented in Figure 4.1 it can be clearly seen that would be an incorrect judgment. But, that does not seem to be a fair argument; the data in Figure 1.2 is from 40 different aircraft, with different and random loadings. How then, was the energy all the same at crack initiation? A possible explanation for this is that the strain energy density wasn't the same at crack initiation, but it was all the same at the damage index, 100% FLE, calibrated to crack initiation (0.254 mm crack size) from a single FSFT. Each 'test' was stopped at the same damage index, nearly the same point in time, and as a result the energies for each of the 40 aircraft were very similar.

However, that explanation doesn't account for the randomness of the different aircraft flights. But, how different were they? Each aircraft took off, conducted normal flight operations and eventually landed. This means that while each plane saw different flight profiles, they were all likely flown the same way. As a result, the loads each aircraft sees are likely similar. Additionally, data is not always taken reliably for each aircraft individually. When data is not available or invalid a process called 'gap-filling' is used to account for missing data (Iyyer

and Phan, 2003). Gap-filling consists of replacing sections of missing or invalid data with an approximate usage value representative of the damage expected based off of a representation, using load spectrum data (Iyyer and Phan, 2003). The amount of gap-filling that takes place can be a considerable portion of the aircrafts life (Iyyer and Phan, 2003). For the forty aircraft using to develop Figure 1.2, approximately 40% of the total life for each aircraft was a result of gap-filling (Rusk, 2013). If 40% of each aircraft is based off the same representative data it would be expected to have a considerable effect on the scatter seen in the results.

4.3 Total strain energy density

The cumulative total strain energy density dissipation for crack initiation of Al 7075-T651 at different load ratios, load amplitudes and tensile mean stresses are presented in Figure 4.5. Results show that, similar to the plastic strain energy density, the total strain energy density dissipation increases as the number of cycles to crack initiation increases. At higher load amplitudes (lower number of cycles to crack initiation), accumulation of strain energy density is lower and it increases as the load amplitude decreases.
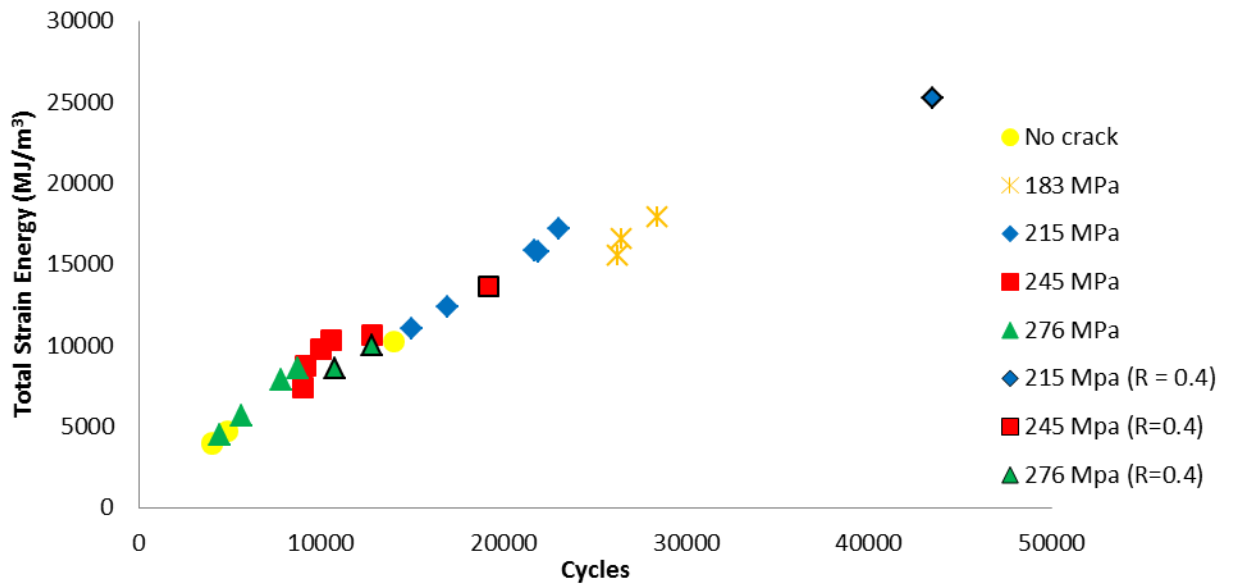
Figure 4.5: Cumulative total strain energy density at crack initiation.

Unlike in the plastic strain energy density, there is only one trend. This is because the way the total energy is calculated. Recalling Figure 3.11, including to elastic strain energy density, the total strain energy density is estimated by taking the entire area under the top of the hysteresis loop (See Figure 3.11a). For a sample tested at 245 MPa, R = 0.4, its hysteresis loop was significantly smaller than the hysteresis loop for the same load with a lower R-value of 0.1. Now that a significant area is no longer excluded (See Figure 3.11b), the cumulative energies for the load ratio 0.4 are larger than those belonging to the same peak load with smaller R-values. While the plastic strain energy density was grouped by peak load, the total strain energy density does not show the same trend.

The results presented in Figure 4.1 show that for notched specimens, under load ratios greater than zero, the plastic strain energy density dissipation at the point of crack initiation is dependent on the maximum stress, follows an increasing trend and is independent of loading ratio. This limited variation in strain energy density throughout the experiment may provide a means of easily predicting the state of the material with respect to crack initiation.
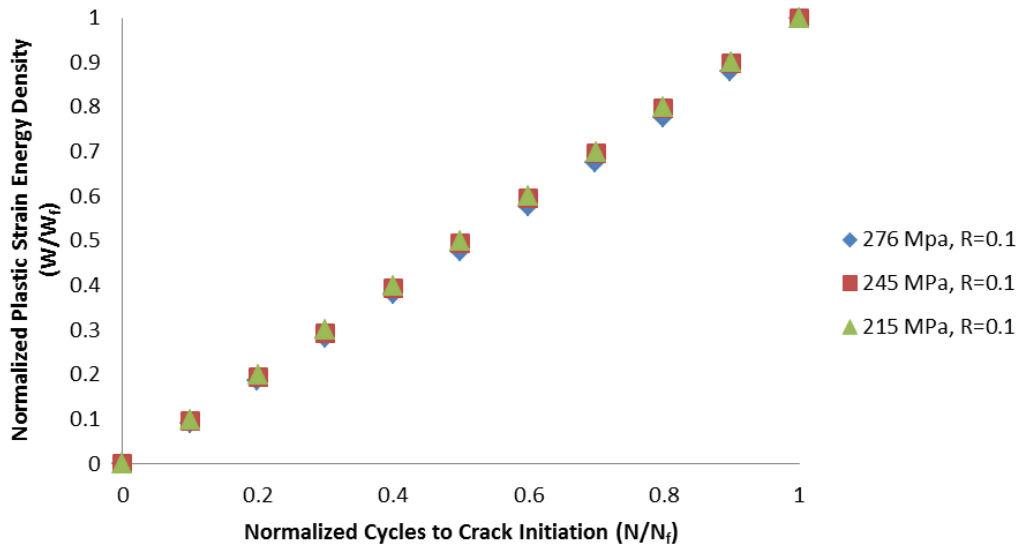
Figure 4.6: Normalized plastic strain energy density dissipation vs. normalized cycles to crack initiation

In Figure 4.6, the normalized plastic strain energy density dissipation for specimens tested under a load ratio of 0.1 at 215 MPa, 245, MPa, and 276 MPa are presented. The relation observed in Figure 4.6 can be expressed as:

$$\frac{W}{W_f} \cong \frac{N}{N_f},$$ (4.12)

where W_f is the plastic strain energy density dissipation at crack initiation for a particular set of loading conditions. This relation is the same as observed in the earlier entropy study on fatigue by Naderi et al. (2010) and the resulting methodology for predicting failure, or crack initiation in this study, still holds. Using Eq. (4.12) the cycles to failure can be expressed as:

$$N_f \cong \left(\frac{N}{W}\right) W_f.$$ (4.13)

Therefore, for a known W_f, after an estimation of the entropy generation W at a cycle N, the fatigue life can be estimated. Since the plastic strain energy density dissipation per cycle does not vary considerably during an experiment, the estimation of cycles remaining to failure can be made at any time during the experiment.

4.4 Plastic strain energy density model development

4.4.1 Deterministic model development

This first step in producing usable results from this data is to determine a model that can appropriately capture not only the trend seen in the energy, but also the difference in results for the change in loading ratios. Experimental data has been split into four different groupings: two groups for probabilistic model development, a group for determination of the model bias and uncertainty and a final group to check that the model is capable of capturing estimates made outside of data used in its development.

In Figure 4.7, the same data presented in Figure 4.1 is presented with the energy as the independent variable such that the model developed can be used to predict the cycles to crack initiation.
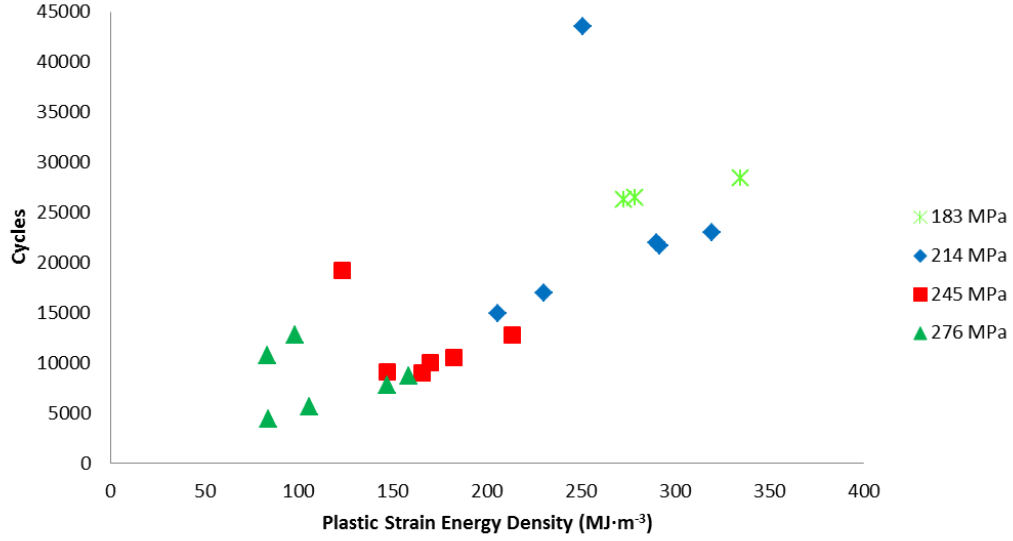
Figure 4.7: Cumulative plastic strain energy density at crack initiation, energy dependent.

Experimental data used in the initial deterministic, model development is presented in table 4.1.

The model chosen to capture the data is of an exponential form:

$$N = ae^{bW}, \tag{4.14}$$

where *a* and *b* are parameters that fit the model. The exponential form was found to best fit the available evidence. The ability to model the experimental results while capturing the difference in changes between different load ratios will be done by having different sub-models for parameters *a* and *b*. The sub-model for parameter *a* is chosen to be a parabolic model:

$$a = a'R^2 + b'R + c'. \tag{4.15}$$

The sub-model for parameter b is a linear model:

$$b = d'R + e', \tag{4.16}$$

where *a'*, *b'*, *c'*, *d'* and *e'* are parameters fit using experimental data. Originally, the sub-models for both *a* and *b* were proposed as linear. However, the difference between the

loading ratios of 0 and 0.1 is not spaced with the same difference as the loading ratios

between 0.3 and 0.4, as will be shown later in this chapter. The parabolic model best fit the

change in trends seen in the experiments between different load ratios. A linear form was

found to appropriately capture the trend needed for the sub-model of *b*.

Table 4.1: Data for deterministic model development.

R	W (MJ·m^{-3})	Max Stress (MPa)	Cycles
0	154.29	215	10391
0.1	272.21	183	26259
0.1	230.21	215	16935
0.1	291.36	215	21701
0.1	213.20	245	12824
0.1	146.67	245	9121
0.1	146.49	276	7786
0.1	105.56	276	5609
0.4	83.028	276	10734
0.4	122.59	245	19188

It will be shown later that the results of the model are better presented as done in

Figure 4.1, with the cycles being the independent variable. Modifying Eq. (4.14), the equation

for the energy given a cycle becomes:

$$W = \frac{ln(N) - ln(a'R^2 + b'R + c')}{d'R + e'} \tag{4.17}$$

The entire form of Eq. (4.17) is fit using the data presented in the Table 4.1. The

initial model fit was done using simple regression minimizing the differences between the

model prediction of the cycles to failure and those observed in the experiments. In this

approach, each parameter was given a value and the resulting model predictions were

compared with the experimental results presented in Table 4.1. The difference between these

two values was reduced by changing the different model parameters using the Solver function

in Microsoft Excel. The results are presented in Figure 4.8.
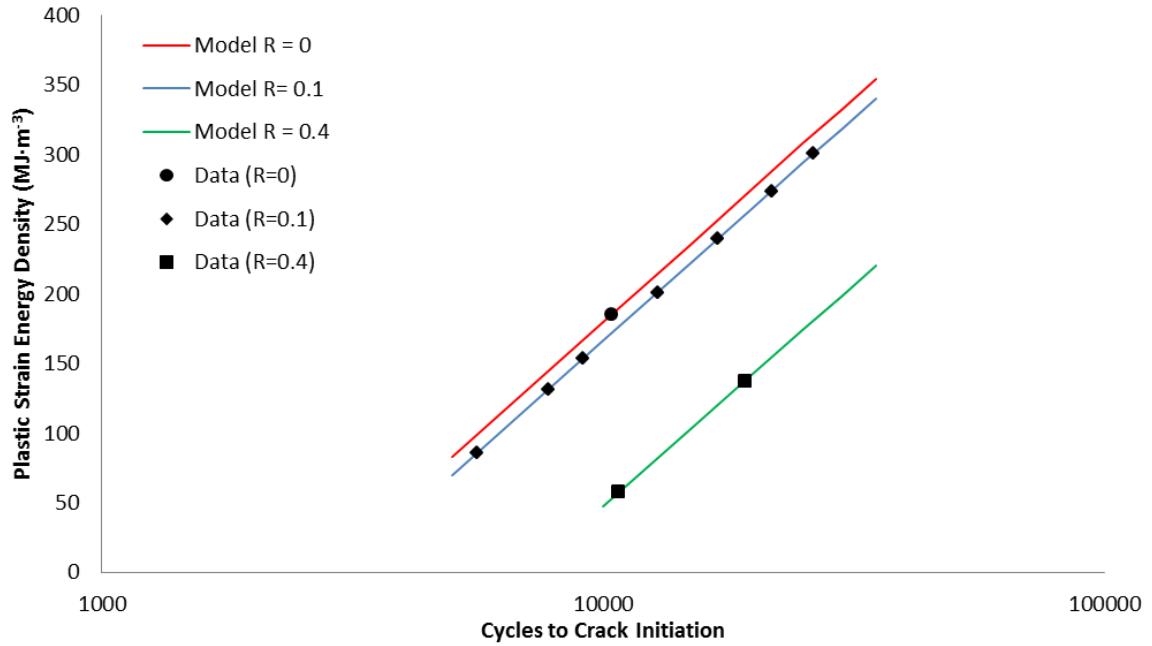
Figure 4.8: Plastic strain energy density deterministic model.

The fitted forms of Eqs. (4.15) and (4.16) are

$$a = 27056.89R^2 + 0 \cdot R + 2756.136, \tag{4.18}$$

and

$$b = 0.0002R + 0.007168. \tag{4.19}$$

The model will now be checked against additional, independent data to determine the validity of the model.

4.4.2 Model validation

In this section experimental results independent from those used to develop the model will be used to validate the model and make an estimation of the true value.

4.4.2.1 Model validation – addition loading conditions

The first test will be a subjective, qualitative assessment. In Figure 4.9, the models for two experiments with loading ratios of 0.2 and 0.3 are shown. The data shown in Figure 4.9 are those of experiments run independent of the model development. The resulting

64

models for the load ratios of 0.2 and 0.3 suggest that the model does an acceptable job predicting the outcome at different loading ratios. Once again observed in Figure 4.9 is the distinction that the energy at crack initiation is dependent on the peak stress and not the cycles to failure as the data was developed using experiments run with a peak stress of 245 MPa.
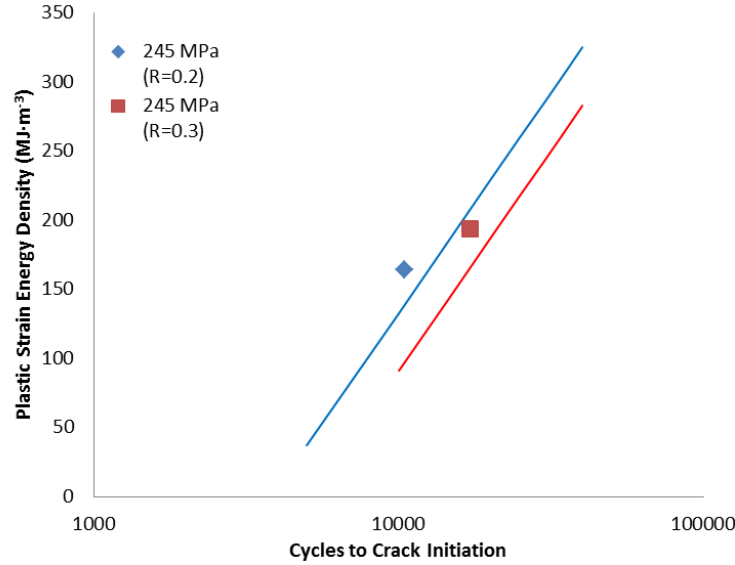
Figure 4.9: Comparison of predicted model and experimental results using plastic strain energy density.

4.4.2.2 Model validation – bias and uncertainty

A Bayesian inference will be used to determine the model bias and uncertainty with respect to the true value. The Bayesian inference is a technique used to update a given 'state of knowledge.' In the Bayesian inference a subjective prior probability distribution (pdf) of parameters $f_0(\theta)$ is combined with observed data (evidence) in the form of a likelihood function of an unknown parameter θ. The result is an updated state of knowledge identified as the posterior distribution, $f(\theta|Data)$. This process is shown mathematically in Eq. (4.20) and pictorially in Figure 4.10.

$$f(\theta|Data) = \frac{f_0(\theta)L(Data|\theta)}{\int_\theta f_0(\theta)L(Data|\theta)}.$$

(4.20)

65
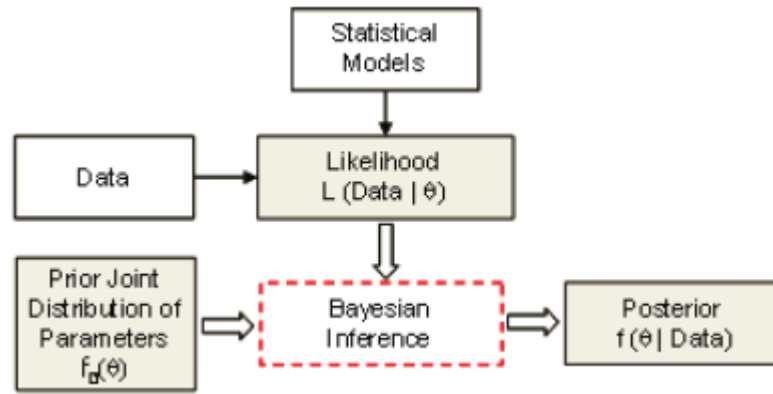
Figure 4.10: Bayesian inference framework. (Azarkhail & Modarres, 2007)

In this research, the Bayesian inference is solved using the program WinBUGS (MRC). The program has been used in previous parameter estimation research (Azarkhail & Modarres, 2007) and output updating analysis (Ontiveros, 2010, Azarkhail et al., 2009, Pourgol-Mohamad, 2007). For more information on WinBUGS see Cowles (2004). The next validation step was to perform a more complex assessment of the models bias and uncertainty. This is done using a method originally developed at the University of Maryland (Azarkhail et al., 2009, Ontiveros, et al., 2010) to account for uncertainties in fire model simulation predictions.
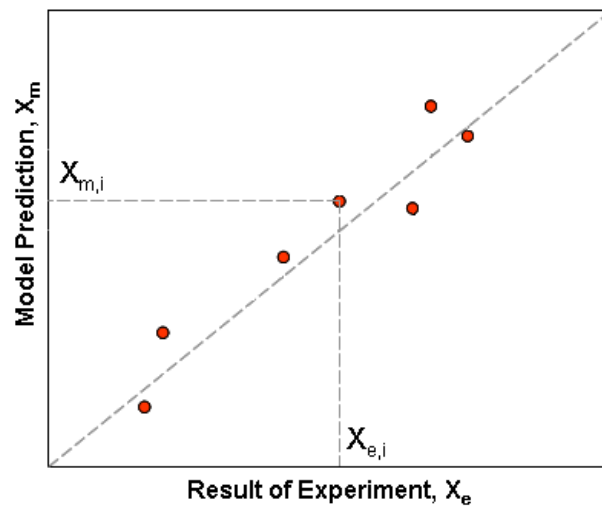
Figure 4.11: Deterministic model comparison to experimental measurement. (Azarkhail et al., 2009)

Figure 4.11 shows a representative illustration of a comparison between model predictions and experimental results. If the model predictions and the experimental results matched perfectly, each point would fall on the dotted, 'perfect match line.' The two values do not match perfectly because of uncertainties in both the model predictions and the experimental measurements.

In this approach, both the model prediction and experimental result are considered to be estimations of physical reality of interest, given some error as shown in Equations 4.21 and 4.22.

$$\frac{X_i}{X_{e,i}} = F_{e,i} \quad ; \quad F_e \sim LN(b_e, s_e) \tag{4.21}$$

$$\frac{X_i}{X_{m,i}} = F_{m,i} \quad ; \quad F_m \sim LN(b_m, s_m) \tag{4.22}$$

where X_i is reality, $X_{e,i}$ is the experimental result, $X_{m,i}$ is the model prediction, F_e is the multiplicative error of experiment with respect to reality, and F_m is the multiplicative error of the model prediction, with respect to reality, b_e is the mean of error of experiment to the real value, s_e is the standard deviation of the error of experiment to the real value, b_m is the mean of error of model to the real value, and s_m is the standard deviation of the error of model to the real value. In this formulation the standard deviation of both multiplicative errors are assumed to have constant standard deviations. With not observed differences in the dispersion between model predictions and experimental results at higher and lower values, this was assumed to be acceptable.

Combining Eqs. (4.21) and (4.22), the result is:

$$F_{e,i} X_{e,i} = F_{m,i} X_{m,i}$$
$$\frac{X_{e,i}}{X_{m,i}} = \frac{F_{m,i}}{F_{e,i}} = F_{t,i}$$

Assuming Independency of F_m, F_e then,

$$F_t \sim LN\left(b_m - b_e, \sqrt{s_m^2 + s_e^2}\right), \tag{4.23}$$

where F_t is the multiplicative error of experiment with respect to the model prediction. The likelihood to be used is:

$$L(X_{e,i} / X_{m,i}, b_e, s_e \mid b_m, s_m) =$$

$$\prod_{i=1}^{n} \frac{1}{\sqrt{2\pi}\left(\dfrac{X_{e,i}}{X_{m,i}}\right)\sqrt{s_m^2 + s_e^2}} e^{-\frac{1}{2} \times \frac{\left[\ln\left(\frac{X_{e,i}}{X_{m,i}}\right) - (b_m - b_e)\right]^2}{s_m^2 + s_e^2}} \tag{4.24}$$

The data used in this step of the analysis must be data independent of the data used in the model development step. The data used in this step is presented below in Table 4.2. The WinBUGS used for this analysis is presented in Appendix 2.

As outlined in the approach described by Ontiveros et al (2010), an estimation of the experimental uncertainty must be made. The plastic strain energy density is taken from the hysteresis loops taken during the experiments. Therefore, the uncertainty on the load applied and recorded by the test frame and the strain measurements made by the extensometer must be made. The load cell on the test frame was calibrated in 2012 (Instron, 2012) and found to be accurate to within ±1%. The extensometer used is stated to be accurate to within ±10% (Epsilon Tech Corp., 2013) for the strain ranges observed in these experiments.

The experimental uncertainties to be used are determined using the relative expanded uncertainties resulting from measurements, $\tilde{U}_E$, as described by NUREG-1824 (Hamins and McGrattan, 2006). The experimental uncertainty used is determined by:

$$U_{c,E} = \frac{1}{\sum_{i=1}^{m} n_i} \sum_{i=1}^{m} \tilde{U}_E n_i \tag{4.25}$$

where m is the number of test series and n_i is the number of tests in a respective test series. $U_{c,E}$ is the experimental uncertainty to be used in the output updating step for estimating the model uncertainty. As all the results used in this analysis came from

the same test series, the calculation using Eq. (4.25) reduces to simply the estimation

of $\tilde{U}_E$. Combining the uncertainties for the strain gauge and the load cell, the

experimental uncertainty to be used with the strain energy density is found to be

$\pm 10.04\%$.

Table 4.2: Data used for determination of model bias and uncertainty.

R	Max Stress (MPa)	Cycles	Experimental W (MJ·m⁻³)	Model W (MJ·m⁻³)
0	276	5754	105.1	102.7
0.1	183	26437	278.6	301.5
0.1	183	28409	334.3	311.5
0.1	215	23031	319.0	282.3
0.1	215	21940	289.7	275.6
0.1	215	14931	205.5	222.0
0.1	245	10004	169.3	166.3
0.1	245	10534	182.3	173.5
0.1	245	9002	165.3	151.6
0.1	276	8748	158.4	147.7
0.1	276	4438	83.5	53.2
0.4	215	43533	250.5	250.5
0.4	276	12757	97.9	81.1

The summary statistics used to determine the model bias and uncertainty for the deterministic

model, Eq. 4.17, are shown in Table 4.3

The model uncertainty bounds can be determined from the percentiles of F_m. The

resulting upper bound is 44.9%, while the lower bound is -20.8%. This is shown graphically

in Figure 4.14. Given the value of F_m, it appears the model is slightly bias and underestimates

the true energy at crack initiation. The bias can be understood graphically in Figure 4.12 by

comparing the True Mean with the Perfect Match Line, which represents unbiased model

predictions and experimental measurements.
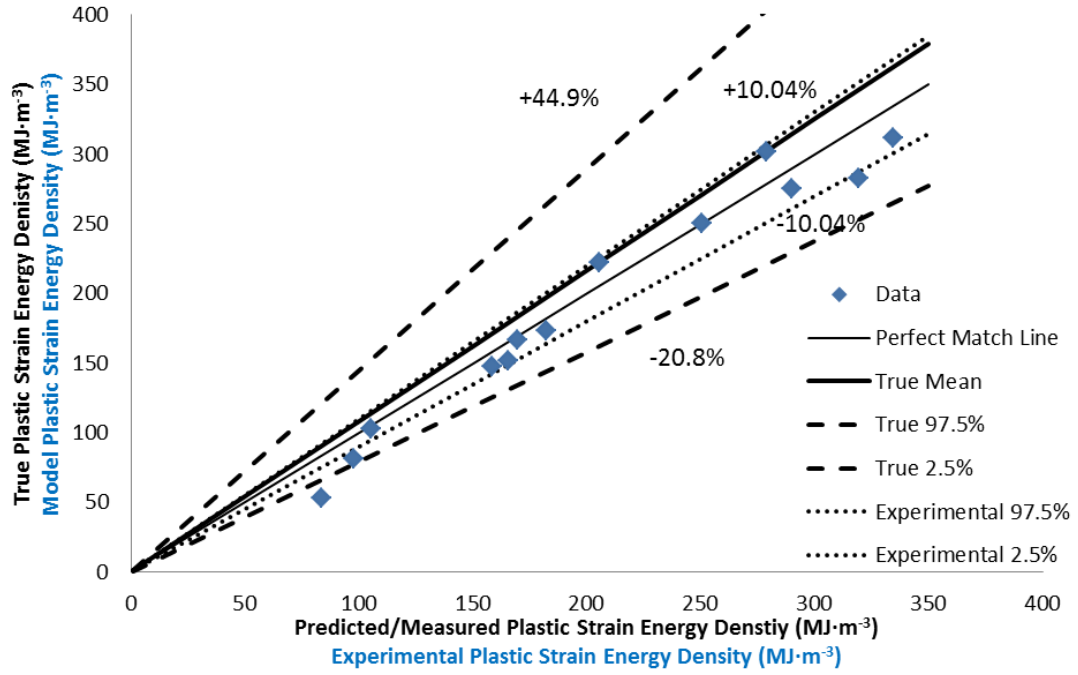
Figure 4.12: True value distribution of cycles given a deterministic model prediction using plastic strain energy density

Table 4.3: Summary statistics for model bias and uncertainty.

Parameter	Mean	STDEV	2.50%	97.50%
b_m	0.069	0.043	-0.015	0.155
s_m	0.139	0.0383	0.0828	0.231
F_m	1.083	0.166	0.792	1.449

A note that must be made is when this approach for model uncertainty (Ontiveros et al., 2010) is used. The bounds presented in Figure 4.12 are that of the true cycles to crack initiation given a model prediction. Studying the values presented in Figure 4.12, it appears that the upper and lower bounds do not match, the bounds appear to just barely encompass the data, and are certainty not centered on the data points. This is in contradiction to the often-observed use of a confidence interval. These bounds represent the confidence of the model prediction for the true cycles to crack initiation. As seen in Figure 4.12, the bounds are seen to be slightly below the matched data indicating that the model predictions are

70

consistently, if only slightly with an $F_m = 1.08$, under predicting the energy at crack initiation. This is because the true cycles to crack initiation could be, with a 95% confidence, as much as 44.9% greater than, or 20.8% lower than the model prediction.

With a determination of F_m, an estimation of true value and its distribution can be determined given model predictions. For a deterministic model, the estimation of the true value is (Azarkhail et al., 2009):

$$X \sim LN(\ln(X_m) + b_m, s_m). \tag{4.26}$$

In Figure 4.13, the true value distribution of plastic strain energy density at crack initiation, given a model prediction is presented. These distributions allow for an estimation of the energy at a given cycle for the loading ratios of 0.1 and 0.4. The decreasing bounds at the lower cycles are an artifact of the use of the multiplicative error used in the estimation of the bias and uncertainty. Also, in the model bias and uncertainty estimation, the distribution of F_m was assumed to be lognormal. In Figure 4.13, the true value distribution for the different load ratios has been converted to a normal distribution. In the next section, the distribution of the true value given a model prediction will be used to determine probability of crack initiation and having a normally distributed model will allow for less complex computation to be required.
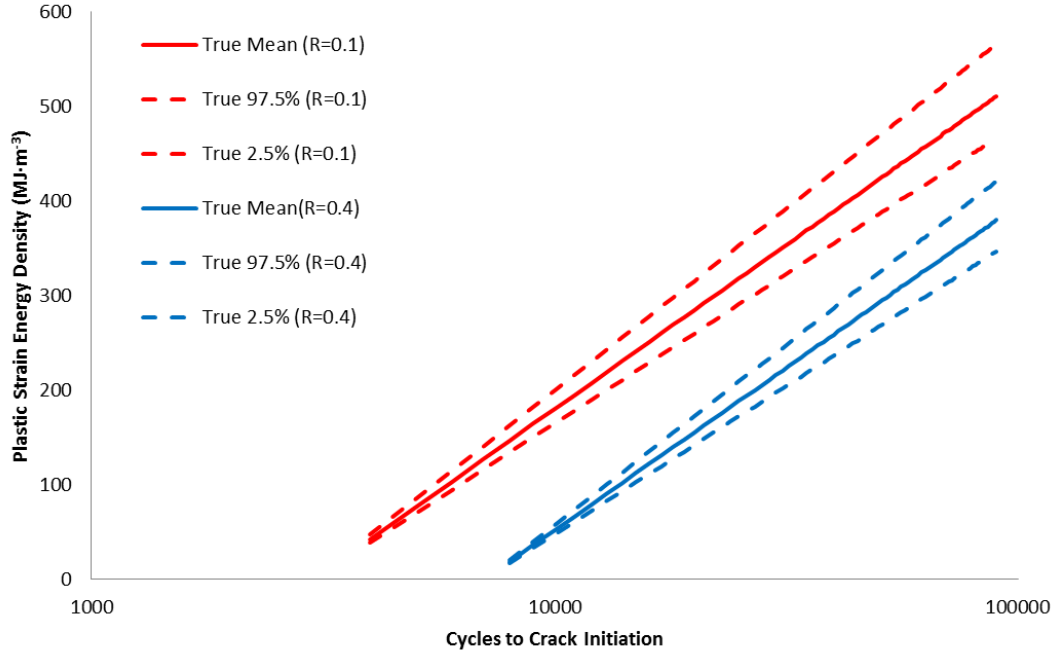
Figure 4.13: True value distribution for 0.1 and 0.4 load ratios using plastic strain energy density.

Recalling the values presented for the loading ratios of 0.2 and 0.3, the value of F_m will be used to correct the model to estimate the true value and compare the results. In Figure 4.14, the results for two experiments with a peak load of 245 MPa and at load ratios of 0.2 and 0.3 are shown. No data of load ratios 0.2 and 0.3 was used in the development of the model. The models appeared to slightly under predict the values. An F_m value of 1.08 confirms the fact that the model was slightly under predicting the true value. The data presented in Figure 4.14 is not the true value, given that experimental values can be uncertain (See Eq. 4.24), but the correction to the model by the application of the multiplicative error of the model prediction, F_m, does appear to increase the accuracy the models predictions.
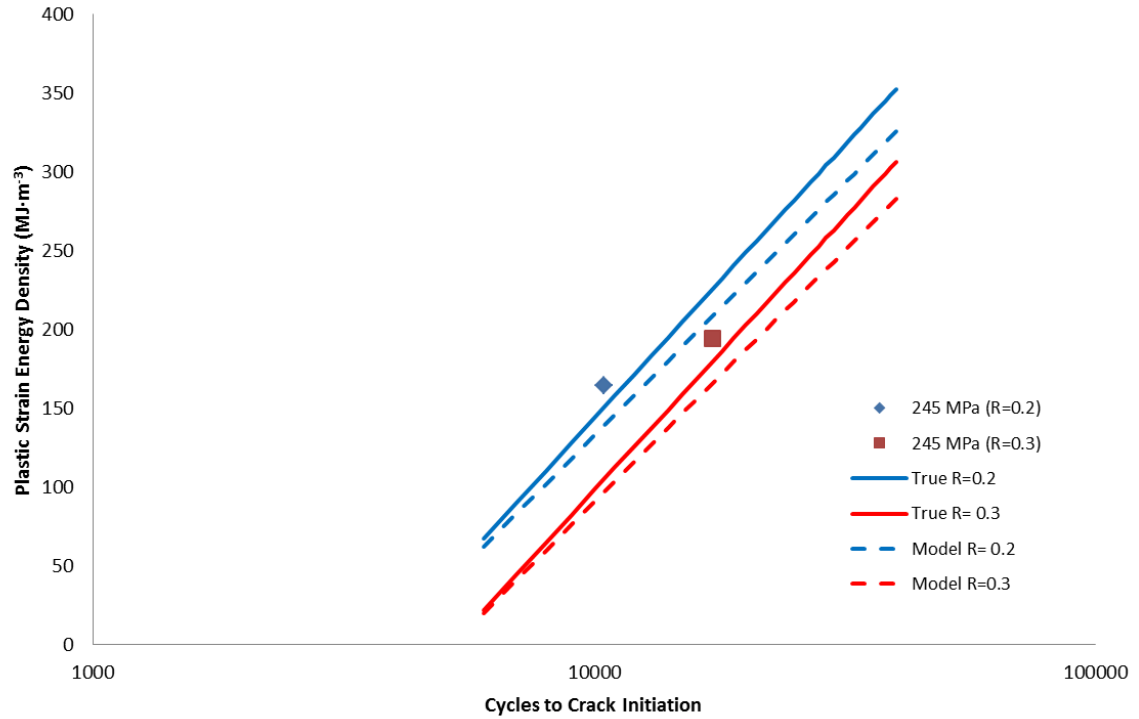
Figure 4.14: Comparison of model prediction and mean true value estimation using plastic strain energy density.

4.4.6 Probability of crack initiation

4.4.6.1 Distributive energy limits

Given the developed model and an understanding of the bias and uncertainty of its predictions, it can be used to determine the cycles to crack initiation. In order to use the plastic strain energy density as a means of predicting fatigue life, a value of energy needs to be picked as the point of crack initiation. As shown in Figure 4.1, the energy at crack initiation is not constant and appears to be a function of the peak stress, regardless of the load ratio. As mentioned in Chapter 3, the difference in cycles between a crack length of 0.254 mm, the Navy's approximation of crack initiation, and complete fracture of the specimen was negligible. In Figure 4.15 the energies presented in Figure 4.1 are plotted at against the crack lengths measured at the conclusion of their respective experiments. In Figure 4.15 the energies are grouped not by crack lengths, but by the peak stress. The groupings become

73

more pronounced when considering the experiments concluded before the initiation of a measurable crack. While not color coded as such, in Figure 4.15 the data point with the greatest energy for the 'No crack' grouping is the result of an experiment run at 215 MPa with a load ratio of 0.1. It appears that this data point is approaching the grouping of the other 215 MPa experiments. These results also supplement the observation seen in Figure 4.1 that the groupings appear to be independent of load ratio.
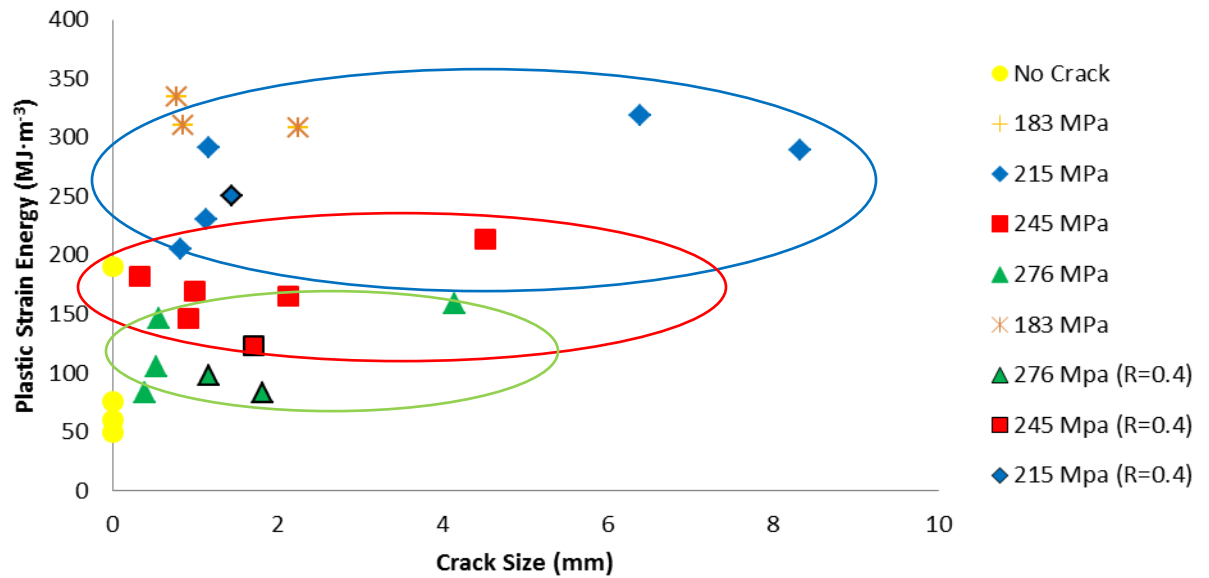
Figure 4.15: Plastic strain energy density vs. crack length.

As mentioned earlier in Chapter 3, a number of experiments were conducted on dog-bone specimens. In these experiments both the cycles at crack initiation and full fracture could be observed and a comparison between the energies could be made. The results for three experiments at different peak stresses and their respective energies at crack initiation and full fracture are shown in Figure 4.16. Figure 4.16 shows the difference in energy between crack initiation and full fracture is nearly negligible.
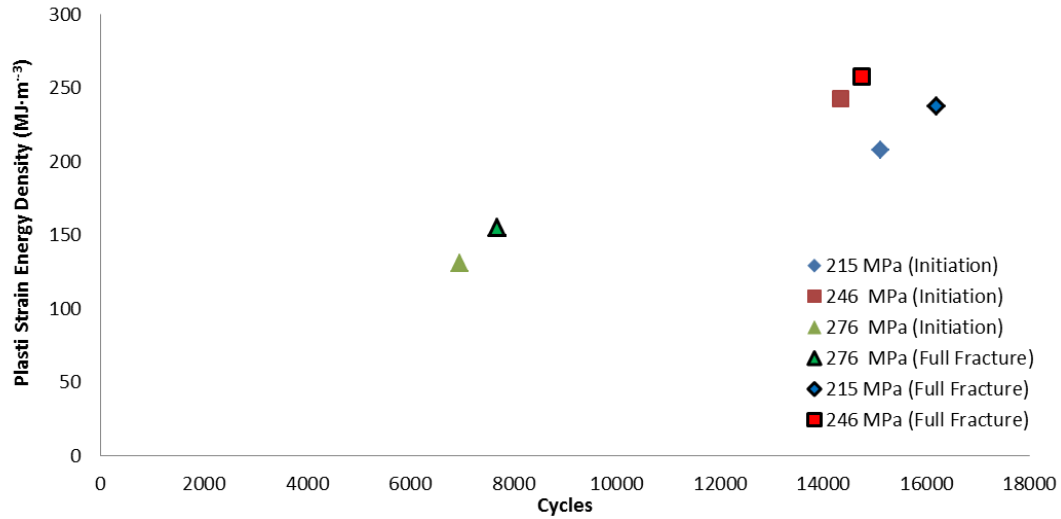
Figure 4.16: Dog-bone specimen plastic strain energy density and crack initiation and full fracture

From the evidence above, it does not appear that a constant value of energy can be used for the determination of crack initiation, but that a distribution of energy, which changes depending on the peak stress, would have a more reliable use. In fact, the energy groupings in Figure 4.15 are reminiscent of the plastic strain energies for the 40 aircraft that served as the genesis of this research (See Figure 1.1). Except, now instead of a single energy limit for crack initiation, this evidence suggests that there is no single limit of plastic strain energy density at crack initiation, but different groupings, dependent on the peak stress.

In Figure 4.17 the energy groupings pointed out in Figure 4.15 are taken and assumed to be distributions of plastic strain energy density at crack initiation for the different peak stresses. For simplicity, the energies are assumed to be normally distributed. The means and standard deviations for each energy grouping are shown in Table 4.4.

Table 4.4: Crack initiation distributions for different peak stresses.

Stress (MPa)	183	215	245	276
Mean	295.02	267.15	175.37	123.48
STDEV	34.13	47.32	24.71	34.94

75
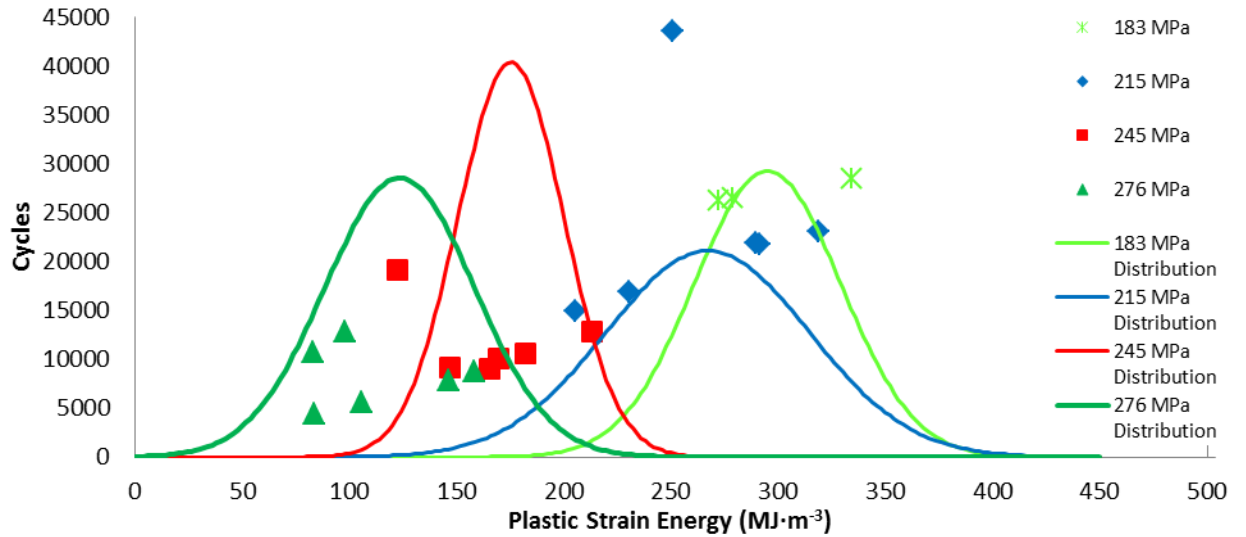
Figure 4.17: Plastic strain energy density distributions of energy to crack initiation.

In Figure 4.17, again it is clear that the cumulative plastic strain energy density at crack initiation is a function of the peak load, similar to what was depicted in Figure 4.15. The results shown in Figures 4.15 and 4.17 are grouped by peak stress even though the two loading ratios result in differing number of cycles to failure. Using the developed probabilistic model, the probability of exceeding a deterministic energy value would be a simple calculation. However, since the target is no longer a single value, but its own distribution, the solution will require a different approach.

4.4.6.2 Prediction of crack initiation

In order to appropriately model a distributive model prediction as it approaches a distributive target, the interactions of these distributions must be considered. As stated in the previous section, the limits of energy for each loading condition are assumed to be normally distributed in order to simplify calculations. With additional data, it is possible that this assumption could be verified or other distributions could be used. Additionally, the model is now presented with a normally distributed error. This relation is presented in Figure 4.18.
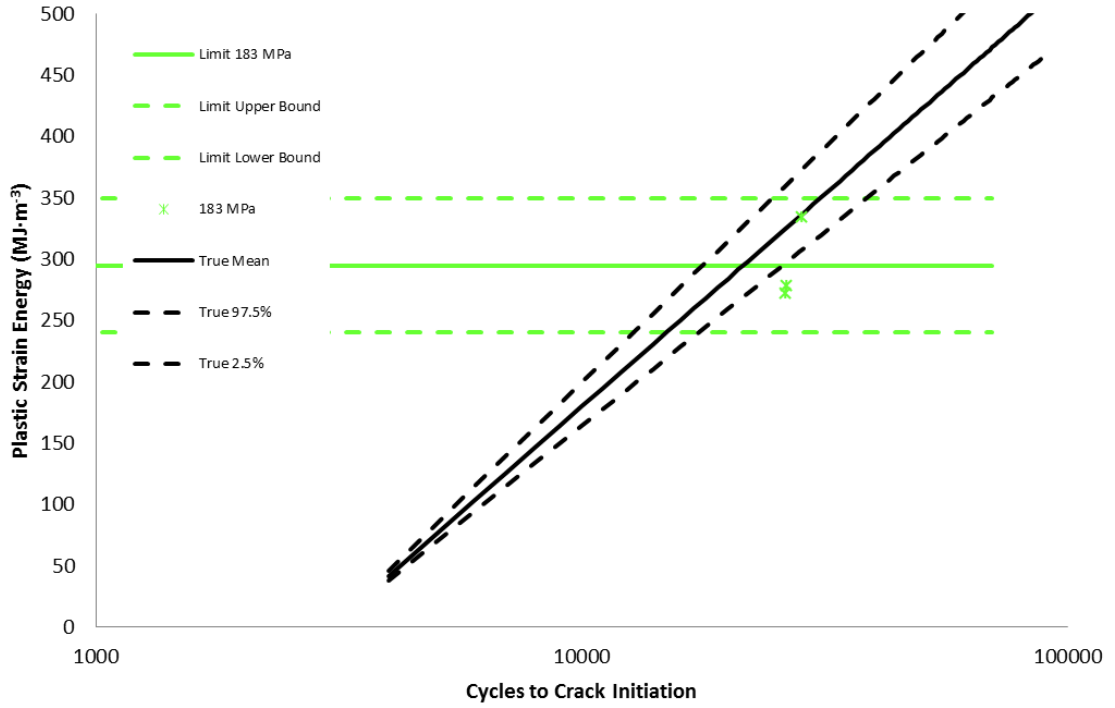
Figure 4.18: True probabilistic value approaching probabilistic limit using plastic strain energy density.

The goal is to determine the interaction between the two distributions, the model distribution as it approaches the limit distribution for a certain peak loading condition. The interaction can be solved as it is similar to the stress-strength interference model (Dai and Wang, 1992). When both the 'stress' and 'strength' are normally distributed, the cumulative distribution function for the interaction of the two distributions can be written as:

$$\Phi\left(\frac{\mu_1-\mu_2}{\sqrt{\sigma_1^2+\sigma_2^2}}\right), \tag{4.27}$$

where, μ_1 is the mean of the model at different cycles, μ_2 is the mean of the limit for a particular peak stress, σ_1^2 is the variance of the model at a particular cycle and σ_2^2 is the variance of the limit for a particular peak stress. The interaction of the two distributions can be used to determine the probability of crack initiation at particular cycles.

As an example, the result for the 183 MPa limit is shown in Figure 4.19. Here, the probability of a crack initiating is 100% after 40,000 cycles. This was expected as there were that no experiments for a loading ratio of 0.1 reached 40,000 cycles. When plotted against the model and limit distributions (Figure 4.20), the results again appear to match the expected outcome.

.
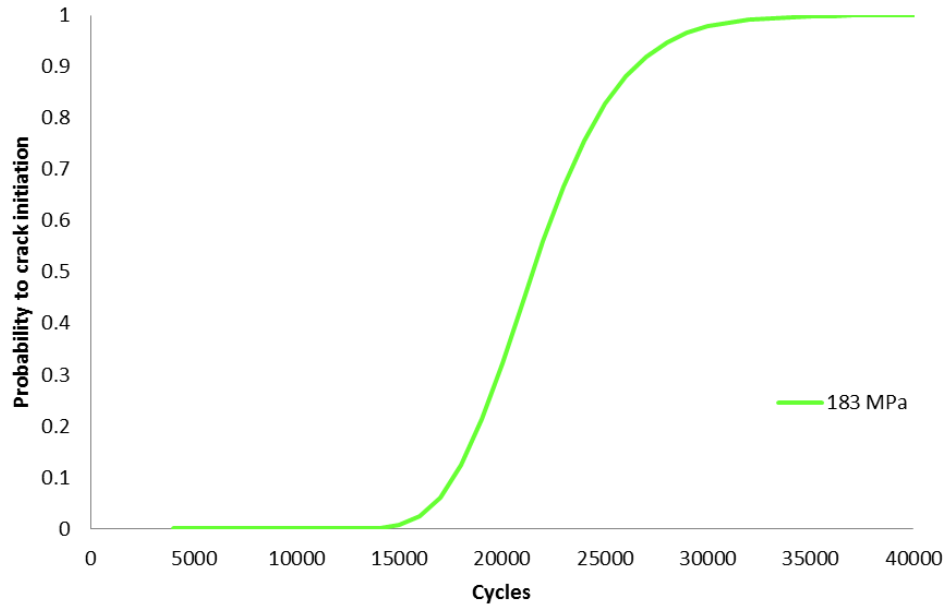
Figure 4.19 Probability of crack initiation using plastic strain energy density.

In Figure 4.20 the probability of crack initiation is plotted with the model and limit distributions. A quick glance shows how the probability starts to increase once the two distributions start to interact. Additionally, the probability of a crack initiating is around 50% when the two models overlap, which from the discussion above, is more reasonable that a probability of 100% when using the area of interaction between the two distributions
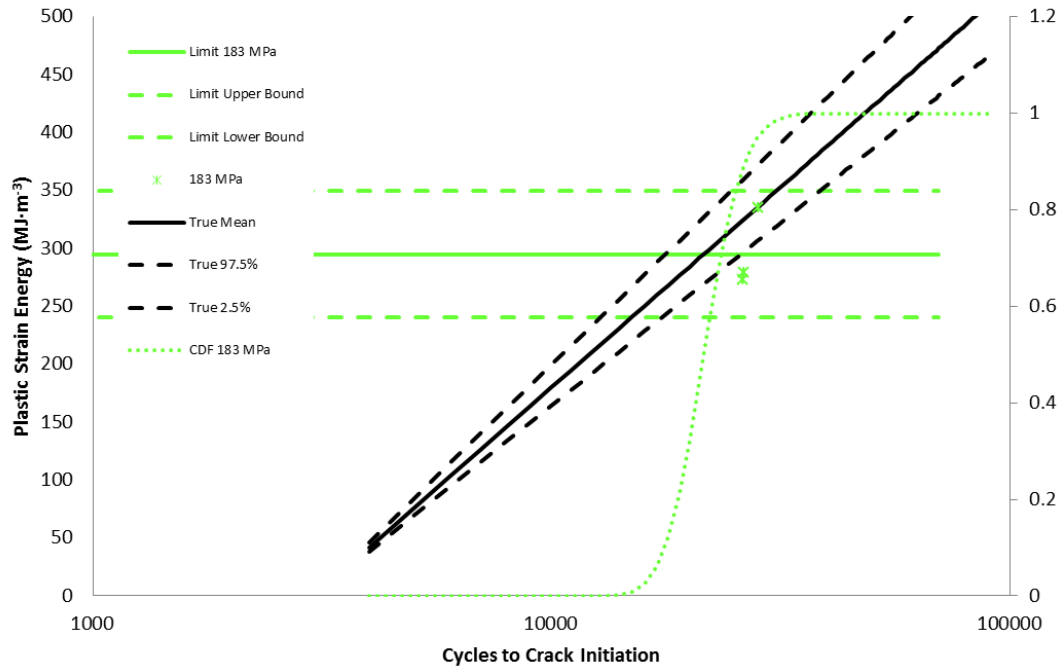
Figure 4.20: Probability of crack initiation for 183 MPa, R=0.1 using plastic strain energy density.

The probability of crack initiation can now be determined for each of the peak stresses. The probability for crack initiation at different peak loads with a loading ratio of 0.1 is shown in Figure 4.21.
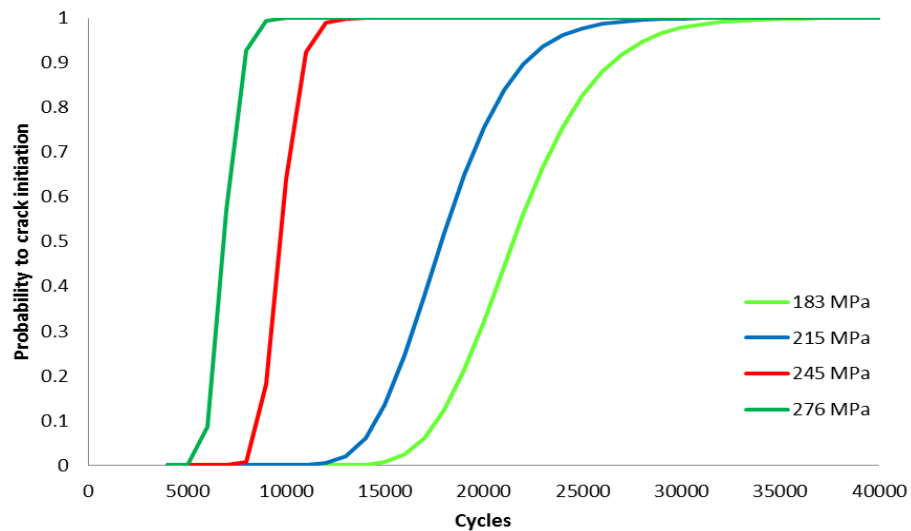
Figure 4.21: Probability of crack initiation for loading ratio of 0.1 using plastic strain energy density.

Additionally, since the model developed is shown to be capable of considering different positive loading ratios, the probability of crack initiation for a loading ratio of 0.4 is shown in Figure 4.22.

As discussed earlier, the strain energy density increases monotonically with the number of cycles (Eq. 4.12) and from the literature review, the energy per cycle remains constant throughout the test (Morrow, 1965.) The distribution of energy for failure is based on the peak load, shortly after the initiation of a fatigue test, once the hysteresis has stabilized, all that is needed to determine the probability of crack initiation is the peak stress and load ratio to determine which probability curve to follow.

In the following sections, a similar analysis will be undertaken using thermodynamic entropy generation.
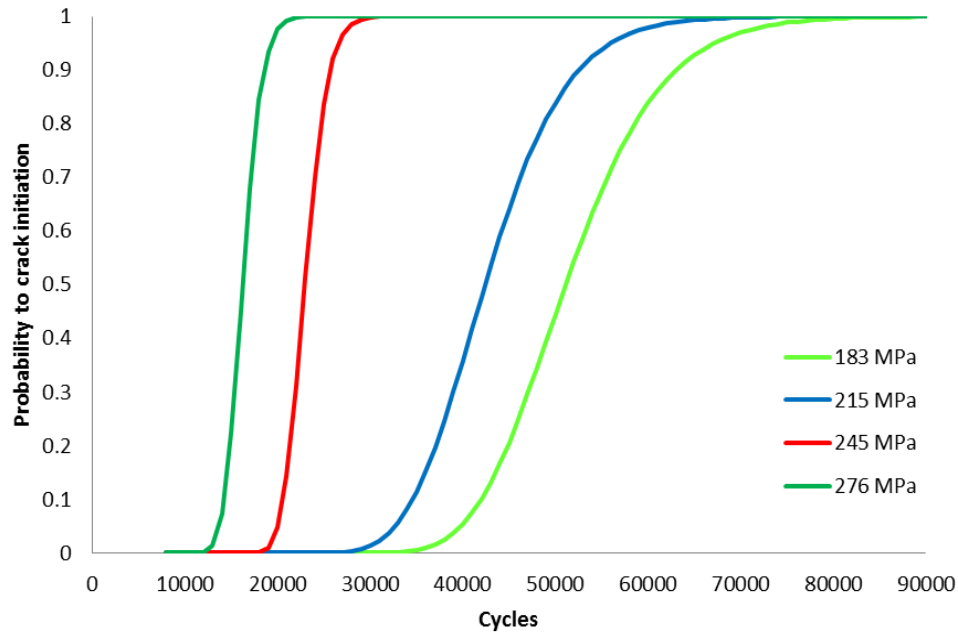
Figure 4.22: Probability of crack initiation for loading ratio of 0.4 using plastic strain energy density.

4.5 Thermodynamic Entropy

Following the discussion in Chapter 2, the thermodynamic entropy generation can be calculated for each cycle by:

$$\dot{s}_i = \frac{\sigma : \dot{\varepsilon}_p}{T} - \frac{A_k V_k}{T} - \frac{YD}{T} - \frac{1}{T^2} \dot{q} \cdot \boldsymbol{gradT} . \qquad (4.28)$$

The temperature change during each experiment was very small, on the order 1-3 degrees (See Figure 2.6). Using the method outlined by Meneghetti (2007), the thermal dissipation energy was estimated. The resulting energy was found to be on the order of 10-15% for different experiments. In the development of Eq. (4.28), it is noted that the energy dissipation associated with the internal variables is a small percentage, often on the order of 5-10%, of the plastic strain energy density, and is therefore often neglected (Lemaitre and Chaboche, 1990). The calculated heat energy is in the form of total thermal dissipation energy, including conduction, convection and radiation (Meneghetti, 2007). The final term in Eq. 4.37 is only a function of the conductive thermal dissipation, which is only a fraction of the total heat energy. Therefore, similar to earlier entropic studies on fatigue (Naderi et al., 2010) the entropy generation due to heat conduction will be considered negligible and the entropy generation per cycle will be determined by:

$$\dot{s}_i = \frac{\sigma : \dot{\varepsilon}_p}{T} - \frac{A_k V_k}{T} - \frac{YD}{T} \qquad (4.29)$$

Recalling Figure 2.12, each of these terms is captured within the experimentally determined hysteresis loops.

The cumulative thermodynamic entropy generation until crack initiation for Al 7075-T651 at different load ratios, load amplitudes and tensile mean stresses are presented in Figure 4.23. Results show that entropy generation, similar to plastic strain energy density increases as the number of cycle to crack initiation increases. At higher load amplitudes (lower number of cycles to crack initiation), accumulation of entropy generation is lower and

it increases as the load amplitude decreases. Also, at a given number of cycles the entropy accumulation is lower for higher load ratio.
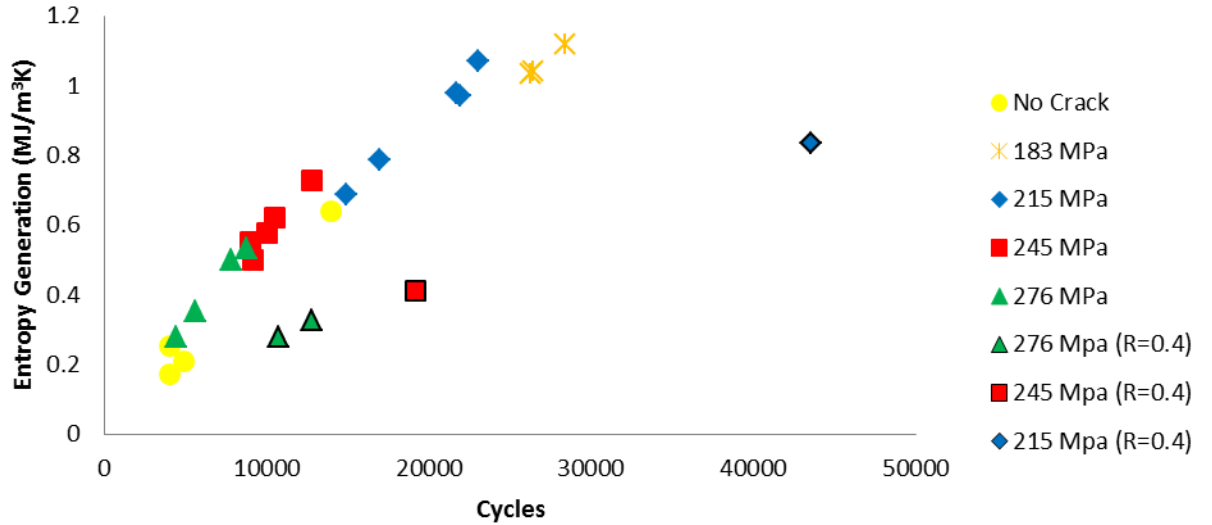
Figure 4.23: Entropy generation at crack initiation

The trend seen in the thermodynamic entropy generation is very similar to that seen in the plastic strain energy density (See Figure 4.1) which is a result of how the entropy is calculated. The entropy calculation in Eq. 4.29 depends on what is captured in the hysteresis loop and the temperature. Since the temperature does not vary considerably during each experiment, the trend is dominated by the plastic strain energy density.

Just as the results for the plastic strain energy density presented in Figure 4.1 differed from the plastic strain energy density results for the 40 P3 aircraft (See Figure 1.2), the results presented in Figure 4.23 differ from the previous entropic studies on fatigue life (Naderi et. al., 2010; Naderi and Khonsari, 2010) which claimed a constant entropy generation at the point of full fracture. This difference suggests that there may be a limit at which $\Delta\varepsilon_p$ no longer results in an increased density of PSBs or increased probability of mesocracks being within a threshold distance. Sornette (1992) hints at this by stating that for strain controlled experiments, within the LCF regime, stress amplitudes increase up to a steady state level (a plateau) likely resulting from cyclic hardening (Sornette, et. al., 1992; Magin et. al., 1984). In

the work by Naderi et al. (Naderi et al., 2010; Naderi and Khonsari, 2010) the entropy generation methodology was presented for un-notched specimens and for the LCF regime, where plastic deformation was dominant. It is possible that the strain ranges used in their work were within the steady state level hinted at by Sornette (1992). In the experiments presented in this work, the nominal stress amplitudes are comparably low due to the stress concentration at the notch. Consequently, the plastic deformation region is localized at the notch area which results in smaller entropy generation that otherwise could have been generated at high nominal stress amplitudes. This difference in loading conditions and specimen geometry contributed to the difference in results observed between the two studies.

Another major difference in the work presented by Naderi et al. (2010) when compared to this work is in the manner of plastic strain energy density dissipation calculation. In this work, the plastic strain energy density dissipation was determined using the hysteresis loops generated from actual stress and strain values taken during the experiment. These values also inherently include the entropy generation due to internal variables and elastic damage (Figure 2.12). In the works by Naderi et al. (2010), the plastic strain energy density is calculated using the relation (Eq. 2.2) presented by Morrow (1965) for fully-reversed, non-notched, plastic strain dominated loading conditions.

Noting that the experiments in this study do not fit the criteria for using these relations, fully reversed, plastically dominated loading, the relations are used for the sake of comparison. In Figure 4.24, the cumulative plastic strain energy density dissipation as determined through the use of Eq. (2.2) is presented. Two immediate differences are noticed. First, the data appears to be far less scattered. Second, the energies estimated are far greater than what was determined experimentally. In fact, comparing both sets of values presented in Table 2.1 the resulting estimations change by an order of magnitude. The results presented in Figure 4.25 show how influential the cyclic fatigue properties can be in an estimation of the strain energy density.

83
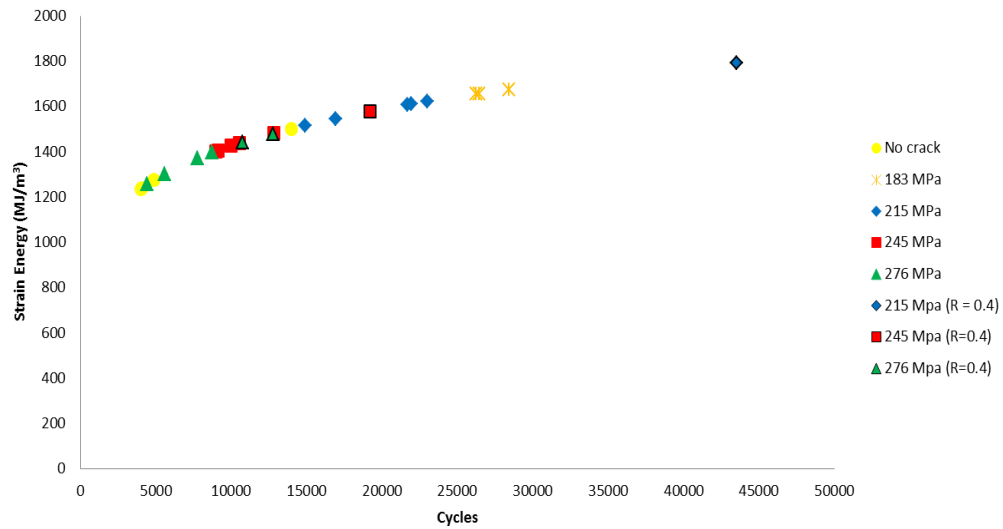
Figure 4.24: Equation (2.2) cumulative plastic strain energy density

The use of Morrow's equations for the calculation of the plastic strain energy density ultimately has an effect on the thermodynamic entropy calculation. Again, the results are far less scattered than those presented in Figure 4.24. The differences in the results presented in Figures 4.1 and 4.24 for strain energy density and Figures 4.23 and 4. 26 for thermodynamic entropy show how influential the use of an approximation can be when compared to experimentally generated results.

Ultimately, the change in plastic strain energy density effects the entropy estimation as well. This effect is seen in the results presented in Figure 4.26. The results for entropy generation in Figure 4.26 are two orders of magnitude larger than those found experimentally.
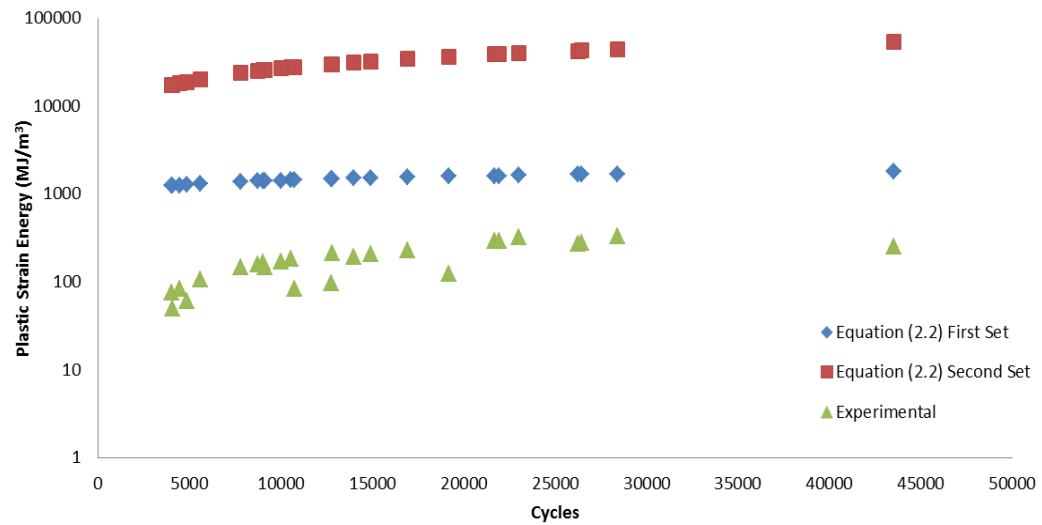
Figure 4.25: Effect of different material properties on strain energy density calculation.
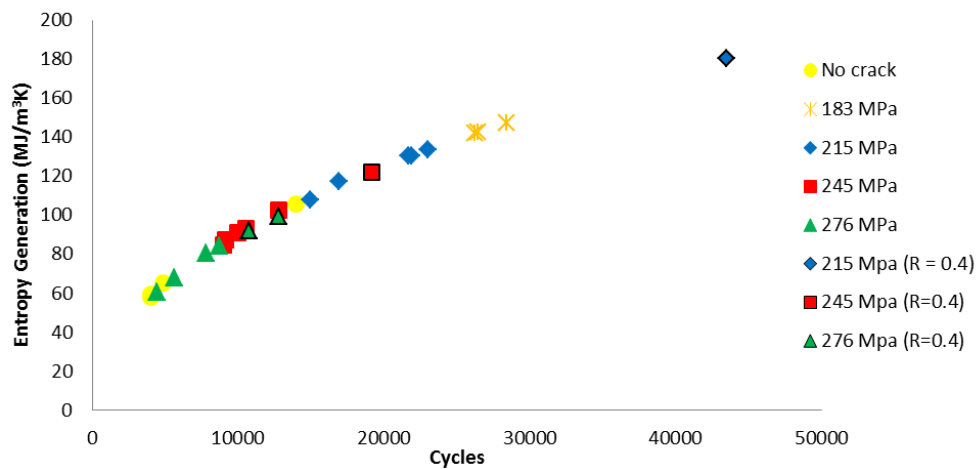
Figure 4.26: Cumulative Thermodynamic Entropy at crack initiation.

With so many similarities between the plastic strain energy density and the

thermodynamic entropy, similar trends were seen with respect to the cumulative entropies

being grouped based on peak load and not crack size as shown in Figure 4.27. Results for the

dog-bone specimens, shown in Figure 28, are similar to the plastic strain energy density

dissipation. The thermodynamic entropy generation differs only slightly between the point of

crack initiation and the full fracture of the specimen. Therefore, as with the plastic strain

energy density, no distinction will be made between the results stopped at the visual observation of a crack and full fracture of the specimen, both will be considered 'crack initiation' in this research.
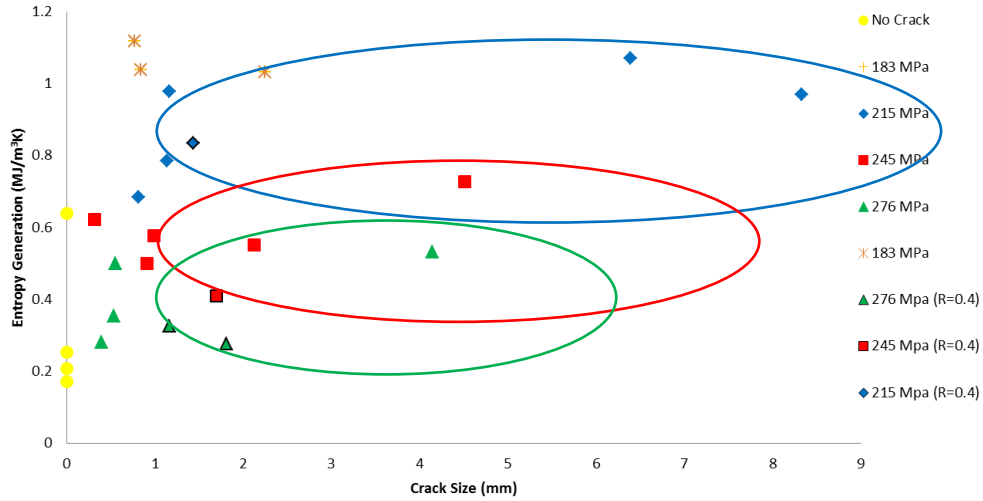
Figure 4.27: Entropy generation for varying crack sizes.
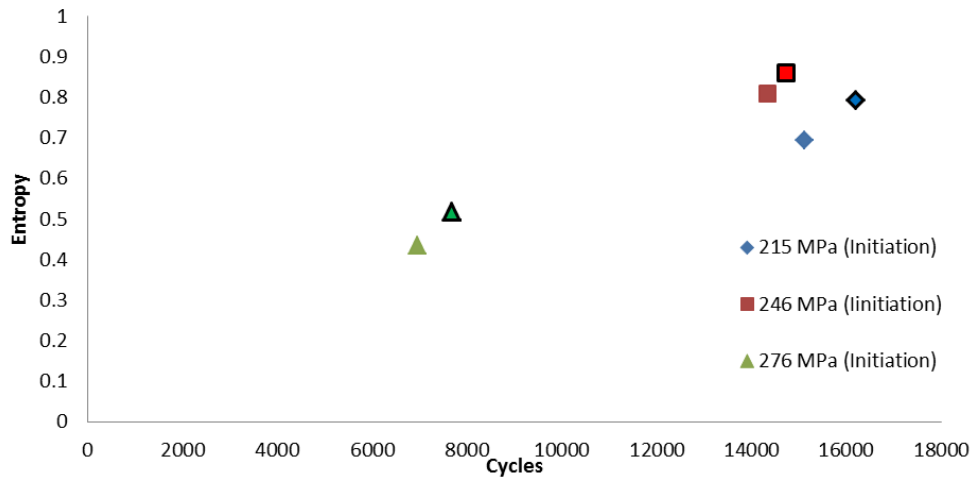
Figure 4.28: Entropy generation for dog-bone specimens at crack initiation and full fracture.

The results presented in Figures 4.23 and 4.27 show that for notched specimens under load ratios greater than zero, the cumulative entropy generation at the point of crack initiation follows an increasing trend is dependent on the peak stress and is independent of loading

86

ratio. This limited variation in strain energy density and temperature throughout the experiment may provide a means of easily predicting the state of the material with respect to crack initiation.
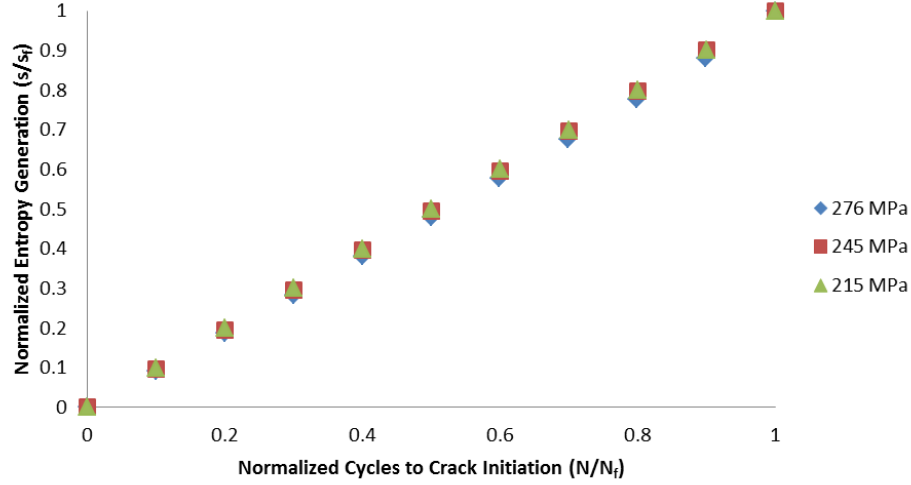
Figure 4.29: Normalized entropy generation vs. normalized cycles to crack initiation

Just as with the plastic strain energy density, in Figure 4.29 the normalized entropy generation for some of the different loading conditions used in this study are presented. The relation observed in Figure 4.29 can be expressed as:

$$\frac{s}{s_f} \cong \frac{N}{N_f}, \tag{4.30}$$

where s_f is the entropy generated at crack initiation for a particular set of loading conditions. This relation is the same as observed in the earlier entropy study on fatigue by Naderi et al. (2010). The resulting methodology for predicting failure, or crack initiation in this study, still holds. Using Eq. (4.30) the cycles to failure can be expressed as:

$$N_f \cong \left(\frac{N}{s}\right) s_f. \tag{4.31}$$

Therefore, for a known s_f, after an estimation of the entropy generation s at a cycle N, the fatigue life can be estimated. Since the energy, temperature and therefore entropy generation per cycle do not vary considerably during an experiment, the estimation of cycles remaining to failure can be made at any time during the experiment.

4.5.1 Deterministic model development

In the following sections the analysis will follow similar steps presented for the analysis of the plastic strain energy density. Different data sets will be used for deterministic model development, determination of the model error and estimation of the model bias and uncertainty for determination of the true value distribution. These true values will then be used to determine the probability of crack initiation.

Experimental data used in the initial deterministic, model development is presented in Table 4.5. The same form of the model used with the plastic strain energy density was chosen to capture the data. The model is of an exponential form:

$$N = a_s e^{b_s S},$$
(4.32)

where a_s and b_s are parameters fit using the thermodynamic entropy experimental results. The ability to model the experimental results while capturing the difference in changes between different load rations will be done by having different sub-models for parameters a_s and b_s. Just as with the model developed for the plastic strain energy density, the sub-model for parameter a_s was chosen to be a parabolic model:

$$a_s = a_s' R^2 + b_s' R + c_s'.$$
(4.33)

The sub-model for parameter b_s is a linear model:

$$b_s = d_s' R + e_s'.$$
(4.34)

where a_s', b_s', c_s', d_s' and e_s' are parameters fit using the thermodynamic entropy generation experimental data. Just as with the strain energy density, developing a model with the cycles as the independent variable, the equation for determining the entropy as a function of the cycles is:

$$S = \frac{\ln(N) - \ln(a_s' R^2 - b_s' R + c_s')}{d_s' R + e_s'}$$
(4.35)

Table 4.5: Data for deterministic model development.

R	s ($MJ \cdot m^{-3}K^{-1}$)	Max Stress (MPa)	Cycles
0.1	1.032	183	26259
0.1	0.785	215	16935
0.1	0.979	215	21701
0.1	0.727	245	12824
0.1	0.500	245	9121
0.1	0.499	276	7786
0.1	0.353	276	5609
0.4	0.277	276	10734
0.4	0.410	245	19188

The entire form of Eq. (4.35) is fit using the data presented in the Table 4.5. The initial model fit is done using the same simple linear regression technique of minimizing the differences between the model predictions to those observed in the experiments as in the development of the plastic strain energy density model. The results are presented in Figure 4.30.
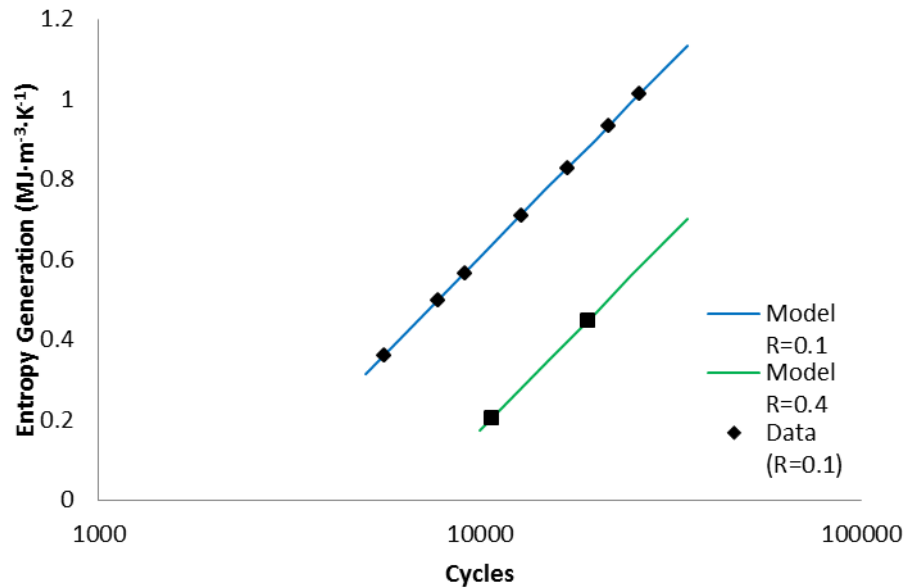
Figure 4.30: Deterministic model for entropy generation for cycles to failure using thermodynamic entropy.

The fitted forms of Eqs. (4.33) and (4.34) are

$$a = 28366.92R^2 + 0 \cdot R + 2101.14, \tag{4.36}$$

and

$$b = 0.002R + 2.37. \tag{4.37}$$

4.5.2 Model validation

In this section, the model developed in the previous sections will be challenged with respect to how accurately it matches data independent of its development and its usefulness in predicting the true cycles to failure given an estimation of the entropy.

4.5.3.1 Model validation – additional loading conditions

Just as with the strain energy density model assessment, the first test will be a subjective qualitative assessment. In Figure 4.31 the models, for loading ratios 0.2 and 0.3 are presented. Included in Figure 4.31 are entropy generation at crack initiation results for experiments conducted with a peak stress of 245 MPa and load ratios of 0.2 and 0.3. The experimental results shown in Figure 4.36 are those of experiments run independent of the model development. These results suggest the models do an acceptable job predicting the outcome at different loading ratios. Also observed in Figure 4.31 is, once again, the distinction that the entropy at crack initiation is dependent on the peak stress and not the cycles to failure as the data was developed for experiments run with a peak stress of 245 MPa.
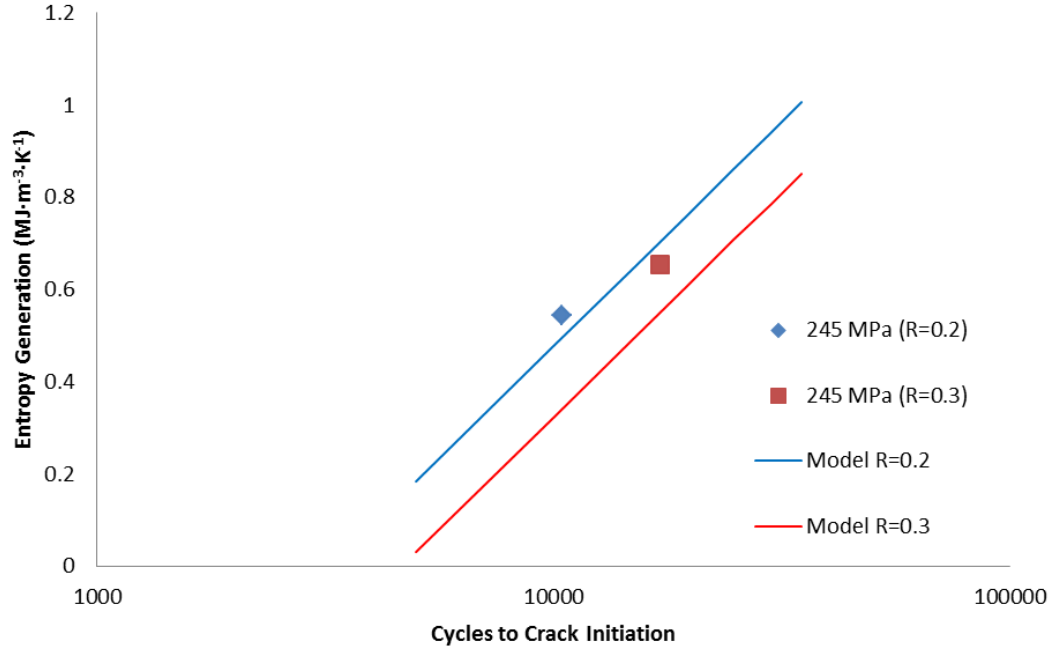
Figure 4.31: Comparison of predicted model and experimental results for 0.2 and 0.3 load ratios using thermodynamic entropy.

The experimental uncertainty will be very similar to that of the plastic strain energy density, as the entropy calculation is a function of the plastic strain energy density. However, now the uncertainty in the temperature measurements must also be considered. The IR sensor and IR camera both have an uncertainty of ±1% for the temperature ranges seen in these experiments. Therefore, the experimental uncertainty is still dominated by the uncertainty in the strain measurements made by the extensometer. The experimental uncertainty used in this analysis is ±10.1%. The resulting summary statistics for the model prediction are shown in Table 4.6.

The model uncertainty bounds can be determined from the percentiles of F_m. The resulting upper bound has increased to 17.4%, while the new lower bound is -11.9%. This is shown graphically in Figure 4.32. These results are slightly better than those of the plastic strain energy density (-44.9%, -20.8%). This is not unexpected for two reasons. First, the determination of the thermodynamic entropy included all the evidence used in the

determination of the plastic strain energy density as well as the inclusion of additional

evidence, the temperature change of the specimen during fatigue. Secondly, while not as

significant, the inclusion of the temperature measurements results in a, very, slight increase to

the estimated experimental uncertainty included in the analysis. Similar to the model

developed for the plastic strain energy density, this model appears to under predict the true

energy at crack initiation. This under prediction is very slight with an F_m of 1.02. And this

magnitude of the bias in the model is made clear by the comparison of the mean True Mean

and the Perfect Match Line in Figure 4.32.

Table 4.6: Summary statistics for model bias and uncertainty.

Parameter	Mean	STDEV	2.50%	97.50%
b_m	0.018	0.025	-0.031	0.068
s_m	0.057	0.029	0.007	0.122
F_m	1.020	0.071	0.880	1.174
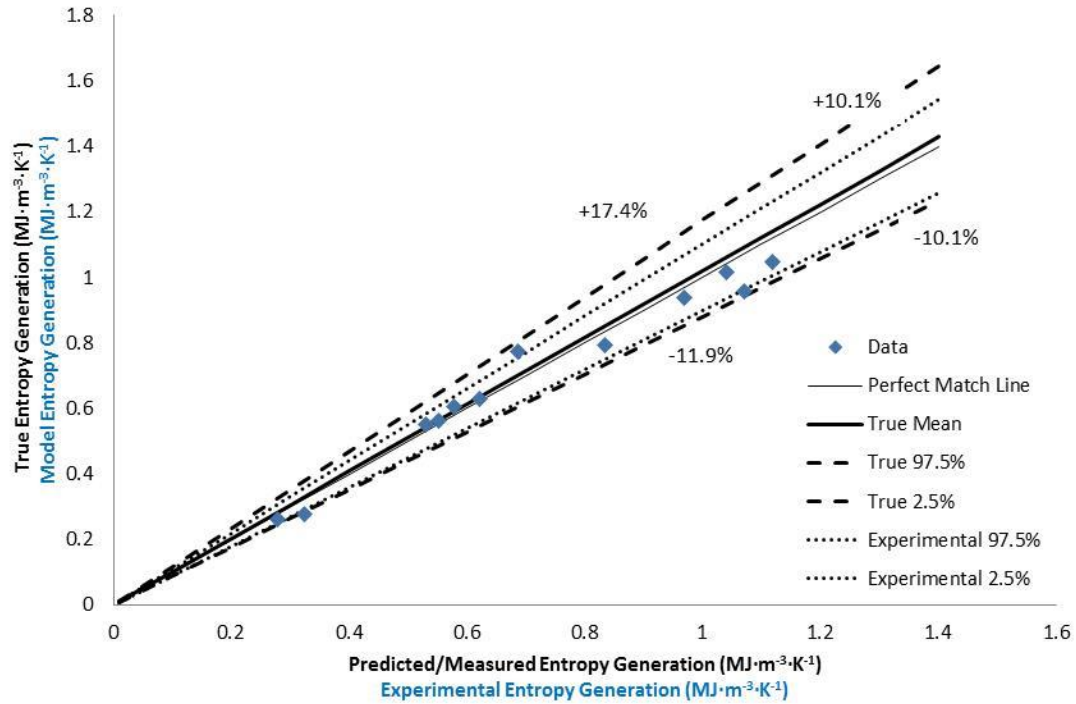
Figure 4.32: True value distribution of cycles given a distributed model prediction using thermodynamic entropy.

With an estimation of the F_m distribution, the distribution of the true entropy generation given the cycle number can be determined using the model predictions. This true value distribution is shown below in Figure 4.33.
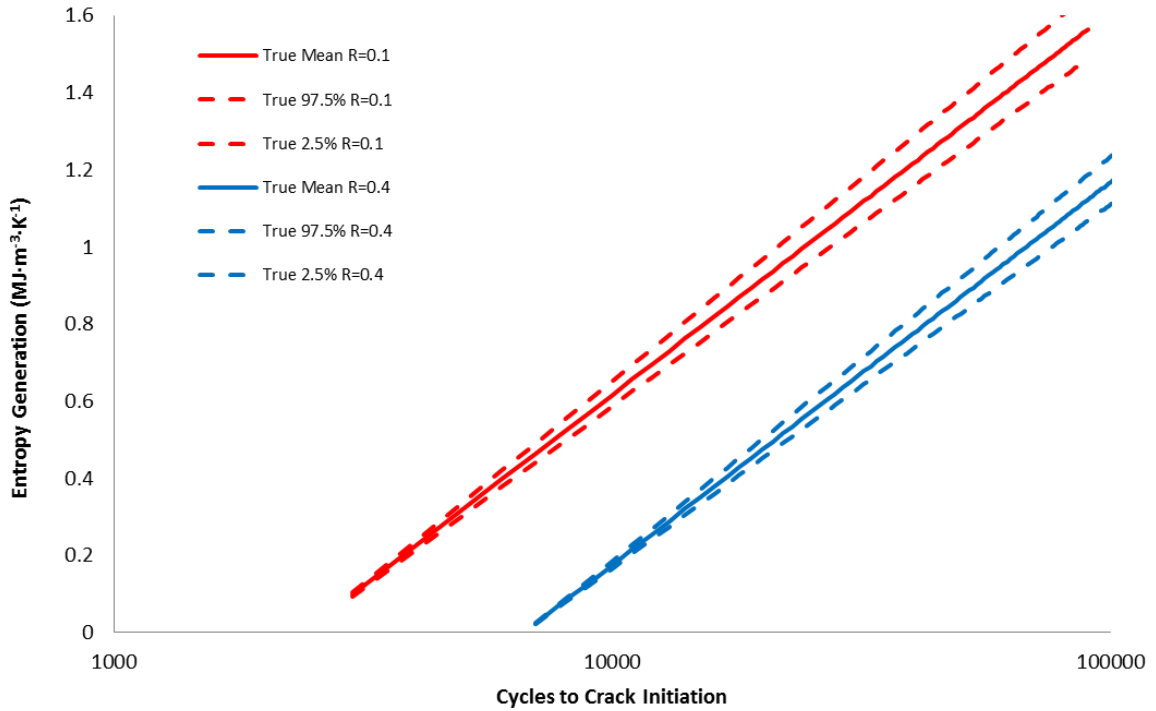
Figure 4.33: True value distribution for 0.1 and 0.4 load ratios using thermodynamic entropy.

Recalling the values presented for the loading ratios of 0.2 and 0.3, the value of F_m will now be used to correct the model to estimate the true value and compare the results. In Figure 4.34 the results for two experiments with a peak load of 245 MPa and at load ratios of 0.2 and 0.3 are shown. No data of load ratios 0.2 and 0.3 was use in the development of the model. The models appeared to slightly under predict the values. With an F_m value of 1.02, it was confirmed that the model was slightly under predicting the true value. The data presented in Figure 4.34 is not the true value, given that experimental values can be uncertain (See Eq. 4.24), but the correction to the model by the application of the multiplicative error of the model prediction, F_m, which does appear to increase the accuracy of the model's predictions.
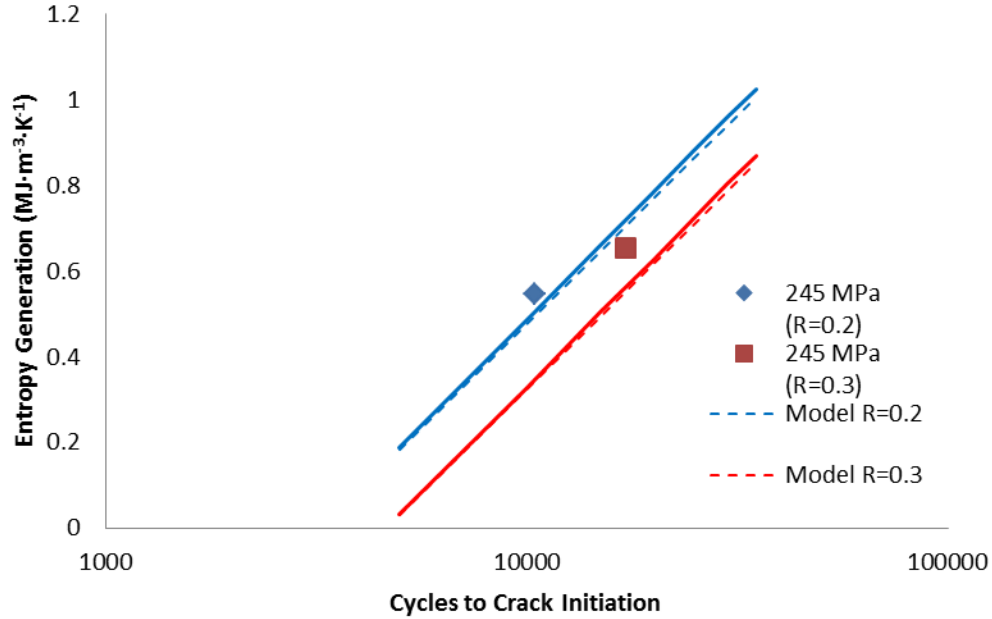
Figure 4.34: Comparison of model prediction and mean true value estimation using thermodynamic entropy.

4.5.4 Probability of crack initiation

Just as with the plastic strain energy density, there is no single entropy value that determines crack initiation, but varies depending on the peak stress. The goal is to determine the interaction between the two distributions, the model distribution as it approaches the limit distribution for a certain peak loading condition. Once again the stress-strength interaction relationship will be used.

The result for the 183 MPa limit is shown in Figure 4.35. A quick glance shows how the probability starts to increase once the two distributions start to interact. Additionally, the probability of a crack initiating is around 50% when the two distributions overlap, which from the discussion above, is more reasonable that a probability of 100% when using the area of interaction between the two distributions. Here, the probability of a crack initiating is 100% around 45,000 cycles.
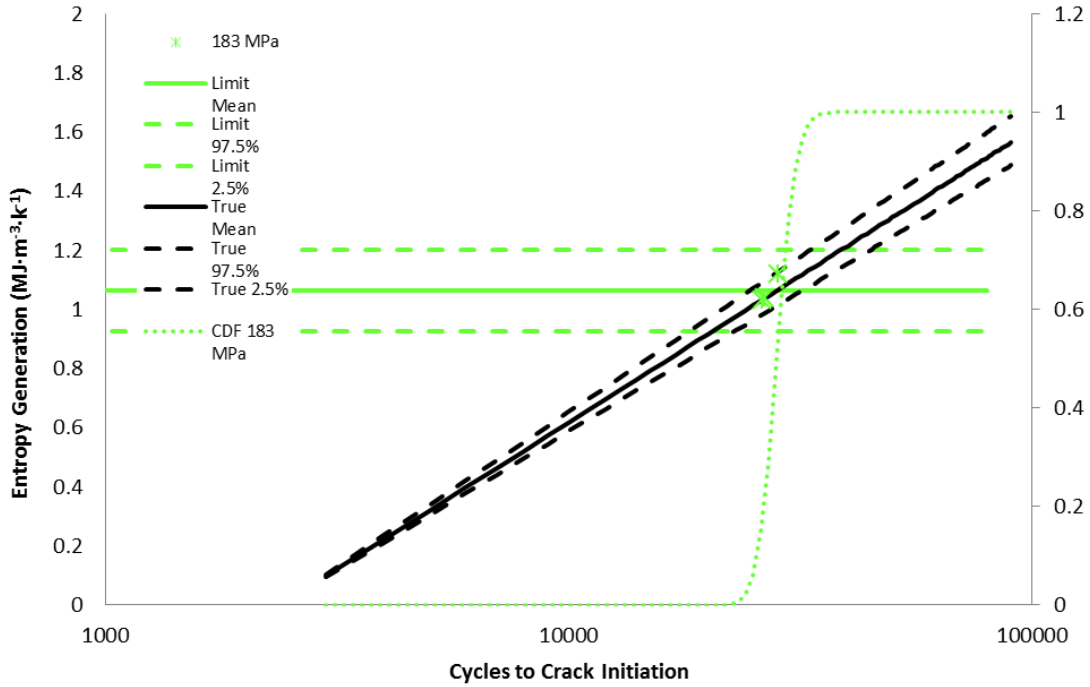
Figure 4.35: Probability of crack initiation for 183 MPa, R=0.1 using thermodynamic entropy.

The probability of crack initiation can now be determined for each of the peak

stresses. The probability for crack initiation at different peak loads with a loading ratio of 0.1

is shown in Figure 4.36. The results are similar to those found for the plastic strain energy

density. In the next section a comparison on the results will be made.

Similar to the plastic strain energy density, the thermodynamic entropy increases

monotonically with the number of cycles (Eq. 4.30). The plastic strain energy density per

cycle remains constant throughout the test and the temperature variations during the test are

minute (Figure 3.21), it can be assumed that the entropy generation per cycle is relatively

constant. The distribution of entropy for failure is based on the peak load, shortly after the

initiation of a fatigue test, once the hysteresis has stabilized, all that is needed to determine

the probability of crack initiation is the peak stress and load ratio and which probability curve

to follow.
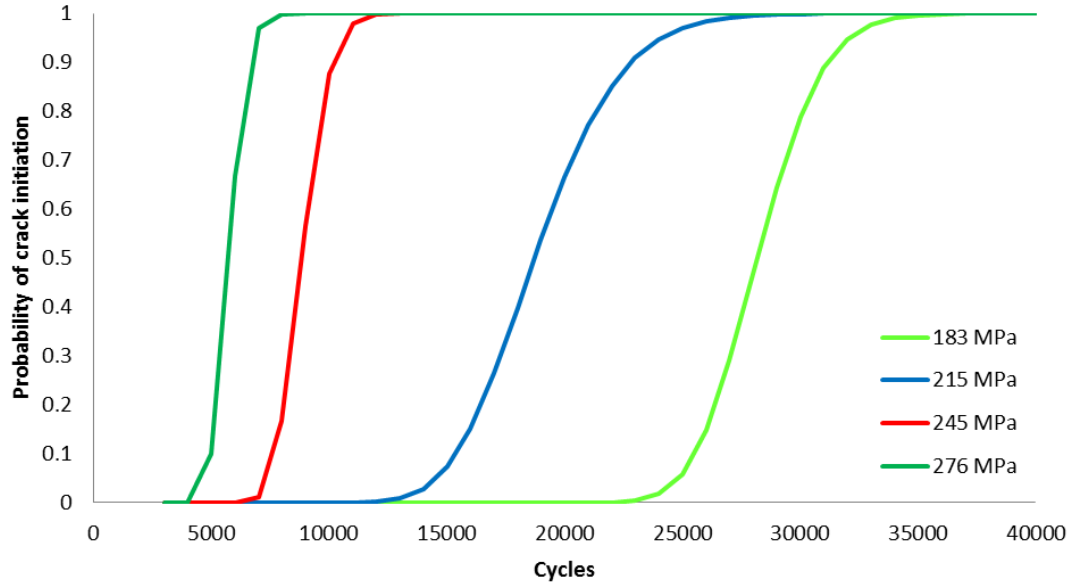
Figure 4.36: Probability of crack initiation for loading ratio of 0.1 using thermodynamic entropy.

4.6 Comparison of plastic strain energy density and thermodynamic entropy

The probability of crack initiation at a given cycle can now be determined using both the plastic strain energy density and the thermodynamic entropy. In Figure 4.37 the probability of crack initiation for different peak stresses with an R=0.1 for both plastic strain energy density and thermodynamic entropy are presented for comparison. However, the trends among the two properties for the peak stress of 183 MPa are noticeably different. This is a result of the assumed limit distributions. The limit distributions were developed using limited experimental data (See Figure 4.17.)

The coefficient of variation (COV) allows for a normalized comparison of dispersion of probability distributions. A comparison of the COVs for the distribution limits assumed for the plastic strain energy density and thermodynamic entropy are presented in Table 4.7.

96

Table 4.7: Coefficient of variations for plastic strain energy density and thermodynamic

entropy at different peak stresses

Physical property	183 MPa	215 MPa	245 MPa	276 MPa
Plastic strain energy density COV	0.116	0.177	0.141	0.283
Thermodynamic entropy COV	0.045	0.162	0.191	0.294
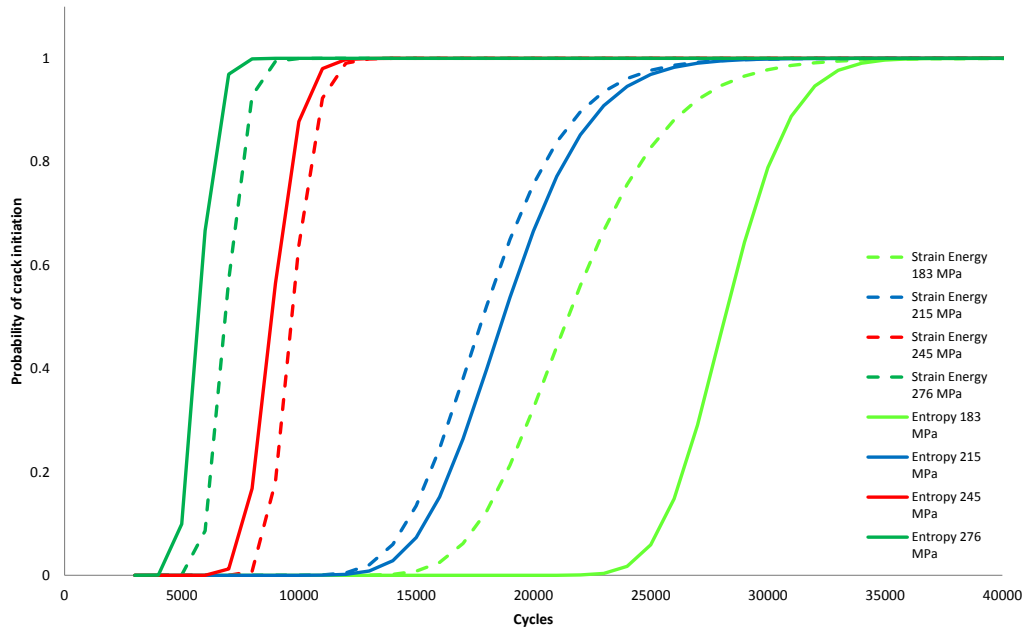
Figure 4.37: Comparison of probability of crack initiation for different peak stresses with an R =0.1 using plastic strain energy density and thermodynamic entropy.

It is clear that there is an issue with distributions for the peak stress of 183 MPa. This

is a byproduct of developing assumed limit distributions using such limited data. Reviewing

Figure 4.17, while none of the limit distributions were constructed using a sizable amount of

evidence, the distribution for the peak stress of 183 MPa had the least with only three

experimental results. When comparing Figure 4.1 and 4.23 it is clear that the evidence used

to determine the limit distributions for each physical property are from the same experiments,

as the entropy calculations make use of the same plastic strain energy density but include the

measured temperatures. It appears that the inclusion of the measured temperatures reduced

the scatter between the entropy estimations for the experiments conducted with a peak stress

of 183 MPa.

While the results presented in 4.37 show that both models predict similar probabilities for crack initiation, recalling Figures 4.18 and 4.32, the uncertainty on reality using the entropy model is less (+17.4%, -11.9%) than the model using plastic strain energy density (+44.9%, -20.8%). Therefore, it suggests, that while similar, the model using thermodynamic entropy provides a better estimation of the true probability of crack initiation. However, consideration must be made with respect to the ability to gather temperature data. The data used to develop these models was taken using controlled experiments. As shown in Figure 3.21 the temperature increase during the experiment is very limited. Also shown in Figure 3.21 is the effect of standing to close to the specimen during the experiment. Simply standing near the sample can result in an incorrect estimation of the temperature, and therefore an incorrect determination of the thermodynamic entropy generation. Recalling that the genesis of this research was predicting crack initiation in Navy fleet aircraft, consideration of the temperature changes observed during operation of these aircraft must be considered. It would be difficult to accurately capture the temperature change that results from fatigue during operation of an aircraft. In fact, the temperature over the length of the aircraft, while not in operation, likely varies more than the 1-2 degrees observed in the experiments performed for this work. During flight it is far less reasonable to believe the temperature could be taken with any great certainty. As the results for the different models are not significantly different, given the challenge posed with accuracy measuring the temperature change that results from fatigue, the model using the plastic strain energy density is sufficient.

Chapter 5: Conclusions and Recommendations

5.1 Summary

Given the challenge posed on inspecting fleets of aircraft, new methods must be explored. Recent areas of research at the University of Maryland have explored means of developing physics-based, probabilistic methods for risk assessment and management of ageing aircraft. Therefore, a framework for predicting crack initiation without the reliance on conservative safety factors is developed and can be used in establishing guidelines of safe and cost effective maintenance scheduling. The research presented in the dissertation is focused on physics-based approach for determination of crack initiation with applications to prognostic health monitoring.

The capability of two quantities and their ability to predict the point of crack initiation resulting from fatigue were studied in depth. The first of which was the plastic strain energy density. Experimental data was developed using a material used in airframe construction, Al 7075-T651. Test specimens were developed based on geometries representative of airframe construction. Data developed in these experiments was used to determine the cumulative plastic strain energy density dissipation over the course of a fatigue test. Using these results for different loading conditions, a probabilistic model was developed for predicting the plastic strain energy density dissipation for different loading conditions. . A Bayesian inference was used to determine the model bias and uncertainty thru a comparison between model predictions and independently generated experimental measurements. As a result the 'true' distribution of energy was able to be determined given a model prediction. Using these results the probability of a crack initiating at a given number of cycles, for different loading conditions determined by the plastic strain energy density dissipation was estimated.

The second quantity studied was the thermodynamic entropy generation. Found to be closely related to the plastic strain energy density, the estimation of this quantity included additional evidence thru the capture of the increase in temperature resulting from the hysteresis effect during fatigue. Similar to the analysis performed with the plastic strain energy density, experimentally generated results were used to model the cumulative entropy generation at a given cycle for different loading conditions. The bias and uncertainty of the model developed were determined by comparison with independent experimental results allowing for an estimation of the true entropy generation given a number of cycles. Once again, the results of this model were used to estimate the probability of a crack initiating as the cycles increase for different loading conditions.

The similarities of the two models were presented and discussed. The challenge of obtaining temperature data for use with the thermodynamic entropy model was reviewed.

The results developed in this methodology have significant potential to be used as a non-destructive means of providing an evidence driven prognostic and structural health modeling the remaining useful life.

5.2 Contributions

Major contributions of this research are as follows:

- The feasibility of estimating crack initiation by using plastic strain energy density dissipation in constant amplitude loading under positive load ratios modeled.
- The feasibility of estimating crack initiation by using thermodynamic entropy generation in constant amplitude loading under positive load ratios modeled.
- A probabilistic model developed to capture the relation between plastic strain energy density dissipation and cycles to crack initiation resulting from fatigue loading. Model bias and uncertainties were estimated using experimental data obtained as a part of this research.

- A probabilistic model developed to capture the relation between thermodynamic entropy generation and cycles to crack initiation resulting from fatigue loading. Model bias and uncertainties were estimated using experimental data obtained as a part of this research.

- It was determined that for notched specimens under, constant, positive amplitude loading the plastic strain energy density at crack initiation was a function of the peak stress, independent of loading ratio. This confirms the historical evidence that the strain energy density increases with cycles to failure. This differs from the results that served as the genesis for the research topic which showed a seemingly constant plastic strain energy density at crack initiation.

- It was determined that for notched specimens, under, constant, positive amplitude loading the cumulative thermodynamic entropy generation at crack initiation was a function of the peak stress, independent of loading ratio. This differs from the results that showed for Al-6061-T6 a constant entropy generation at full fracture.

- The difference in results between the plastic strain energies at crack initiation determined in this study and those of the 40 P-3 aircraft has been proposed to be an artifact of the relation between the point of crack initiation and it's relation to the damage index used in the Navy safe-life approach, the fatigue life expenditure, FLE.

- The difference in thermodynamic entropy results to those published in the literature has been proposed as a difference in loading conditions, primarily plastic deformation in earlier entropic studies and primarily elastic, with the effect of a notch, in this study.

Major potential benefits of this research project include:

- Provide a means of estimating crack initiation without the reliance on conservative safety factors often used with the established empirical measures such as the Palmgren-Miner rule.

- Prediction of crack initiation using physics-based models developed for plastic strain energy density dissipation and thermodynamic entropy generation for non-destructive testing approach.

- Data driven prognosis to support risk-informed decisions.

- Provide information for condition-based monitoring.

- Maximize the periodic inspection intervals while minimizing the risk and reduce costly downtimes.

5.3 Recommendation for future work

In this section some topics for potential future work are presented. Future research in this area will be more productive if focused on ideas highlighted below:

- The results obtained in this research were for constant amplitude loadings, under positive loading ratios. Updating the model, if required, for compressive loading would greatly increase its applicability.

- Spectrum loading would have on the results and updating the model appropriately would benefit this area of research.

- The models developed for both plastic strain energy density and thermodynamic entropy predict a negative energy for a low cycle to failure. Additional experiments at higher stresses not studied in this research could result in a correction to the current model or perhaps an additional model should there a change in the physics be found as suggest when attempting to explain the results of previous entropic studies.

- It would be interesting to study the results of the 40 P-3 aircraft that served as the genesis of this research to find if in fact the similarities between how each aircraft is

flown results in a cumulative plastic strain energy density dissipation 'limit' for the different flights and is found to be similar to that found for individual loading conditions.

- The models presented for both plastic strain energy density and thermodynamic entropy are only applicable for Al 7075-T651. It would be beneficial to obtain data for additional airframe materials such they could be studied. This task would require a considerable undertaking of additional experiments.

- The use of different specimens, the coupon design and the dog-bone specimens allowed for a hypothesis that the plastic strain energy density and thermodynamic entropy models are geometry independent. Performing experiments using more complex geometries could confirm this.

Appendices

Appendix 1: Hysteresis loop calculation

```matlab
%Show MATLAB where to start the data
 ni_st=2195; % first element for synchronization
 ni_en=2681040; % final element for synchronization

% Use INSTRON Load and Extensometer Strain
 usestress = ((data(ni_st:ni_en,8)*4.4428)/0.000323)*2.37; %Converts
kip to kN the divides by area resulting in kPa,
 %============================
 % Correct the strain from the extensometer based on the stress of
the test
 %
 %
 %============================

%12 1.311284733 1.239950798 1.168616863 2.73
 %14 1.323966606 1.250396492 1.176826378 2.37
 %16 1.322859928 1.252887396 1.182914865 2.095421318
 %18 1.362012224 1.281733575 1.201454926 1.881982894

 % constants for the test
 a100p=1.323966606;
 a50p=1.250396492;
 a0p=1.176826378;

extstrain=data(ni_st:ni_en,9);
 sign = zeros(1,length(extstrain(:)))';
 differ = ones(1,length(extstrain(:)))';
 apercent=0;
 for i=1:length(sign)
 if i==1
 sign(i)=2;
 end
 if i>=2
 differ(i)= extstrain(i)-extstrain(i-1);
 if differ(i)<0 && differ(i-1)>0
 sign(i-1)=1;
 end
 if differ(i)>0 && differ(i-1)<0
 sign(i-1)=2;
 end
 end
 end

 i3=1; % This is the count variable which tells the next loop to
begin counting until a set (including 1 0 and 2) is made
 for i2=1:length(sign)
```

```matlab
 if i3==1 && sign(i2)==2 % this is when the count (i3) is 1 and the
sign value is 2
 trig=1; % the trigger value signifies when to stop counting (1) and
begin calculation
 end
 if i3==1 && sign(i2)==1 % this is when the count (i3) is 1 and the
sign value is 1
 trig=2; % the trigger value signifies when to stop counting (2) and
begin calculation
 end
 if sign(i2)==trig % if trig=1 then the difference between max and
min strain is taken
 if trig==1
 adiff=extstrain(i2)-extstrain(i2-i3+1); % the difference between
max and min strain
 aperc_=(extstrain(i2)-extstrain(i2-i3+1:i2))./adiff; % percentage
of strain at this particular curve
 amax=extstrain(i2); % defines the max strain at this point
 trig=2; % the trigger value signifies when to stop counting (2) and
begin calculation
 elseif trig==2
 adiff=extstrain(i2-i3+1)-extstrain(i2); % the difference between
max and min strain
 aperc_=(extstrain(i2-i3+1)-extstrain(i2-i3+1:i2))./adiff; %
percentage of strain at this particular curve
 amin=extstrain(i2); % defines the min strain at this point
 trig=1; % the trigger value signifies when to stop counting (1) and
begin calculation
 end
 apercent=[apercent;aperc_(1:i3-1)]; % cumulation of the total
percentages for the entire strain vector
 i3=2;
 else
 i3=i3+1; % increases the count by 1
 end
 if i2==length(sign) % calculates the remaining strain at the end
 aperc_=(amax-extstrain(i2-i3+2:i2))./adiff; % percentage of strain
at this particular curve
 apercent=[apercent;aperc_]; % cumulation of the total percentages
for the entire strain vector
 end
 end
 apercent=apercent(2:length(apercent)); % the final total percentage
vector for the strain vector

for i4=1:length(sign)
 if apercent(i4)>=0 && apercent(i4)<.5 % calculate the strain
multiplication constant as a linear equation (0-50%)
 m=(a50p-a0p)/.5;
 b=a0p;
 else % calculate the strain multiplication constant as a linear
equation (50-100%)
 m=(a100p-a50p)/.5;
 b=a50p-m*0.5;
 end
 aconst(i4,1)=b+m*apercent(i4); % strain multiplication constant
vector
```

```matlab
  end

usestrain= (extstrain(:).*aconst)/100; % strain multiplication
constant vector times strain vector to yield modified strain vector


%========================================

n = 2678845; % Will have to change this such that it represents the
time to crack initiation. -needs to be ni-st-ni_en
 for i=1:n-1 %Will have to fill in values for which ever is less
than the other
  if usestress(i,1) < usestress(i+1,1)
 Top(i,1) =((usestress(i+1,1)+usestress(i+1,1))/2) *
((usestrain(i+1)-usestrain(i)));
 else
 Bottom(i,1) = (usestress(i,1)+usestress(i+1,1))/2 * ((-
(usestrain(i+1)-usestrain(i))));
 end
 end

Plastic = sum(Top - Bottom);
Elastic = sum(Bottom);
Total = sum(Plastic + Elastic );
```

Appendix 2: WinBUGS code for model bias and uncertainty determination

```
+model;
{

        bm~dunif(-1,1)
        sm~ dunif(0,1)
        taum<-1/pow(sm,2)
        pe<-0.1004

        be<-(log(1+pe)+log(1-pe))/2
        se<-(log(1+pe)-log(1-pe))/(2*1.95996398454005)

        bt<-bm-be
        st<-sqrt(pow(sm,2)+pow(se,2))

        C <- 1000

         for( i in 1 : N ) {
                        zeros[i] <- 0
                        L[i] <- pow(exp(-0.5*pow((log(x[i,2]/x[i,1])-
bt)/st,2))/(sqrt(2*3.141592654)*st)/(x[i,2]/x[i,1]),x[i,3])
                 ghr[i] <- ( -1) * log(L[i]) + C
        zeros[i] ~ dpois(ghr[i])
                                                        }
        fm~dlnorm(bm,taum)
```

```
        logfm<-log(fm)
                    for( j in 1 : 8 ){

yy[j]<-xx[j]*fm


}

}
```

list(x=structure(.Data=c(102.6853,105.144,1,301.5079,278.5863,1,282.3203,319.0262,1,275.
569,289.6895,1,166.3164,169.3175,1,250.4778,250.5059,1,311.5162,334.2564,1,222.0266,2
05.4605,1,173.4981,182.35,1,151.6342,165.2816,1,147.6524,158.3534,1,53.24433,83.52453,
1,81.13313,97.90399,1),.Dim=c(13,3)),N=13,xx=c(1,50,100,150,200,250,300,350))

Appendix 3: Plastic Strain Energy Density

R	Max Stress (MPa)	Experimental W (MJ·m^{-3})	Cycles
0	215	154.29	10391
0	276	105.1	5754
0.1	183	272.21	26259
0.1	215	230.21	16935
0.1	215	291.36	21701
0.1	245	213.2	12824
0.1	245	146.67	9121
0.1	276	146.49	7786
0.1	276	105.56	5609
0.1	183	278.6	26437
0.1	183	334.3	28409
0.1	215	319	23031
0.1	215	289.7	21940
0.1	215	205.5	14931
0.1	245	169.3	10004
0.1	245	182.3	10534
0.1	245	165.3	9002
0.1	276	158.4	8748
0.1	276	83.5	4438
0.4	276	83.028	10734
0.4	245	122.59	19188
0.4	215	250.5	43533
0.4	276	97.9	12757

Appendix 4: Entropy Generation

R	Max Stress (MPa)	Experimental S ($MJ \cdot m^{-3}K^{-1}$)	Cycles
0.1	183	1.032	26259
0.1	215	0.785	16935
0.1	215	0.979	21701
0.1	245	0.727	12824
0.1	245	0.5	9121
0.1	276	0.499	7786
0.1	276	0.353	5609
0.4	276	0.277	10734
0.4	245	0.41	19188
0.1	183	1.04	26437
0.1	215	1.07	23031
0.1	215	0.97	21940
0.1	245	0.58	10004
0.4	215	0.84	43533
0.1	183	1.12	28409
0.1	215	0.69	14931
0.1	245	0.62	10534
0.1	245	0.55	9002
0.1	276	0.53	8748
0.1	276	0.28	4438
0.4	276	0.33	12757

Appendix 4: Dog-Bone Results, Initiation

R	Max Stress (MPa)	Experimental W ($MJ \cdot m^{-3}$)	Experimental S ($MJ \cdot m^{-3}K^{-1}$)	Cycles
0.1	276	130.867	0.435	6966
0.1	245	242.675	0.810	14334
0.1	215	207.555	0.692	15114

Appendix 5: Dog-Bone Results, Full Fracture

R	Max Stress (MPa)	Experimental W $(MJ \cdot m^{-3})$	Experimental S $(MJ \cdot m^{-3}K^{-1})$	Cycles
0.1	276	155.691	0.518	9495
0.1	245	258.385	0.862	14730
0.1	215	237.545	0.792	16196

Appendix 6: Experimental Uncertainty Calculation

Plastic strain energy:
Stress ±1%
Strain ±10%

$$\tilde{U}_E: \sqrt{10^2 + 1^2} = 10.04$$

$$U_{c,E} = \frac{1}{\sum_{i=1}^{m} n_i} \tilde{U}_E n_i$$

n = 13, and since there is only one test series,

$$U_{c,E} = \frac{1}{13} 10.04 \cdot 13 = 10.04\%$$

Thermodynamic entropy:
Stress ±1%
Strain ±10%
Temperature ±1%

$$U_{c,E} = \tilde{U}_E: \sqrt{10^2 + 1^2 + 1^2} = 10.1\%$$

Bibliography

Abdel-Aziz, M., Mahmoud, T.S., Gaafer, A. M., 'Fabrication and Fatigue Behavior Study of Metal Matrix Composite,' 17th ECF17, Brno, Czech Republic 2008

Azarkhail, M., and Modarres, M., "A Novel Bayesian Framework for Uncertainty Management in Physics-Based Reliability Models", ASME International Mechanical Engineering Congress and Exposition, November 11-15, Seattle, Washington, USA., 2007

Azarkhail, M., Ontiveros, V., Modarres. M., "A Bayesian Framework for Model Uncertainty Consideration in Fire Simulation Codes." 17th International Conference on Nuclear Engineering, Brussels, 2009.

Abaqus Software, Dassault Systèmes Simulia Corp, Providence, RI, USA

Amiri, M., M. Naderi, and MICHAEL M. Khonsari. "An experimental approach to evaluate the critical damage." International Journal of Damage Mechanics 20.1 (2011): 89-112.

Bairstow, Leonard. "The elastic limits of iron and steel under cyclical variations of stress." Philosophical Transactions of the Royal Society of London. Series A, Containing Papers of a Mathematical or Physical Character 210 (1911): 35-55.

Basaran, Cemal, and Hong Tang. "Implementation of a thermodynamic framework for damage mechanics of solder interconnects in microelectronics packaging." International Journal of Damage Mechanics 11.1 (2002): 87-108.

Bhattacharya, Baidurya, and Bruce Ellingwood. "Continuum damage mechanics analysis of fatigue crack initiation." International journal of fatigue 20.9 (1998): 631-639.

BRAMMER, ANDREW THOMAS. EXPERIMENTS AND MODELING OF THE EFFECTS OF HEAT. Diss. The University of Alabama TUSCALOOSA, 2013.

Bryant, M. D., M. M. Khonsari, and F. F. Ling. "On the thermodynamics of degradation." Proceedings of the Royal Society A: Mathematical, Physical and Engineering Science 464.2096 (2008): 2001-2014.

Chang, C. S., W. T. Pimbley, and H. D. Conway. "An analysis of metal fatigue based on hysteresis energy." Experimental Mechanics 8.3 (1968): 133-137.

Coffin Jr, L. Fo. "A study of the effects of cyclic thermal stresses on a ductile metal." trans. ASME 76 (1954): 931-950.

COMSOL Metaphsics, COMSOL Inc. Stockholm, Sweden.

Dai S.H. and Wang, M. O. WANG. "Reliability analysis in engineering applications." (1992).

Dally, J.W., Riley, W. F., Experimental stress analysis. University of Michigan: McGraw-Hill, 1978.

Doelling, K. L., et al. "An experimental study of the correlation between wear and entropy flow in machinery components." Journal of Applied Physics 88.5 (2000): 2999-3003.

Droguett, Enrique Lopez. Methodology for the treatment of model uncertainty. DISS. The University of Maryland., College Park. 1999.

Enomoto, Nobusuke. "On fatigue tests under progressive stress." PROC ASTM. Vol. 55. 1955.

Epsilon Technology Corp., 'Model 3542 Axial Extensometers'http://www.epsilontech.com/pdf/3542.pdf, 2013

Feltner, C. E. "Strain hysteresis, energy and fatigue fracture,"." Dept. of Theoretical and Applied Mechanics, Univ. of Illinois, TAM Kept 146 (1959).

Feltner, C. E., Morrow, J., "Micro-plastic Strain Hysteresis Energy as a Criterion for Fatuige Fracture,' Transactions, Am. Soc. Mechcanicl Engrs., 83, Series D, Journal, Basic Engineering, (1961):15-22.

G.B. Wallis., "Contribution to the paper Statistical aspects of best estimate method-1 by Attila Guba, Makai M., Pa´l L", Reliability Engineering and System Safety 80309–11, 2003

Golos, K. M. "A total strain energy density model of metal fatigue." Strength of materials 27.1-2 (1995): 32-41.

Golos, K., and F. Ellyin. "A total strain energy density theory for cumulative fatigue damage." Journal of pressure vessel technology 110.1 (1988): 36-41.

Halford, G. R. "The energy required for fatigue(Plastic strain hystersis energy required for fatigue in ferrous and nonferrous metals)." Journal of materials 1 (1966): 3-18.

Halford, Gary R. The Fatigue Toughness of Metals: A Data Compilation. Department of Theoretical and Applied Mechanics, University of Illinois, 1964.

Halford, G. R., 'Plastic Strain Energy Analysis of Torsional Fatigue,' MS Thesis, University of Illiinios, Urbana, Ill. 1961.

Hamins, A., and K. B. McGrattan. "Verification and Validation of Selected Fire Models for Nuclear Power Plant Applications, Volume 2: Experimental Uncertainty." NUREG-1824 and EPRI 1011999 (2006).

Hansen, N. R., and H. L. Schreyer. "A thermodynamically consistent framework for theories of elastoplasticity coupled with damage." International Journal of Solids and Structures 31.3 (1994): 359-389.

Hanstock, R. F. "Damping capacity, strain hardening and fatigue." Proceedings of the Physical Society 59.2 (1947): 275.

112

Harig, H., and M. Weber. "Estimation of crack initiation in plain carbon steels by thermometric methods." Defects, Fracture and Fatigue. Springer Netherlands, 1983. 161-170.

Hodowany, Jon. On the conversion of plastic work into heat. Diss. California Institute of Technology, 1997.

Hoffman, P, "A Bayesian Approach to P-3 Structural Integrity Management," ICAF Presentation, International Committee on Aeronautical Fatigue, Germany, 2005

Hoffman, P., et al. "Strain energy density-Based Probabilistic Life Assessment of Dynamic," UMD-
NAWCAD Research Project Workshop. March 2010

Hurtado-Cahuao, Jose Luis. "Airframe integrity based on Bayesian approach," Dissertation The
University of Maryland, (2006).

Ince, A., and G. Glinka. "A modification of Morrow and Smith–Watson–Topper mean stress correction models." Fatigue & Fracture of Engineering Materials & Structures 34.11 (2011): 854-867.

Instron, 'Certificate of Calibration,' Instron Calibration Laboratory. 2012

Ital'yantsev, Y.F., 1984, Thermodynamic state of deformed solids. Report 1. Determination of local function of state, Strength Mater., 16, 238-241.

Iyyer, N., Phan, N., " Gap-fill Methods for Estimating Fatigue Damage" 7th Joint DoD/FAA/NASA Conference on Aging Aircraft; New Orleans, LA, 2003

Iyyer, N., Sarkar, S., Merrill, R., Phan, N., "Risk Assessment of P-3C Aircraft," 9th Joint DoD/FAA/NASA Conference on Aging Aircraft; Atlanta, GA , 2006.

Iyyer, Nagaraja, et al. "Aircraft life management using crack initiation and crack growth models–P-3C Aircraft experience." International Journal of Fatigue 29.9 (2007): 1584-1607.

Izumi, Y., M. E. Fine, and T. Mura. "Energy considerations in fatigue crack propagation." International Journal of Fracture 17.1 (1981): 15-25.

Jasper, T. M. "LXVII. The value of the energy relation in the testing of ferrous metals at varying ranges of stress and at intermediate and high temperatures." The London, Edinburgh, and Dublin Philosophical Magazine and Journal of Science 46.274 (1923): 609-627.

Jiang, L., et al. "Characterization of the temperature evolution during high-cycle fatigue of the ULTIMET superalloy: Experiment and theoretical modeling." Metallurgical and Materials Transactions A 32.9 (2001): 2279-2296.

Kelly, James M., and Peter P. Gillis. "Thermodynamics and dislocation mechanics." Journal

of the Franklin Institute 297.1 (1974): 59-74.

Kujawski, Daniel. "Fatigue failure criterion based on strain energy density." Mech. Teor. Stosow 27.1 (1989): 15-21.

L. Pal, M. Makai, "Remarks on statistical aspects of safety analysis of complex systems". arXiv:physics/0308086, 2004

L. Pal, M. Makai, "Statistical Considerations of safety analysis". arXiv:physics/0511140 v1, 2005

La Rosa, G., and A. Risitano. "Thermographic methodology for rapid determination of the fatigue limit of materials and mechanical components." International Journal of Fatigue 22.1 (2000): 65-73.

Lamas, J., Edwards, M., 'P-3C Service Life Assessment Program – Full Scale Fatigue Test,' Presented at the 22nd Symposium of International Committee on Aeronautical Fatigue, Lucerne, Switzerland, May 2003.

Lee, H. T., J. C. Chen, and J. M. Wang. "Thermomechanical behaviour of metals in cyclic loading." Journal of materials science 28.20 (1993): 5500-5507.

Lemaitre, J., Chaboche, J.L., 'Mechanics of solid materials,' First edn, University Press., Cambridge, UK. 1990

Levey, M. , Assessment of Damage Tolerance Requirements and Analyses AD-A175 110. Fairchild Industires, Farmingdale N.Y. September 1986

Levy, Meir. Assessment of Damage Tolerance Requirements and Analysis. Volume 1. Executive Summary. FAIRCHILD INDUSTRIES INC FARMINGDALE NY FAIRCHILD-REPUBLIC DIV, 1986.

Liaw, P.K., Wang, H., Jiang, L., Yang, B., Huangm, J.Y., Kue, R.C.,et. al., 'Thermographic Detection of Fatigue Damage, of Pressure Vessel Steels at 1000 and 20 Hz, Scripta Materiallia, 42, pp.389-395, 2000.

Ling, F. F., M. D. Bryant, and K. L. Doelling. "On irreversible thermodynamics for wear prediction." Wear 253.11 (2002): 1165-1172.

M. K. Cowles, "Review of WinBUGS 1.4", The American Statistician, Vol. 58(4):330-336, 2004

M. Pourgol-Mohamad. "Integrated Methodology for Thermal-Hydraulics Uncertainty Analysis (IMTHUA)," Ph.D Thesis; University of Maryland-College Park, 2007 Manson, Samuel S. Behavior of materials under conditions of thermal stress. TN 2933: NACA, 1953.

Magin, T., Driver, J., Lépinoux, J. and Kubin, L., Rev. Phys. Appl., **19**, 1984.

Manson, Samuel S. *Behavior of materials under conditions of thermal stress*. TN 2933: NACA, 1953.

Martin, D. E. "An energy criterion for low-cycle fatigue." Journal of Basic Engineering 83 (1961): 565.

Martin, Do E., and J. Brinn. "Some Observations on the Plastic Work Required to Fracture Stainless Steel Under Cyclic Loading." Proc. ASTM. Vol. 59. 1959.

Meneghetti, G. "Analysis of the fatigue strength of a stainless steel based on the energy dissipation." International journal of fatigue 29.1 (2007): 81-94.

Metals Handbook, Vol.2 - Properties and Selection: Nonferrous Alloys and Special-Purpose Materials, ASM International 10th Ed. 1990

Morrow, JoDean. "Cyclic plastic strain energy density and fatigue of metals." (1965).

MRC Biostatistics Unit, "The WinBUGS Project," Cambridge, UK.

Mroziński, Stanisław, and Dariusz Boroński. "Metal tests in conditions of controlled strain energy density." Journal of Theoretical and Applied Mechanics 45.4 (2007): 773-784.

Mura, Toshio. Micro-mechanics of Defects in Solids. Vol. 3. Springer, 1987.

Naderi, M., and M. M. Khonsari. "Thermodynamic analysis of fatigue failure in a composite laminate." Mechanics of Materials 46 (2012): 113-122.

Naderi, M., M. Amiri, and M. M. Khonsari. "On the thermodynamic entropy of fatigue fracture." Proceedings of the Royal Society A: Mathematical, Physical and Engineering Science 466.2114 (2010): 423-438.

Nuclear Regulatory Commission, "Reactor License Renewal Overview," http://www.nrc.gov/reactors/operating/licensing/renewal/overview.html , *Page Last Reviewed/Updated Thursday, April 25, 2013*

Ontiveros, V., Cartillier, A., Modarres, M., ' An Integradted Methodology for Assessing Fire Simulation Code Uncertainty,' Nuc. Sci. Eng., 166 (2010): 179-201.

Park, Jinsoo, and Drew Nelson. "Evaluation of an energy-based approach and a critical plane approach for predicting constant amplitude multiaxial fatigue life." International Journal of Fatigue 22.1 (2000): 23-39.

Pilkey, Walter D., and Rudolph Earl Peterson. "Peterson's stress concentration factors." (1997).Prediction Methods, Albany, NY, 18–21.

Rashband, W., 'ImageJ,' National Institues of Health, USA. http://rsb.info.nih.gov/ij/ 2008

Rusk, D. (personal communication, June 18, 2013)

S.S. Wilks. "Determination of sample sizes for setting tolerance limits" Ann Math

Stat;12:91–6, 1941

S.S. Wilks. "Statistical prediction with special reference to the problem of tolerance limits."
Ann Math Stat,13:400–409, 1942

Scott-Emuakpor, O. E., et al. "Analysis of Strain energy density Behavior Throughout a Fatigue
Process." Experimental mechanics 51.8 (2011): 1317-1323.

Scott-Emuakpor, Onome E., et al. "An energy-based uniaxial fatigue life prediction method
for commonly used gas turbine engine materials." Journal of engineering for gas
turbines and power 130.6 (2008).

Scott-Emuakpor, Onome, et al. "Development of an improved high cycle fatigue criterion."
Journal of engineering for gas turbines and power 129.1 (2007): 162-169.

Smith, R.C., Montemerlo, M., Modarres, M., Hoffman, P. 'Strain energy density Based
Proababilisitc Life Assesmment of Dynamic Structures,' IMECE2010, Nov. 12-18,
Vancouver, 2010.

Socie D, Malton G, Socie B, Prycop J, Socie M, Cook B. eFatigue. 28 Jan. 2011;
<https://www.efatigue.com/>.

Sornette, D., T. Magnin, and Y. Brechet. "The physical origin of the Coffin-Manson
law in low-cycle fatigue." *EPL (Europhysics Letters)* 20.5 (1992): 433.

Stowell, E. Z. "A study of the energy criterion for fatigue." Nuclear Engineering and Design
3.1 (1966): 32-40.

Topper, T. H., and W. D. Biggs. "The cyclic straining of mild steel." APPL MATER RES 5.4
(1966): 202-209.

V. Ontiveros, A. Cartillier, M. Modarres, An Integrated Methodology for Assessing Fire
Simulation Code Uncertainty, , Nuclear Science and Engineering, 166, 179–201
(2010).

Voyiadjis, George Z. Advances in Damage Mechanics: Metals and Metal Matrix Composites:
Metals and Metal Matrix Composites. Elsevier Science, 1999.

Walker, K. The Effect of Stress Ratio During Crack Propagation and fatigue for 2024-T3 and
7075-T6 Aluminum. Effects of Environment and Complex Load Histories on
Fatigue Life, ASTM STP 462. New Jersey: 1970;p. 1-14.

Wallace, Duane C. "Irreversible thermodynamics of flow in solids." Physical Review B 22.4
(1980): 1477.

Weertman, Johannes, and Julia Randall Weertman. "Elementary dislocation theory." (1966).

Weissmann, Gerd F. "Bending, damping and fatigue of metals." Experimental Mechanics
21.7 (1981): 255-260.

Whaley, P.W., 1983, 'A thermodynamic approach to metal fatigue,' Proc. ASME Int. Conf. Advances in Life

Winter, A. T. "A model for the fatigue of copper at low plastic strain amplitudes." *Philosophical Magazine*30.4 (1974): 719-738

Yang, B., et al. "Thermographic investigation of the fatigue behavior of reactor pressure vessel steels." Materials Science and Engineering: A 314.1 (2001): 131-139.

Yang, Bing. "Thermographic detection of fatigue damage of reactor pressure vessel (RPV) steels." Journal of materials engineering and performance 12.3 (2003): 345-353.

Zhao, T., Fatigue of Aluminum Alloy 7075-T651, Ph.D. Dissertaiton, Univeristy of Nevada, Reno. December 2008

Zhao, Tianwen, and Yanyao Jiang. "Fatigue of 7075-T651 aluminum alloy." International Journal of Fatigue 30.5 (2008): 834-849.